

A Parametric Study of the Hydrodynamic Stability Theory of 3-D Compressible Free Shear Flows

by

Peter Samuel King

Dissertation Submitted to the Faculty of the

Virginia Polytechnic Institute and State University

in partial fulfillment of the requirements for the degree of

DOCTOR OF PHILOSOPHY

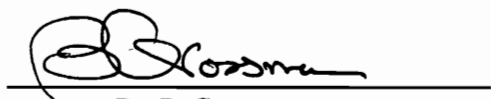
in

Aerospace Engineering

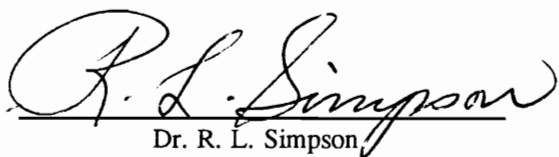
APPROVED:



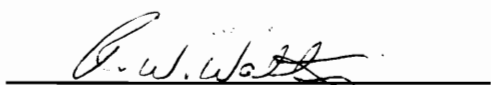
Dr. J. A. Schetz, Chairman



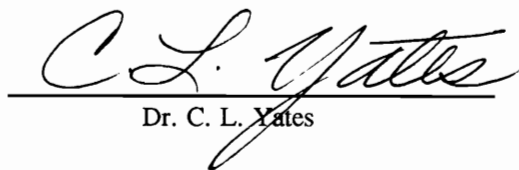
Dr. B. Grossman



Dr. R. L. Simpson



Dr. R. W. Walters



Dr. C. L. Yates

September 1991
Blacksburg, Virginia

A Parametric Study of the Hydrodynamic Stability Theory of 3-D Compressible Free Shear Flows

by

Peter S. King

Committee Chairman: Dr. Joseph A. Schetz

Aerospace & Ocean Engineering

Abstract

In this study, a new and efficient numerical algorithm is developed to solve both the two-dimensional and three-dimensional compressible hydrodynamic stability problem. A parametric study of free shear flows with two or more supersonic streams is performed. Flows examined included shear layers, jets/wakes, and various geometrical combinations of these flows. The effect of Mach number on the stability characteristics of the flow is studied and found to confirm the work of other researchers who found that increasing the relative (or convective) Mach number increases the stability of the flow. For 2-D mean flows, the most amplified disturbance is shown to be axial for $M < 1.2$ and fully three-dimensional for $M > 1.2$. Disturbances for three-dimensional mean flows are found here to be axial in the presence of side walls. The variation of the eigenfunctions and flowfield disturbances as a function of Mach number and the flow geometry was also studied. Comparisons of the stability code results are also made to several turbulent mixing experiments. The stability code correctly predicts which parameters will accelerate mixing. New correlations of the effects of some important parameters on stability are developed.

Acknowledgements

This work was supported by funds from the Johns Hopkins University Applied Physics Laboratory under the supervision of Dr. H. E. Gilreath. Dr. J. Kuttler also provided many helpful suggestions. Their help and advice are greatly appreciated.

I would like very much to thank Dr. Joseph Schetz, my committee chairman and friend, for the vast amount of support that I have received from him during my undergraduate and graduate studies at Virginia Tech. With his encouragement and guidance, it was easier to remain in school to work on my graduate degrees. I would also thank the rest of my doctoral committee for their assistance and patience.

Finally, I would like to thank my wife, Lorette, without whose constant help, support, and companionship things like college degrees don't mean much.

Table of Contents

Acknowledgements	iii
Nomenclature	vii
List of Figures	ix
1. Introduction	1
2. Stability of Two-Dimensional Background Flows	9
2.1 Derivation of the Governing Equations	9
2.2 Numerical Considerations	14
3. Results for Two-Dimensional Background Flows	19
3.1 Shear Layers	19
3.1.1 Effect of Relative Mach Number	20
3.1.2 Effect of Momentum Thickness	22
3.2 Planar Jets/Wakes	24
	iv

3.2.1	Effect of Relative Mach Number	25
3.2.2	Effect of the Jet Half-Radius	26
3.3	Combined Jet/Shear Layer Flows	26
3.3.1	Effect of Jet Velocity	27
3.3.2	Effect of Jet Location	28
4.	Comparison with Two-Dimensional Background Flow Experiments	29
4.1	Calculation of the Mean Flowfield	29
4.2	Stability Calculations	31
5.	Stability Code for Three-Dimensional Background Flows	33
5.1	Problem Formulation	33
5.2	Use of the Method to Investigate Hybrid Injection Schemes	35
6.	Results for Three-Dimensional Background Flows	36
6.1	Comparison of 2-D and 3-D Shear Layers and Jets	36
6.1.1	Shear Layers	36
6.1.2	Planar Jets	38
6.2	Fully Three-Dimensional Profiles	38
6.2.1	3-D Jet/Shear Layers	38
6.2.2	3-D Jets	39

7. Conclusions 40

References 43

Figures 47

Vita 148

Nomenclature

a	speed of sound
c	Complex wave speed, nonlinear eigenvalue
i	Imaginary unit, $i=\sqrt{-1}$
k, l	x, z wavenumbers
L	Reference length, $L \equiv y_1 $
M	Relative Mach number, $M = \Delta U / a_0$
p	Pressure
$r_{1/2}, y_{1/2}, z_{1/2}$	Jet half-radius
T	Temperature
t	Time
u, v, w	Velocity components
ΔU	Reference velocity, $\Delta U \equiv u_2 - u_1 $
\mathbf{V}	Velocity vector
x, y, z	Cartesian coordinates
ξ, η, ζ	Computational coordinates
ρ	Density
ϕ	Propagation angle of oblique disturbance
ω	Wavenumber vector, $\omega = [k, l]^T$
γ	Ratio of specific heats
δ	Boundary layer thickness

θ	Momentum thickness
μ	Initial guess for eigenvalue c
σ	Complex linear eigenvalue, $\sigma = -i\omega$
∇	Gradient (divergence)

Subscripts

0	Background flow
1,2	Flow domain limits
i	Imaginary part
r	Real part
x,y,z	Derivatives with respect to Cartesian coordinates
ξ,η,ζ	Derivatives with respect to computational coordinates
*	Value at maximum growth rate

Superscripts

'	Mean flow disturbance
*	Dimensional value

Diacritical Marks

\sim	Disturbance eigenfunction
'	Rotated variables

List of Figures

Figure 1.1 Neutral curves of the Orr-Sommerfeld equation; from White [25] . . .	48
Figure 1.2 Stability of mixing between two parallel compressible flows; from Shen [41]	49
Figure 1.3 Neutral stability curve for compressible planar jets; from Shen [41] .	50
Figure 2.1 Eigenvalue spectrum: $M=0.5$, $\theta=0.05$, $k=3.0$	51
Figure 2.2 Computational k - l wavenumber plane	52
Figure 2.3 Grid refinement study: imaginary part of c for $M=0.5$ and 1.5 , $\theta=0.02$ and 0.05	53
Figure 2.4 Grid refinement study: density eigenfunctions	54
Figure 3.1 Shear layer: $M=0.5$, $\theta=0.03$; (a) from Greenough et al. [24], (b) 2-D stability code	55
Figure 3.2 Shear layer: $M=1.5$, $\theta=0.03$; (a) from Greenough et al. [24], (b) 2-D stability code	56
Figure 3.3 Typical shear layer flowfield parameters	57
Figure 3.4 Shear layer growth rate surface: $\theta=0.02$, $M=0.05$, $d=1.0$	58
Figure 3.5 Shear layer growth rate surface: $\theta=0.02$, $M=0.25$, $d=1.0$	59
Figure 3.6 Shear layer growth rate surface: $\theta=0.02$, $M=0.50$, $d=1.0$	60
Figure 3.7 Shear layer growth rate surface: $\theta=0.02$, $M=0.75$, $d=1.0$	61
Figure 3.8 Shear layer growth rate surface: $\theta=0.02$, $M=1.00$, $d=1.0$	62

Figure 3.9 Shear layer growth rate surface: $\theta=0.02$, $M=1.25$, $d=1.0$	63
Figure 3.10 Shear layer growth rate surface: $\theta=0.02$, $M=1.50$, $d=1.0$	64
Figure 3.11 Shear layer growth rate surface: $\theta=0.02$, $M=1.75$, $d=1.0$	65
Figure 3.12 Shear layer growth rate surface: $\theta=0.02$, $M=2.00$, $d=1.0$	66
Figure 3.13 Shear layer growth rate surface: $\theta=0.02$, $M=2.25$, $d=1.0$	67
Figure 3.14 Shear layer growth rate surface: $\theta=0.02$, $M=2.50$, $d=1.0$	68
Figure 3.15 Shear layer growth rate surface: $\theta=0.02$, $M=2.75$, $d=1.0$	69
Figure 3.16 Shear layer most amplified propagation angle vs. relative Mach number	70
Figure 3.17 Shear layer most amplified wavenumber vs. relative Mach number .	71
Figure 3.18 Shear layer most amplified wavenumber (collapsed) vs. relative Mach number	72
Figure 3.19 Shear layer maximum growth rate vs. relative Mach number	73
Figure 3.20 Shear layer maximum growth rate (collapsed) vs. relative Mach number	74
Figure 3.21 Shear layer density eigenfunctions vs. relative Mach number	75
Figure 3.22 Shear layer u velocity eigenfunctions vs. relative Mach number . . .	76
Figure 3.23 Shear layer v velocity eigenfunctions vs. relative Mach number . . .	77
Figure 3.24 Shear layer density disturbance $\rho'(x,y,z=0,t=0)$; $M=0.5$, $\theta=0.02$, $k=6.75$	78

Figure 3.25 Shear layer velocity disturbance $u'(x,y,z=0,t=0)$; $M=0.5$, $\theta=0.02$, $k=6.75$	79
Figure 3.26 Shear layer velocity disturbance $v'(x,y,z=0,t=0)$; $M=0.5$, $\theta=0.02$, $k=6.75$	80
Figure 3.27 Shear layer vorticity disturbance $\Omega'_z(x,y,z=0,t=0)$; $M=0.5$, $\theta=0.02$, $k=6.75$	81
Figure 3.28 Shear layer maximum growth rate vs. momentum thickness	82
Figure 3.29 Shear layer maximum dimensional growth rate vs. momentum thickness	83
Figure 3.30 Shear layer most amplified wavenumber vs. momentum thickness ..	84
Figure 3.31 Shear layer density eigenfunctions vs. momentum thickness	85
Figure 3.32 Shear layer u velocity eigenfunctions vs. momentum thickness	86
Figure 3.33 Shear layer v velocity eigenfunctions vs. momentum thickness	87
Figure 3.34 Shear layer maximum growth rate vs. wall placement	88
Figure 3.35 Shear layer maximum growth rate (collapsed) vs. wall spacing ...	89
Figure 3.36 Shear layer density eigenfunctions vs. wall spacing	90
Figure 3.37 Shear layer u velocity eigenfunctions vs. wall spacing	91
Figure 3.38 Shear layer v velocity eigenfunctions vs. wall spacing	92
Figure 3.39 Shear layer density eigenfunction $\rho'(x,y,z=0,t=0)$; $M=0.5$, $\theta=0.02$, $d=0.6$, $k=6.75$	93

Figure 3.40 Shear layer u velocity eigenfunction $u'(x,y,z=0,t=0)$; $M=0.5$, $\theta=0.02$, $d=0.6$, $k=6.75$	94
Figure 3.41 Shear layer v velocity eigenfunction $v'(x,y,z=0,t=0)$; $M=0.5$, $\theta=0.02$, $d=0.6$, $k=6.75$	95
Figure 3.42 Shear layer vorticity eigenfunction $\Omega'_z(x,y,z=0,t=0)$; $M=0.5$, $\theta=0.02$, $d=0.6$, $k=6.75$	96
Figure 3.43 Typical planar jet flowfield parameters	97
Figure 3.44 Planar jet growth rate surface; $M=0.25$, $r_{1/2}=0.05$	98
Figure 3.45 Planar jet maximum growth rate vs. relative Mach number	99
Figure 3.46 Planar jet maximum growth rate (collapsed) vs. relative Mach number	100
Figure 3.47 Planar jet most amplified wavenumber vs. relative Mach number .	101
Figure 3.48 Planar jet most amplified wavenumber (collapsed) vs. relative Mach number	102
Figure 3.49 Planar jet density eigenfunctions vs. relative Mach number	103
Figure 3.50 Planar jet u velocity eigenfunctions vs. relative Mach number . . .	104
Figure 3.51 Planar jet v velocity eigenfunctions vs. relative Mach number . . .	105
Figure 3.52 Planar jet maximum growth rate vs. jet half-radius	106
Figure 3.53 Planar jet most amplified wavenumber vs. jet half-radius	107
Figure 3.54 Planar jet density eigenfunctions vs. jet half-radius	108
Figure 3.55 Planar jet u velocity eigenfunctions vs. jet half-radius	109

Figure 3.56 Planar jet v velocity eigenfunctions vs. jet half-radius	110
Figure 3.57 Planar jet density disturbance $\rho'(x,y,z=0,t=0)$; $M=0.75$, $r_{1/2}=0.05$, k=15.2	111
Figure 3.58 Planar jet u velocity disturbance $u'(x,y,z=0,t=0)$; $M=0.75$, $r_{1/2}=0.05$, k=15.2	112
Figure 3.59 Planar jet v velocity disturbance $v'(x,y,z=0,t=0)$; $M=0.75$, $r_{1/2}=0.05$, k=15.2	113
Figure 3.60 Planar jet vorticity disturbance $\Omega_z'(x,y,z=0,t=0)$; $M=0.75$, $r_{1/2}=0.05$, k=15.2	114
Figure 3.61 Typical jet/shear layer flowfield parameters	115
Figure 3.62 Typical jet/shear layer profiles vs. U_{jet} ; $\theta=0.02$, $y_{jet}=0.2$, $r_{1/2}=0.02$.	116
Figure 3.63 Typical jet/shear layer profiles vs. U_{jet} ; $\theta=0.02$, $y_{jet}=0.2$, $r_{1/2}=0.05$.	117
Figure 3.64 Jet/shear layer growth rates vs. k; $M=0.5$, $\theta=0.02$, $y_{jet}=0.2$, $r_{1/2}=0.02$, $\phi=0$	118
Figure 3.65 Jet/shear layer growth rates vs. k; $M=0.5$, $\theta=0.02$, $y_{jet}=0.2$, $r_{1/2}=0.05$, $\phi=0$	119
Figure 3.66 Jet/shear layer maximum growth rates vs. U_{jet} ; $M=0.5$, $\theta=0.02$, $y_{jet}=0.2$, $\phi=0$	120
Figure 3.67 Jet/shear layer most amplified wavenumber vs. U_{jet} ; $M=0.5$, $\theta=0.02$, $y_{jet}=0.2$, $\phi=0$	121
Figure 3.68 Typical jet/shear layer profiles vs. y_{jet} ; $\theta=0.02$, $U_{jet}=0.4$, $r_{1/2}=0.02$.	122

Figure 3.69 Typical jet/shear layer profiles vs. y_{jet} ; $\theta=0.02$, $U_{jet}=0.4$, $r_{1/2}=0.05$	123
Figure 3.70 Jet/shear layer growth rates vs. k ; $M=0.5$, $\theta=0.02$, $U_{jet}=0.4$, $r_{1/2}=0.02$, $\phi=0$	124
Figure 3.71 Jet/shear layer growth rates vs. k ; $M=0.5$, $\theta=0.02$, $U_{jet}=0.4$, $r_{1/2}=0.05$, $\phi=0$	125
Figure 3.72 Jet/shear layer maximum growth rates vs. y_{jet} ; $M=0.5$, $\theta=0.02$, $U_{jet}=0.4$, $\phi=0$	126
Figure 3.73 Jet/shear layer most amplified wavenumber vs. y_{jet} ; $M=0.5$, $\theta=0.02$, $U_{jet}=0.4$, $\phi=0$	127
Figure 4.1 APL experiment test conditions	128
Figure 4.2 Typical numerical grid for PNS calculations	129
Figure 4.3 Computed velocity and pressure contours for APL Case 2	130
Figure 4.4 Computed u velocity profiles at each axial station for APL Case 5	131
Figure 4.5 Growth rate planes at each axial station for APL Case 1	132
Figure 4.6 (a) Maximum growth rates; (b) comparison of growth rates vs. measured spreading rates	133
Figure 6.1 Typical computational grid for 3-D shear layer and planar jet; 61 x 31 points	134
Figure 6.2 Comparison of 2-D and 3-D shear layer growth rates vs. k ; $\theta=0.02$, $\phi=0$	135

Figure 6.14 Elliptic jet growth rates for various jet aspect ratios 147

1. Introduction

The study of the stability of compressible shear layers has been going on for many years. Since the recent interest in the development of the National Aerospace Plane (NASP), these studies have taken on a renewed vigor because this vehicle would be propelled by a supersonic combustion ramjet, or scramjet, propulsion system. Subsonic mixing is fairly well understood, and augmentation methods such as the addition of swirl are used with great success. However, these subsonic mixing techniques fail to provide efficient mixing for high speed flows. Since the residence time of fuels in supersonic combustors is exceedingly short, the mixing of two parallel supersonic streams is of primary importance to the design of propulsion systems using supersonic combustion. Methods that could increase the rate of mixing of the fuel-air layers would have a large impact on the size of the combustor. Because the NASP will have a highly integrated airframe, a reduction in the size of the propulsion system can have a large effect on the total weight of the aircraft. Therefore, it is of the utmost importance to understand the physics behind the rate at which these shear layers can be mixed. This interest has led to numerous experiments to determine conditions and configurations that will provide for enhanced mixing. This, in turn, would allow for the design of more efficient supersonic combustors. Wind tunnel experiments performed by King and Schetz [1] dealing with the mixing characteristics of combined normal and tangential supersonic injection found that for the proper combination of geometry and pressures, the production of large turbulent eddy structures could be greatly increased. These large structures and their subsequent

breakdown into smaller eddies are responsible for the entrainment of free stream air into the fuel streams, so that efficient combustion can take place. However, the exact configurations that produced these structures was extremely hard to predict, and they were found mostly by "trial and error" experimentation. And, since these experiments consisted mainly of cold flow conditions, they did not adequately take into account more realistic conditions found in actual combustors. It was decided that an analytical framework that could assist in the prediction of the growth rates, sizes, and locations of these structures as a function of important flow parameters, such as Mach number and velocity profile shapes, would be of great practical application, and development of the methods described in this study was begun. Such a tool would also be useful for assessing other augmentation schemes.

It has long been established that the spreading rates (and hence mixing rates) of supersonic free shear layers is substantially less than that of subsonic and incompressible mixing layers. This was originally thought to be due to density ratio effects. However, studies by Bogdanoff [2] and Papamoschou and Roshko [3] introduced the concept of the convective Mach number as the proper parameter with which to scale compressibility effects. The convective Mach number is defined by

$$M_c = \frac{U_1 - U_2}{a_1 + a_2}$$

where U_1 and U_2 are the velocities and a_1 and a_2 are the sound speeds in the two streams. It is the Mach number measured in a moving frame of reference fixed to the dominant

waves or structures in the mixing layer, i.e. in a Lagrangian frame of reference. They suggested that the normalized growth rate of turbulent compressible mixing layers is a function of the convective Mach number. They also noted that the curve of the normalized spreading rate versus the convective Mach number is very similar to that of the normalized instability growth rate curve, implying that the decrease in spreading rate is directly related to the reduction of the instability of the mixing layer. This has since been confirmed by many other researchers, including Ragab and Wu [4] using multiple scale and Floquet methods, Tam and Hu [5], who derived the relevant dispersion relation and used grid searching techniques to find the poles, and Zhuang et al. [6], who used shooting methods. Lele [7] also confirmed these results using direct numerical simulations of compressible free shear layers. So, by studying the mathematical problem of the stability of high speed shear layers, some light can be shed on the processes by which these shear layers actually mix and grow.

Hydrodynamic stability theory is concerned with whether or not a given velocity profile is stable with respect to small disturbances. By "stable" we mean that perturbations to the flow decrease with time, returning the flow to its initial state. Suppose that Q_0 represents a flow solution, or an approximate solution, to the governing flow equations. A small disturbance Q' is assumed and then added to the basic solution, and this perturbed solution, Q_0+Q' , is substituted back into the governing equations. The terms involving Q_0 that identically satisfy the governing equations are eliminated, and we are left with the disturbance equations that describe the behavior of Q' in terms of Q_0 and the

parameters of the flow being considered. If the disturbance increases with time, the flow is said to be unstable. Note that the disturbance, which generally may be represented in terms of its Fourier components, must be stable at all frequencies in order for the flow to be considered stable. If even one frequency component is found to be unstable, then the entire flow must be considered unstable. The theory says nothing concerning whether an instability leads to some permanent divergence or some other stable configuration. The stability referred to here is temporal stability, as opposed to spatial stability. That is, the equations describe how the disturbances grow in time, rather than how they grow in space. Use of temporal stability can be justified by the following argument. Since the governing equations for supersonic flow are hyperbolic, a disturbance at some point cannot influence the flow upstream of it. This behavior is also seen for temporally growing mixing layers, since a temporal disturbance does not affect the previous development of the flow. A Lagrangian viewpoint is assumed in this study in order to simplify the mathematics, but it is also justified from the concept of a convective reference frame attached to the dominant flow structures. Temporal and spatial stability are found to be equivalent only at points of neutral stability.

Some of the first studies into the linear stability of two supersonic streams were conducted by Landau [8], Pai [9], and Hatanaka [10]. These authors considered an unbounded vortex sheet and found that the Mach number must be less than $\sqrt{8}$ as a requirement for stability. Miles [11] found the same results using transform methods. Blumen [12], Blumen et al. [13], and Drazin et al. [14] dealt with unbounded continuous

profiles and found multiple modes of instabilities. The hyperbolic-tangent profile has been studied by many authors. They include Michalke [15], who studied this profile using the inviscid Rayleigh stability equations. Ragab and Wu [16] studied the effect of flow parameters on the growth of instability waves using both viscous and inviscid stability analysis to study both two-dimensional and oblique modes.

While the development and roll-up of vortices in the shear layer is clearly a nonlinear process, the initial physics of this process can be conveniently examined using linear theory. The classic experiments of Schubauer and Skramstad [17] established once and for all the basic correctness of linear stability theory as the mechanism for the instability of laminar incompressible shear layers. These experiments consisted of placing a thin metal ribbon close to the wall and oscillating it electromagnetically. The disturbances downstream were measured with a hot wire probe, and the results were found to agree very well with the linear theory. Similar experiments for compressible flow were performed by Laufer and Vrebalovich [18]. Riley and Metcalfe [19] used direct numerical simulations of incompressible flows using perturbations of the Orr-Sommerfeld equations and saw that vortices corresponding to the wavelengths predicted from linear theory were indeed produced. McMurtry [20] extended that work to low Mach number compressible flows. Numerical studies have been carried out by Sandham et al. [21] who studied the spatial stability of three-dimensional modes in high speed flows and found that the maximum growth rates are proportional to the predicted linear growth rates of those modes. They also noted that the physics controlling the nonlinear roll-up of vortices is

contained in the linear eigenfunctions. Soetrisno et al. [22] studied the role of shocks in compressible mixing layers and found that their growth is inhibited as the Mach number is increased. Wind tunnel experiments have been performed to measure spreading rates, and the results have been compared to theory by Gilreath and Sullins [23]. Greenough et al. [24] studied the effect of walls on inviscid compressible mixing layers, and conducted direct numerical simulations in order to study the nonlinear development of the instability waves. These results confirmed the effect of Mach number on the reduction of the growth rate, and they concluded that the linear theory can be very useful in understanding the physics of compressible free shear layers and predicting the actual nonlinear growth rate of plane mixing layers.

Although researchers have studied both viscous and inviscid stability, the inviscid analysis shows much promise when examining high speed shear layers. Figure 1.1 [from 25, p. 401] shows the stability characteristics for incompressible viscous flow derived from the Orr-Sommerfeld equations. It indicates that for incompressible flows, profiles with an inflection point are unstable for all Reynolds numbers above some critical Reynolds number, while flows without an inflection point tend to be more stable and are always stable in the limit of large Re_δ . Rayleigh [26] showed that for an inviscid flow ($Re_\delta \rightarrow \infty$), an inflection point in the velocity profile is a necessary condition for instability. For compressible flows, similar results have been obtained. Figure 1.2 shows some of Lessen's calculations [27] for the stability of compressible unbounded shear layers. The wavenumber associated with the point of neutral stability is seen to approach a constant

value for large Reynolds numbers, and this indicates that an inviscid analysis is appropriate to determine the limits of stability for these conditions. Figure 1.3 shows that this effect also holds for unbounded planar jets [28,29]. Therefore, since this study will be dealing with compressible flows at high Reynolds number with one or more inflection points, an inviscid analysis is deemed to be adequate.

Not many researchers seem to have addressed the stability of three-dimensional mixing flows. Koshigoe and Tubis [30,31], Baty and Morris [32], and Morris et al. [33] have studied three-dimensional shear layers and jets of arbitrary geometries, but have mostly limited their studies to incompressible cases. They found that circular jets are nearly stable, and that the profiles must be noncircular in order to promote rapid growth. They have used a spatial stability analysis which is not directly comparable to temporal analyses except for the stability region boundaries (i.e. on the neutral curves), but some researchers feel that spatial stability can be better compared to experimental data.

In this study, the hydrodynamic stability of confined free shear layers will be studied in an attempt to discover the effect of several flow parameters on the mixing of two (or more) supersonic streams. These parameters include the relative Mach number (in this study, the relative Mach number is equal to twice the convective Mach number), shear layer and jet thicknesses, and geometric parameters, such as jet spacing and wall placement. Inviscid linear stability analysis from a temporal viewpoint provides a relatively straightforward method to examine this problem. It provides information about the most amplified wavenumbers, the range of amplified wavenumbers, and the spatial

extent, both lateral and transverse, of their disturbances. The types of flows treated in the current study include two-dimensional shear layers, planar jets, and combinations of these two flows. Variations of these flows were also studied in three dimensions, including shear layers in three dimensions with the addition of side walls, axisymmetric and elliptic jets, and combinations of shear layers with jets similar to those studied experimentally by King and Schetz in [1].

The approach used here was developed as a new hybrid linear/nonlinear scheme aimed at reducing the total memory and run times needed to solve the stability equations. A large global linear eigenvalue problem is solved to get an initial point in the growth rate plane. Then, a highly efficient nonlinear inverse iteration routine is used to find the stability characteristics at other points until the instability surface is mapped out sufficiently. This hybrid method has been found to be extremely effective in reducing the total cost of these calculations. Recently, a similar method has been reported by Malik [34], who used it to solve a different set of equations in the study the transition of compressible wall boundary layers. These methods differ from those of Greenough et al. [24], who used shooting method techniques to integrate the equations across the flow, in that no *a priori* knowledge of the growth rates are needed in order to solve the eigenvalue problem.

2. Stability of Two-Dimensional Background Flows

2.1 Derivation of the Governing Equations

The unsteady Euler equations are the appropriate governing equations for inviscid, compressible fluid flows:

$$\begin{aligned}\rho^*_{,t} + \nabla^* \cdot (\rho^* \mathbf{V}^*) &= 0 \\ \rho^* \mathbf{V}^*_{,t} + \rho^* (\mathbf{V}^* \cdot \nabla^*) \mathbf{V}^* + \nabla^* p^* &= 0 \\ \rho^* [e^*_{,t} + (\mathbf{V}^* \cdot \nabla^*) e^*] &= -p^* (\nabla^* \cdot \mathbf{V}^*)\end{aligned}\tag{2.1}$$

where the asterisks denote dimensional quantities. Assuming ideal gas behavior, no heat addition or shocks, and constant entropy and total enthalpy upstream, the energy equation can be replaced with the isentropic relation

$$\frac{p^*}{\rho^{*\gamma}} = \text{constant}.$$

These equations are nondimensionalized by the freestream conditions:

$$\mathbf{V} = \frac{\mathbf{V}^*}{\Delta U^*} = [u, v, w]^T, \quad \mathbf{r} = \frac{\mathbf{r}^*}{L^*} = [x, y, z]^T\tag{2.3}$$

$$\rho = \frac{\rho^*}{\rho_0^*}, \quad p = \frac{p^*}{\rho_0^* a_0^{*2}}, \quad \nabla = \nabla^* L^*, \quad t = \frac{t^* \Delta U^*}{L^*}$$

where ΔU^* is a characteristic relative velocity and L^* is a characteristic length for the problem. The constants ρ_0^* and a_0^* are the ambient density and sound speed, respectively. When these are substituted into Eqn. 2.1, and the constant in the isentropic relation is evaluated at the ambient conditions, the nondimensional equations are

$$\begin{aligned}
\rho_t + \nabla \cdot (\rho \mathbf{V}) &= 0 \\
\rho \mathbf{V}_t + \rho (\mathbf{V} \cdot \nabla) \mathbf{V} + \frac{1}{M^2} \nabla p &= 0 \\
\frac{p}{\rho^\gamma} &= \frac{1}{\gamma}.
\end{aligned} \tag{2.2}$$

These equations are linearized with respect to the ambient conditions of the mean flowfield. The disturbed quantities are

$$\begin{aligned}
\rho &= 1 + \rho' \\
\mathbf{V} &= \mathbf{V}_o + \mathbf{V}' \\
p &= \frac{1}{\gamma} + p'
\end{aligned} \tag{2.3}$$

where the small disturbance quantities are denoted by primes. Equation 2.3 is substituted into Eqns. 2.2. In order to linearize the disturbed isentropic relation $1 + \gamma p' = (1 + \rho')^\gamma$, the binomial expansion, $(a+x)^n = a^n + na^{n-1}x + \frac{1}{2}n(n-1)a^{n-2}x^2 + \dots$ where $x < 1$, is used. The isentropic relation then reduces to $p' = \rho'$, after neglecting terms of order ρ'^2 , thus eliminating p' from the set of disturbance equations. When Eqns. 2.3 are put back into Eqns. 2.2 and products of primed quantities are neglected, we get the following set of disturbance equations:

$$\begin{aligned}
\rho'_t + \nabla \cdot \mathbf{V}' + (\mathbf{V}_o \cdot \nabla) \rho' &= 0 \\
\mathbf{V}'_t + (\mathbf{V}_o \cdot \nabla) \mathbf{V}' + (\mathbf{V}' \cdot \nabla) \mathbf{V}_o + \frac{1}{M^2} \nabla \rho' &= 0.
\end{aligned} \tag{2.4}$$

The domain of interest is a plane channel air flow bounded by walls at $y=y_1$ and $y=y_2$, extending to infinity in the x - and z -directions, and consisting of 2-D parallel flow in the x -direction. Since the directions x and z extend to infinity, it is reasonable to expect

that the solutions should be either periodic in x and z , or independent of them [35]. Thus, the disturbances to the mean flow can be represented by a superposition of sinusoids in the x - z plane and travelling in the x -direction:

$$\begin{bmatrix} \rho'(r,t) \\ u'(r,t) \\ v'(r,t) \\ w'(r,t) \end{bmatrix} = \sum_{k=-\infty}^{\infty} \sum_{l=-\infty}^{\infty} A(k,l) \begin{bmatrix} \tilde{\rho}(y) \\ \tilde{u}(y) \\ \tilde{v}(y) \\ \tilde{w}(y) \end{bmatrix} e^{i(kx+lz-ckt)}$$

where k and l are the x - and z -wave number components and c is the complex phase speed. The vector function of y on the right hand side is the mode shape of the disturbance, while $A(k,l)$ is the disturbance amplitude at time $t=0$. The real part of each spectral component is of the form

$$A(k,l) e^{c_r k t} \begin{bmatrix} \tilde{\rho}(y) \\ \tilde{u}(y) \\ \tilde{v}(y) \\ \tilde{w}(y) \end{bmatrix} \cos(kx + lz - c_r k t). \quad (2.5)$$

Each component propagates at an angle $\phi = \tan^{-1}(l/k)$ with respect to the x -axis at a speed c_r and with a growth rate of $c_i k$. If the complex quantity σ is defined as $-(ick)$ the growth rate is simply σ_r . Positive values of the growth rate indicate that the disturbance is unstable and will grow in time. Damped disturbances are indicated by negative values. Note that the disturbance can be fully oblique even if the background flow is only two-dimensional.

If the form of the disturbance defined by Eqn. 2.5 is substituted back into Eqn. 2.4, the disturbance equations for a particular wave number $\omega=[k,l]^T$ are written as

$$ik(u_o - c)\rho + i(ku + lw) + \frac{dv}{dy} = 0$$

$$\frac{ik}{M^2}\rho + ik(u_o - c)u + \frac{du_o}{dy}v = 0$$

$$\frac{1}{M^2}\frac{d\rho}{dy} + ik(u_o - c)v = 0$$

$$\frac{il}{M^2}\rho + ik(u_o - c)w = 0$$

where the primes have been dropped for convenience. By applying a rotation of the coordinate system in the x-z plane to align with the wavenumber vector ω

$$\acute{k}^2 = k^2 + l^2, \quad \acute{k}u = ku + lw,$$

$$\acute{u}_o = u_o \cos \phi, \quad k = \acute{k} \cos \phi,$$

a reduction of the number of variables is achieved by eliminating w. This is similar to Squire's analogy used in incompressible stability analysis, but it is used here only to simplify the mathematics. The rotated equations are

$$\begin{aligned} i\acute{k}(\acute{u}_o - c)\rho + i\acute{k}u + \frac{dv}{dy} &= 0 \\ \frac{i\acute{k}}{M^2}\rho + i\acute{k}(\acute{u}_o - c)u + \frac{d\acute{u}_o}{dy}v &= 0 \\ \frac{1}{M^2}\frac{d\rho}{dy} + i\acute{k}(\acute{u}_o - c)v &= 0. \end{aligned} \tag{2.6}$$

In matrix notation these are

$$\begin{bmatrix} ik\dot{u}_o & ik & D_y \\ \frac{ik}{M^2} & ik\dot{u}_o & \frac{d\dot{u}_o}{dy} \\ \frac{1}{M^2}D_y & 0 & ik\dot{u}_o \end{bmatrix} \begin{bmatrix} \rho \\ \dot{u} \\ v \end{bmatrix} = -\sigma \begin{bmatrix} \rho \\ \dot{u} \\ v \end{bmatrix} \quad (2.7)$$

where $D_y = d/dy$. It is obvious from Eqn. 2.7 that we are dealing with a linear eigenvalue problem. These three equations can be reduced to one equation for ρ :

$$(u_o - c) \frac{d^2 \rho}{dy^2} - 2 \frac{du_o}{dy} \frac{d\rho}{dy} + [k^2 M^2 (u_o - c)^3 - (u_o - c)(k^2 + l^2)] \rho = 0. \quad (2.8)$$

Equation 2.8 can also be written in the form of a nonlinear eigenvalue problem

$$[A_0 + cA_1 + c^2A_2 + c^3A_3] \rho = 0 \quad (2.9)$$

where

$$\begin{aligned} A_0 &= u_o D_y^2 - 2 \frac{du_o}{dy} D_y + k^2 M^2 u_o^3 - u_o (k^2 + l^2) \\ A_1 &= -D_y^2 - 3k^2 M^2 u_o^2 + k^2 + l^2 \\ A_2 &= 3k^2 M^2 u_o, \quad A_3 = -k^2 M^2 \\ D_y^2 &\equiv \frac{d^2}{dy^2}, \quad D_y \equiv \frac{d}{dy}. \end{aligned} \quad (2.10)$$

The boundary condition used with Eqns. 2.7 and 2.8 is the condition that there be no mass flux through the walls, or $v(y_1) = v(y_2) = 0$. From the last of Eqn. 2.6, $d\rho/dy(y_1) = d\rho/dy(y_2) = 0$. If the second in Eqn. 2.6 is differentiated with respect to y and $d\dot{u}_o/dy = 0$ is imposed at the walls, we obtain the last boundary condition, $d\dot{u}/dy(y_1) = d\dot{u}/dy(y_2) = 0$.

2.2 Numerical Considerations

In order to solve the eigenproblem Eqn. 2.7, the problem can be formulated on a finite-difference grid. The grid was generated by dividing the background velocity u_0 into n discrete points. The distribution of these points is accomplished by dividing a modified "arc length" into equal intervals. The true arclength is computed from

$$ds = \int_{s_1}^{s_2} \left(1 + \frac{du_0}{dy} \right)^{1/2} dy.$$

However, this function does not give a satisfactory distribution of points, so it is modified by writing

$$ds' = \int_{s_1}^{s_2} \left(1 + G \log \left(\frac{du_0}{dy} + 1 \right) \right)^{1/2} dy.$$

where G is a parameter that allows for variable concentration of points in regions of high velocity gradients. Typical values of G range from 1.5 to 4.0. Integrating the modified arclength across the flowfield and dividing it into equal intervals gives a satisfactory and efficient grid generation scheme. Grid metrics for this unequally spaced grid were also computed.

Equation 2.7 is written in second-order accurate central difference form, and it can be solved using the IMSL¹ routine DEVLCG which solves a general complex eigenvalue problem by the QR algorithm. This algorithm is only practical when the matrix is of

¹International Mathematics Software Library

upper Hessenberg form, so DEVLG first converts the general, complex matrix using a series of plane rotations to eliminate the entries below the first subdiagonal. Then, this matrix is reduced to upper triangular form using a series of unitary transformations. The eigenvalues are then the diagonal entries of the upper triangular matrix. This algorithm is used to find the entire eigenvalue spectrum. This routine is rather inefficient here, since the matrix is extremely sparse. In order to overcome this inefficiency, the nonlinear eigenproblem Eqn. 2.9 is solved for the complex phase speed (eigenvalue) c and the mode shape (eigenfunction) $\rho(y)$ by a modified inverse iteration scheme [37,38]. Equation 2.9 is rewritten as a larger linear eigenproblem of the form

$$\begin{bmatrix} 0 & I & 0 \\ 0 & 0 & I \\ B_0 & B_1 & B_2 \end{bmatrix} \begin{bmatrix} x_3 \\ x_2 \\ x_1 \end{bmatrix} = c \begin{bmatrix} x_3 \\ x_2 \\ x_1 \end{bmatrix} \quad (2.11)$$

where $x_1 = cx_{i+1}$, $x_3 = \rho$, and $B_i = -A_3^{-1}A_i$. Inverse iteration can be used efficiently here by writing

$$\begin{bmatrix} -\mu I & I & 0 \\ 0 & -\mu I & I \\ B_0 & B_1 & B_2 - \mu I \end{bmatrix} \begin{bmatrix} x_3 \\ x_2 \\ x_1 \end{bmatrix}^{j+1} = \begin{bmatrix} x_3 \\ x_2 \\ x_1 \end{bmatrix}^j$$

at each iteration j , where μ is an initial estimate for the eigenvalue c . This can be simplified further by combining the system of equations to get

$$\left[A_0 + \mu A_1 + \mu^2 A_2 + \mu^3 A_3 \right] x_1^{j+1} = A_0 (x_2^j + \mu x_3^j) + \mu A_1 x_2^j - \mu^2 A_3 x_1^j$$

Thus, only a single linear system must be solved at each iteration. Once the vector x_1^{j+1} has been found, the best estimate of the corresponding eigenvalue can be computed using the Rayleigh quotient

$$c = \frac{(x^{j+1})^T A x^{j+1}}{(x^{j+1})^T x^{j+1}}$$

where A and x are the matrix and vector from Eqn. 2.11. One drawback to this method is that a sufficiently good estimate of the eigenvalue must be obtained to start each iteration cycle. This starting value can be found by solving the larger linear eigenproblem, Eqn. 2.7. The IMSL routine computes the entire spectrum of n eigenvalues, and the one corresponding to the largest growth rate is used for μ . A typical eigenvalue spectrum for a shear layer is given in Fig. 2.1. Note the symmetry about both the real and imaginary axes.

This hybrid linear/nonlinear method is particularly efficient when one is interested in solving the eigenproblem many times while varying some parameter. Once the eigensystem (eigenvalue and corresponding eigenvector) is determined for a certain set of parameter values, one can use that solution to start the iteration procedure for a slightly different set of parameters [38]. For example, the solution is marched along lines of constant ϕ in the k - l wavenumber plane until the growth rate approaches zero as shown in Fig. 2.2. The linear routine is used to find the solution at some value of k near zero ($k=0$ is a singular point of the equations), and this is used to start the iteration for $k+\delta k$. The initial solution can be used to start the iteration for all $\phi=\text{constant}$ lines. This hybrid

approach works quite well in reducing the total CPU time necessary to compute the solution for the entire k -1 subplane of interest compared to using the linear scheme at all of the points. This method is also faster than other techniques that have been used for shear layer stability, for example the integration methods of Greenough et al. [24].

A grid refinement study was done in order to determine the optimum number of grid points with which to discretize the velocity profiles. Some results of this study are shown in Figs. 2.3 and 2.4 for a hyperbolic-tangent velocity profile for two different relative Mach numbers and momentum thicknesses. Figure 2.3 shows the results for several cases. The values plotted are normalized by the nonlinear solution for one hundred grid points, which is assumed to be the most accurate solution, since it represents an exceedingly fine grid. It shows that for these profiles, at least fifty grid points were needed to resolve the growth rates to within 1% of the correct solution. In practice, sixty points were used for these profiles, and up to seventy-five points were used for more complex profiles. Since the computed density eigenfunctions were later integrated across the domain in order to compute the velocity and vorticity eigenfunctions, one hundred points were used to calculate the eigenfunctions to improve the accuracy of the integrations. Figure 2.4 shows some of the density eigenfunctions for various numbers of grid points.

The execution time of the calculations was measured. The linear portion computed the eigenvalue spectrum for a distribution of sixty to one hundred points in less than two CPU seconds on the Virginia Tech IBM 3090 vector processor. The nonlinear routine

took approximately 0.1 msec per grid point per iteration. The nonlinear routine converged to a residual of 10^{-6} in two to five iterations per point in the $k-l$ plane.

3. Results for Two-Dimensional Background Flows

In order to verify that the stability code gives accurate results, test cases were run for a shear layer with momentum thickness $\theta=0.03$ and relative Mach numbers $M=0.5$ and 1.5 . These results were then compared to those of Greenough et al. [24] obtained with other solution methods. The results for $M=0.5$ are shown in Fig. 3.1, and for $M=1.5$ in Fig. 3.2. The growth rate surfaces show excellent agreement. Therefore, we can proceed confidently to other profiles.

3.1 Shear Layers

A typical shear layer is shown in Fig. 3.3. The important parameters under consideration in a 2-D inviscid, compressible shear layer flow include the relative Mach number M based on the velocity difference between the two streams, the shear layer momentum thickness θ (or boundary layer thickness δ), and the channel thickness ratio, $d=|y_2/y_1|$. The variation of these parameters was studied over the following ranges: $0 \leq M \leq 3$, $0.005 \leq \theta \leq 0.050$, and $0.05 \leq d \leq 1.0$. These ranges cover most supersonic shear layer cases of practical interest. The variations are compared to a baseline case of $M=0.5$, $\theta=0.02$, and $d=1.0$. The profile used is given by $U(y)=\frac{1}{2}\tanh(ay)$, where a is chosen to be $0.3069/\theta$, or $2.647/\delta$. (For these profiles, $\delta=8.624\theta$.) This profile was chosen due to its simple analytical form and smoothness properties, and it has been used by numerous researchers over the years, e.g. [4,5,15,24]. The value of a is found by setting $U(\delta)=0.99$. The phase velocity (convective velocity), c_r , was found for all shear layer cases to be equal to the average of the two stream velocities.

3.1.1 Effect of Relative Mach Number

Figures 3.2 through 3.13 consist of the growth rate surfaces in the k,l plane for various values of the relative Mach number ranging from 0.05 to 2.75, with $\theta=0.02$ and $d=1.0$ held constant. The focus of each surface indicates the wave component (wavenumber and propagation angle) having the maximum growth rate. Values associated with this point of maximum temporal growth rate are indicated by the subscript $*$. It is assumed that this component will dominate the flow after some amount of time t has passed. This disturbance component has a wavenumber of $|\omega|=(k^2+l^2)^{1/2}$ and a propagation angle $\phi=\tan^{-1}(l/k)$ with respect to the positive x -axis. For subsonic and transonic values of M , the point of maximum growth rate is found to be located on the k -axis, indicating a purely two-dimensional (axial) disturbance independent of z . As M is increased past approximately 1.2, the maximum point moves off the k -axis, and the disturbance becomes an oblique one, being a function of both x and z . The variation of this propagation angle ϕ_* with respect to M is shown in Fig. 3.16. The symbols represent results calculated with the stability code. The nonzero portion of the curve can be approximated by $M \cos \phi = 1.2$. The most amplified wave number, $|\omega|_*$, is given in Fig. 3.17 as a function of the relative Mach number. It is seen to be nearly constant for $M < 0.5$, decreasing through the transonic range, and constant again for $M > 1.2$. If the value of $|\omega|_*$ is divided by its value at $M=0$, the data nearly collapses onto a single curve, as shown in Fig. 3.18.

Figure 3.19 is a plot of the maximum growth rate σ_* versus M for various values of θ . The maximum growth rate is seen to decrease with increasing M , as predicted by

theory and experiments. If the growth rate is divided by the growth rate at $M=0$ the curves collapse reasonably well onto one curve. This is shown in Fig. 3.20. A curve fit to these points is given by:

$$\frac{\sigma_{r*}}{\sigma_{r*(M=0)}} = \cos^2(0.53M) \quad \text{for } 0 \leq M \leq 1$$

$$\frac{\sigma_{r*}}{\sigma_{r*(M=0)}} = \frac{0.753}{M} \quad \text{for } M > 1$$

These equations were found by a linear least-squares analysis performed on the collapsed growth rate data.

Figure 3.21 is a plot of the density eigenfunction ρ_* corresponding to the most amplified disturbance for various M . ^{values of} The eigenfunctions are seen to be nearly symmetric about the center of the shear layer. It is clear from this plot that compressibility effects of the disturbance are not confined to the shear layer itself, but extend across the entire flow. The next two figures, Figs. 3.22 and 3.23 are the streamwise and vertical velocity eigenfunctions. Keep in mind that these eigenfunctions are for only the *one* mode of the disturbance that is believed to dominate the flow, and that the actual disturbance is made up of the superposition of *all* the modes. Neither of these functions appear to have any particular symmetry with respect to the shear layer center. These plots also show the distribution of points calculated by the grid generation routine. The full flowfield disturbances, $\rho'(x,y,z,t)$, etc., due to these components can be calculated from Equation 2.5. Figures 3.24 through 3.27 are the density, streamwise and vertical velocities, and z -

vorticity disturbances at time $t=0$ for the baseline case of $\theta=0.02$ and $M=0.5$. The vorticity disturbance is derived from the formula

$$\Omega'_z = \frac{\partial v'}{\partial x} - \frac{\partial u'}{\partial y}.$$

Figure 3.24 is also the pressure disturbance (since $p'=\rho'$), and it indicates alternating regions of high and low pressure on either side of the shear layer. These pressure fluctuations result in the shear layer taking on a wavy shape and eventually rolling up into vortical structures. Figure 3.27 shows the structure of these counter-rotating vortices.

3.1.2 Effect of Momentum Thickness

From Fig. 3.28, we can see the effect of the momentum thickness θ on the maximum shear layer growth rate. Lines fit to the computed data points are of the form $\sigma_r^* = \kappa(M)\theta^{0.9945}$, showing a decrease in the maximum growth rate for increasing relative Mach number. In order to collapse this data, the maximum growth rate is multiplied by the relative Mach number. The justification for this choice of multipliers is obvious from the equation for the dimensional growth rate

$$\sigma_r^* = k^* c_i^* = \frac{a_0 M}{L} k c_i, \text{ or } M k c_i = M \sigma_r^* = \frac{L}{a_0} \sigma_r^*$$

Thus, the quantity $M \sigma_r^*$ is proportional to the dimensional growth rate σ_r^* . From Fig. 3.27, the dimensional growth rate is seen to be independent of M for $M \geq 1$.

In Fig. 3.30, it is shown that the most amplified wavenumber $|\omega|_*$ is also independent of M for $M \geq 1$, and nearly so for $M < 1$. The "jitter" observed for the smaller

values of $|\omega|_*$ is due to the finite k step size used in the calculations in k - l plane (typically $\delta k=0.2$ to 0.4).

The next three figures, Figs. 3.31 to 3.33, show the density, streamwise and vertical velocity eigenfunctions versus θ for $M=0.5$. Again, the density eigenfunctions in Fig. 3.31 are symmetric about the shear layer center since $M<1$, and no particular symmetry is seen for the velocity eigenfunctions.

3.1.3 Effect of Wall Placement

The height of the upper wall was varied to study the effects of the wall placement on the growth of the shear layer disturbances. The parameter $d \equiv |y_2/y_1|$ was used to indicate the relative spacing of the walls with respect to the shear layer center. Figure 3.34 shows the variation of the maximum growth rate with the wall spacing d . It shows that the wall placement has little effect upon σ_r for large values of d . Figure 3.35 is the same data plotted versus d/δ , and it shows that d has no effect on the maximum growth rate until $d/\delta \approx 2$ or 3 . Below this value, σ_r drops off rapidly. This indicates that the shear layer must have room above and below to grow, and placing the wall too close to the shear layer severely dampens the maximum growth rate. The effect occurs at larger values of d/δ as M increases.

The next three figures show the effect of varying d on the eigenfunctions for the baseline conditions of $M=0.5$ and $\theta=0.02$. Figure 3.36 shows that the density eigenfunction is antisymmetric for symmetrically placed walls ($d=1$) and unsymmetric for $d<1$. Also, note that the maximum point of the eigenfunction is pushed downward as the top

wall spacing is decreased. Figures 3.37 and 3.38 show similar trends. Figures 3.39 through 3.42 show the full flowfield disturbances for $M=0.5$, $\theta=0.02$, and $d=0.6$ at the most amplified wavelength. Note that the disturbances are not affected by the upper wall, since it is several boundary layer thicknesses above the shear layer.

3.2 Planar Jets/Wakes

In order to study the stability characteristics of 2-D jets and wakes, velocity profiles of the form

$$U(y) = \text{sech}^2(by), \quad \text{for jets}$$

$$U(y) = 1 - \text{sech}^2(by), \quad \text{for wakes}$$

were used, where $b=0.8814/r_{1/2}$. As with the shear layer profile, this form of profile has the qualities of smoothness and analytic simplicity, and it also is in agreement with experimentally measured jets and wakes. See Fig. 3.43 for an illustration. The phase speed of the jets was found to vary between that of the freestream and jet (i.e. between 0 and 1), decreasing for increased relative Mach number and nearly independent of the jet half-radius. The stability characteristics of the wakes studied matched those of the equivalent jets, except that the phase speed is equal to $(1-c_{r_{jet}})$. This can be seen by the following argument. If the jet velocity profile, $\text{sech}^2(ay)$, is multiplied by -1, the coefficients A_i in Eqns. 2.10 change sign for even i , and remain the same for odd i . Then, Eqn. 2.9 becomes $[A_0 - cA_1 + c^2A_2 - c^3A_3]\rho = 0$. Thus, if some value of c is a solution to Eqn. 2.9, $-c$ is a solution the equation above. But, since the eigenvalues occur in oppositely signed pairs as shown on Fig. 2.2, the phase speed (c_r) and growth rates are the same for

both cases. The addition of a unit velocity to $-\text{sech}^2(ay)$ only has the effect of shifting the real part of c by 1. This is seen in Eqn. 2.8, where c only occurs in the grouping $(u_0 - c)$. Thus shifting u_0 by some amount has the result of shifting c by the same amount. Thus, the growth rates are the same for jets and wakes, but the wake phase speed is now $(1 - c_{r_{\text{jet}}})$. For these reasons, wakes are not discussed further in this study.

3.2.1 *Effect of Relative Mach Number*

The relative Mach number is now that between the jet maximum (or wake minimum) and the freestream. Figure 3.44 is a typical plot of the growth rate in the wavenumber plane. Figure 3.45 shows the maximum growth rate σ_{*} versus M for several values of the jet half-radius. The maximum growth rate is larger for a jet than a shear layer of the same size and Mach number (see Fig. 3.19). Again, the data can be collapsed by dividing the growth rate by the growth rate at $M=0$. This is shown in Fig. 3.46. As in the case of shear layers, the maximum growth rate decreases with increasing relative Mach number.

The variation of the most amplified wavenumber with M is shown in Fig. 3.47. The wavenumber decreases with M as it does for shear layers. Again, the data can be collapsed as in Fig. 3.48.

Figures 3.49 through 3.51 are the density and velocity eigenfunctions for a nominal jet size of $r_{1/2}=0.05$. They are seen to be either symmetric or antisymmetric with respect to the jet centerline. This is because the jet is symmetric in the freestream. The disturbances widen out into the freestream as the Mach number is increased.

3.2.2 *Effect of the Jet Half-Radius*

Figure 3.52 is the variation of the maximum growth rate with the jet half-radius for various relative Mach numbers. The effect of increasing jet half-radius is to decrease the maximum growth rate. This data does not collapse for $M > 1$ as the shear layer results do, showing that the dimensional growth rate is not constant for $M \geq 1$. However, returning to Fig. 3.48, the normalized maximum growth rate is nearly independent of the half-radius. The point of maximum growth does not move off of the k -axis for $M > 1.2$ as it did for the shear layer cases. This indicates that the most amplified disturbance for a 2-D jet is always an axial one.

The next plot, Fig. 3.53 shows the effect of the jet half-radius on the most amplified wavenumber for various Mach numbers. Again, it is seen to be nearly independent of M for $M < 1$.

The eigenfunctions shown in Figs. 3.54 to 3.56 are all once again either symmetric or antisymmetric about the jet centerline. The disturbance has a wider effect on the flowfield as the jet half-radius increases. The flowfield disturbances are shown in the next four plots, Figs. 3.57 to 3.60. Again, they indicate regions of alternating pressure (density) along the centerline. The vortical structure is basically similar to that of the shear layers.

3.3 Combined Jet/Shear Layer Flows

The effect of superimposing a jet upon a shear layer was studied by examining profiles of the type

$$U(y) = 0.5 \tanh(ay) + U_{jet} \text{sech}^2(b(y-y_{jet}))$$

as shown in Fig. 3.61, where a and b are defined as before. King and Schetz [1] found that the size and placement of the jet on top of the shear layer can have a marked effect on the growth of the structures in the mixing layer. That situation will be discussed in a later chapter in a 3-D version of this case.

3.3.1 Effect of Jet Velocity

Figures 3.62 and 3.63 are typical profiles where the jet velocity U_{jet} is varied between 0.2 and 1.2. The next two figures show the growth rate versus the wavenumber k . There are now two dominant modes, one from the shear layer and one from the jet. Figures 3.64 and 3.65 indicate that the jet mode quickly dominates the shear layer mode as U_{jet} is increased, although the most amplified wave number of the jet mode is larger, and hence has a smaller wavelength. Thus, for reasonably sized jets, the structure is smaller but grows faster. Note that the maximum growth rate for the two modes where $U_{jet}=1.0$ agrees very closely with that of the shear layer and jet separately. This implies that the effects of the two profiles are merely superimposed at this spacing. Increasing U_{jet} also has the effect of slightly lowering the shear layer growth rate slightly. Figure 3.66 shows the maximum growth rate of both modes versus the jet velocity for both $r_{1/2}=0.02$ and $r_{1/2}=0.05$ at $y_{jet}=0.2$. The jet mode seems to dominate the shear layer mode once the jet velocity U_{jet} is increased past $10r_{1/2}$. Figure 3.67 shows the most amplified wavenumber versus the jet velocity for $y_{jet}=0.2$. The jet and shear layer mode wavenumbers are

nearly constant as the jet velocity is increased for a small jet half-radius, but they decrease with U_{jet} for larger jet half-radii.

3.3.2 *Effect of Jet Location*

Figures 3.68 and 3.69 show typical jet/shear layer profiles as y_{jet} is varied between 0.1 and 0.6 for $U_{jet}=0.4$. Figure 3.70 indicates the effect of the jet location on the growth rate of both jet and shear layer modes versus the wavenumber k for $r_{1/2}=0.02$. Both modes appear to remain nearly unchanged until y_{jet} is lowered to a point where the jet and shear layer profiles begin to overlap. At this point, the maximum growth rate and the most amplified wavenumber begin to decrease. The two modes are no longer simply superimposed, since there is now, in fact, a new hybrid profile. Figure 3.71 is the data for $r_{1/2}=0.05$. As the jet begins to merge with the shear layer, the shear layer mode growth rate first begins to decrease, then suddenly increases for $y_{jet}=0.1$. This type of effect could be responsible for the increased structure size observed by King and Schetz. These trends are clearly shown in Figs. 3.72 and 3.73.

4. Comparison with Two-Dimensional Background Flow Experiments

In order to more fully understand the behavior of shear layer mixing flows, stability calculations were performed to predict the stability characteristics in conjunction with experiments performed at the Johns Hopkins Applied Physics Laboratory by G. Sullins and H. Gilreath [39]. The aim of this analysis was to calculate the dominant wavelengths and mode shapes of amplified disturbances in the shear layer. The data should predict, at least in a qualitative manner, the size and location of dominant structures in the actual flow. If good agreement is shown by these calculations, the stability analysis can be used to design future experiments to look for mixing enhancement. This can result in a large savings of both time and money by decreasing the number of wind tunnel tests required to determine whether a particular mixing scheme is practical.

The cases studied consisted of two confined supersonic air streams. The Mach numbers of the lower and upper streams was 2.0 and 1.2, respectively, and the total temperature of both streams was 520°R. The static pressure in the two streams was varied for the five cases shown in Fig. 4.1.

4.1 Calculation of the Mean Flowfield

The stability analysis requires as input the mean velocity profile u_0 . Since the analysis requires a profile at an $x=\text{constant}$ plane, profiles at several downstream locations must be known or computed in order to study the entire flowfield. The program CFL3DE [40] was used to calculate these shear layer flowfields. This code can be used to solve the 2-D or 3-D, laminar or turbulent, Thin-Layer or Parabolized Navier-Stokes (TLNS/PNS)

equations using a finite-volume formulation. For these calculations, the code was used in the PNS mode assuming 2-D laminar flow. Laminar flow was computed to avoid having the turbulent modelling quantities appear as additional parameters in the problem. A viscous calculation was needed to enforce the no-slip conditions at the walls. Given the initial profiles at the trailing edge of the splitter plate, the solution was marched downstream. This method gives second-order accuracy in the streamwise direction. In the direction normal to the flow, third-order accuracy was achieved in the inviscid terms, but coupling with the viscous terms reduced the overall accuracy to second-order. A perfect gas equation of state was used, and 2-D flow was assumed. Since the stability code assumes constant ambient conditions along the profile in the y-direction, constant x-planes from the PNS solutions were chosen for analysis at stations in the constant pressure regions between shocks so as to minimize the effect of the pressure and density gradients from these shocks.

The solution was computed on a 481 x 100 point grid, Cartesian in the streamwise direction and stretched in the transverse direction to better capture the wall boundary layers and mixing layer. The grid generation scheme discussed previously for the stability code was used to generate the spacing. A typical grid used is shown in Fig. 4.2. This corresponded to flowfield dimensions of 12 x 2 inches. Flowfield velocity and pressure contours computed for Case 2 are superimposed in Fig. 4.3. Velocity profiles computed for several downstream planes were then used as input for the 2-D stability code. Typical profiles taken from the PNS solutions and used for the stability code are shown in Fig.

4.4. The small vertical component of the velocity was neglected in the stability code, since parallel flow was assumed.

4.2 Stability Calculations

Figure 4.5 consists of the growth rate surfaces in the k - l plane for Case 1 (matched pressure). Note, that since the relative Mach number for all of these cases was 0.8, the point of maximum growth always occurs on the k -axis, indicating that two-dimensional axial disturbances dominate the flow. These six surfaces are very similar in appearance for this case since the matched pressure flowfield has few waves to disturb the flow. Hence, the profiles at the six stations were similar.

The maximum growth rate for all five cases at all six axial stations is shown in Fig. 4.6a. The initial profile for the five cases was the same, hence the growth rate at $x=0$ is the same for all cases. For Case 3, the stream pressures were such that a Mach reflection occurred on the upper wall near the splitter plate. The PNS solver could not resolve the subsonic flow behind this normal shock, since the solution was marched, so downstream profiles were not available for this case for use in the stability code. Only the first two stations are represented for this case. It can be seen from this figure that for Cases 2 and 3 (the overexpanded cases), the growth rate decreased from that of the baseline case, while Cases 4 and 5 (the underexpanded cases) had increased growth rates. This agrees well with the spreading rates measured experimentally. For all cases, the stability code showed that the majority of the growth occurs after the initial adjustment shocks, which tended to equalize the pressure between the streams, which then remains

nearly constant. In order to compare the computed growth rates with the measured spreading rates, Sullins and Gilreath normalized the growth rates and spreading rates by the values from the baseline matched pressure case (Case 1). These values are shown in Fig. 4.6b. The dotted line represents the condition where the two methods would correlate exactly. Except for Case 3, the plot indicates that there is good agreement between the theory and the experiment. That is, the stability code correctly predicted the cases for which the spreading rate was found to increase over the baseline case. The discrepancies, especially in Case 3, might be attributed to several factors. Primarily, for this case, the upper stream was highly overexpanded, which violates the assumption of constant pressure. Also, after the initial adjustment wave there is a significant vertical velocity component, and the parallel flow assumption is no longer valid.

5. Stability Code for Three-Dimensional Background Flows

5.1 Problem Formulation

Three-dimensional parallel flows can be analyzed in a very similar manner to two-dimensional flows if the background velocity profile is taken to be a function of both y and z . One important difference in the three-dimensional case is the presence of the wall boundary conditions in the z -direction. The walls restrict the propagation of the disturbance to the x -direction only, eliminating the z -wavenumber, l , from the disturbance equations. Thus, all of the disturbances for three-dimensional profiles are assumed to be axial. The governing disturbance equations become

$$\begin{aligned} ik(u_0 - c)\rho + iku + \frac{\partial v}{\partial y} + \frac{\partial w}{\partial z} &= 0 \\ \frac{ik}{M^2}\rho + ik(u_0 - c)u + \frac{\partial u_0}{\partial y}v + \frac{\partial u_0}{\partial z}w &= 0 \\ \frac{1}{M^2}\frac{\partial \rho}{\partial y} + ik(u_0 - c)v &= 0 \\ \frac{1}{M^2}\frac{\partial \rho}{\partial z} + ik(u_0 - c)w &= 0 \end{aligned}$$

or in matrix form,

$$\begin{bmatrix} iku_0 & ik & D_y & D_z \\ \frac{ik}{M^2} & iku_0 & \frac{\partial u_0}{\partial y} & \frac{\partial u_0}{\partial z} \\ \frac{1}{M^2}D_y & 0 & iku_0 & 0 \\ \frac{1}{M^2}D_z & 0 & 0 & iku_0 \end{bmatrix} \begin{bmatrix} \rho \\ u \\ v \\ w \end{bmatrix} = -\sigma \begin{bmatrix} \rho \\ u \\ v \\ w \end{bmatrix}$$

Again these can be written in nonlinear form as

$$(u_0 - c) \left(\frac{\partial^2 \rho}{\partial y^2} + \frac{\partial^2 \rho}{\partial z^2} \right) - 2 \left(\frac{\partial u_0}{\partial y} \frac{\partial \rho}{\partial y} + \frac{\partial u_0}{\partial z} \frac{\partial \rho}{\partial z} \right) + k^2 (u_0 - c) (M^2 (u_0 - c)^2) \rho = 0.$$

The form of the nonlinear problem remains very similar to the 2-D case, although the order of the problem has now increased, and the coefficient matrices A_i gain additional terms.

A grid refinement study, similar to the 2-D study discussed previously, was done for the 3-D code. Similar results were obtained, in that about fifty grid points in each of the two directions was required to achieve accurate convergence to the correct growth rate solution using the nonlinear solver. Due to memory storage limitations on the IBM 3090 computer, the size of the grid for the linear portion of the code was kept to around 31 x 31 points. This number of grid points was adequate for the nonlinear routine to converge. Calculation times were measured, and as expected, were significantly greater than for the 2-D code. Typically, the time for computing a 3-D linear solution was on the order of nine hundred CPU seconds for a 31 x 31 grid, and approximately 2 msec per grid point

per iteration for the nonlinear portion. The nonlinear routine usually converged to a residual of 10^{-6} in three to five iterations.

5.2 Use of the Method to Investigate Hybrid Injection Schemes

The full three-dimensional stability problem can be used to study a wide range of potential injection schemes. Examples include planar shear layers and jets as before, but now with the presence of walls in the cross-flow dimension, as well as many hybrid schemes including arrays of jets, combined axial jet/shear layer flows, and other shear flows. The stability code allows us to vary the spacing and geometry of the profiles over a large range of parameters with relative ease. This in turn will allow intelligent decisions about what configurations to actually test in wind tunnel experiments. King and Schetz [1] found that some cases of combined normal and tangential injection into a supersonic stream can produce substantially enhanced mixing rates and large eddy structures. The geometry and flow parameters had a marked effect on the amount of mixing enhancement, but the exact combination of parameters that produced the augmentation could only be found by tedious "trial and error" experiments. The use of the 3-D stability code will help better understand the interaction of the flow elements.

6. Results for Three-Dimensional Background Flows

6.1 Comparison of 2-D and 3-D Shear Layers and Jets

In order to more fully understand the two-dimensional results discussed in Chapter 3, some of the same profiles were examined using the three-dimensional stability code. The difference now is the added presence of walls in the z -dimension. It is expected that this will not have a large effect on the gross stability characteristics of the flows studied with the 2-D code, but may change some of the details.

6.1.1 Shear Layers

Shear layers with nominal momentum thickness, but now constrained into the region $-0.5 \leq z \leq 0.5$ were examined for Mach numbers of 0.5, 1.0, and 1.5. Figure 6.1 shows a typical numerical grid for these flows, with the grid points concentrated in the region of high velocity gradients. The results are plotted in Fig. 6.2. For wavenumbers less than $|\omega|_*$, the growth rate for the three-dimensional case is seen to be the same as for the two-dimensional case. For larger wavenumbers, however, the 3-D growth rate is less than that of the 2-D cases. This is undoubtedly due to side wall effects, since that is the only new element that has been introduced. Figure 6.3 shows the flowfield vorticity disturbance for $M=0.5$ at the most amplified wavenumber of $k=6.5$. The contours in the y - z plane indicate the form of the vorticity eigenfunction. Note, that the eigenfunction is now a function of both y and z . For this spectral component, it is seen that the greatest amount of vorticity is generated where the shear layer meets the z boundaries, and not in the middle of the flow. Recall that this is only one mode of the disturbance, although it

is the most highly amplified. The contours in the x-y planes at $z=0$ and $z=-0.5$ are also shown. They show the periodic nature of the disturbances in the x direction. The apparent lack of regularity in each period is due to the discretization of the eigenfunction in the x-direction. Since the size of the domain in this direction (2π) is not always an exact multiple of the wavelength of the disturbance, the number of points in each period is not constant. The disturbance for $M=1.0$ shown in Fig. 6.4 has a similar structure, but at a slightly smaller wavenumber. Since the vortex structure at this wavenumber is slightly larger, the disturbance on the $z=-0.5$ wall extends a little further in the y direction than before. Also note that there is more of a corner effect in evidence and that the vorticity is relatively stronger in the center of the flow domain than before.

Figure 6.5 is for the $M=1.5$ case at a wavenumber of $k=4.5$. The wall effect extends completely up and down the side walls now and joins with the corner vorticity. The vorticity in the center of the flow is also now much larger compared to the vorticity at the walls.

From these last three figures it seems that as the relative Mach number is increased, the dominant structure size increases (the wavenumber decreases), and more vorticity is generated away from the walls. The walls seem to have a dampening effect on the large-scale structure. The fact that the corner effect only is apparent in the upper corner is due to the asymmetry of the shear layer velocities.

6.1.2 Planar Jets

The 3-D stability code was also used to compare 2-D and 3-D planar jets. This grid is similar to those generated for the shear layer cases above. A comparison of the growth rates for planar jets is shown in Fig. 6.6. Similar to the shear layers, the growth rate is nearly identical to the 2-D cases except at the largest wavenumbers.

6.2 Fully Three-Dimensional Profiles

6.2.1 3-D Jet/Shear Layers

Figure 6.7 shows the vorticity eigenfunction for the first fully three-dimensional profile examined. The case is for a nominal 2-D shear layer with $M=1.5$, $\theta=0.03$, and a round jet with $r_{1/2}=0.05$. Again, we see the wall effects dominate at this wavenumber, $k=1$, which is not the most amplified wavenumber for this case. Also, the vorticity in the middle of the shear layer is no longer uniform between the sidewalls. This is due to the presence of the jet above the shear layer. The fact that the vorticity from the axisymmetric jet is not axisymmetric is probably an artifact of the grid spacing in the immediate vicinity of the jet. The next plot, Fig. 6.8, is the flowfield vorticity disturbance associated with the previous eigenfunction in Fig. 6.7.

The next case in this section is the same as the previous case, but for the most amplified wavenumber of $k=4.5$. In Fig. 6.9, it is clear that the vorticity in the shear layer now dominates the flow. Also, the jet has much less influence at this wavenumber, and the wall effects are less pronounced. The flowfield vorticity disturbance is shown in Fig.

6.10, and it shows the same features as observed in the eigenfunction shown in the previous figure.

Figures 6.11 and 6.12 are the vorticity eigenfunction and flowfield disturbance for the jet/shear layer case corresponding to the 2-D case where a large increase in the growth rate was observed (see Fig. 3.71). Notice, in Fig. 6.11 the shear layer vorticity clearly dominates this mode.

6.2.2 3-D Jets

Three-dimensional jets were also studied using the stability code. A typical numerical grid used is shown in Fig. 6.13. The aspect ratio of the jets is defined as $AR = z_{1/2}/y_{1/2}$, where $y_{1/2}$ and $z_{1/2}$ are the half-radii in the y- and z-directions. Figure 6.14 shows the growth rate versus wavenumber for several jets of different geometries at $M=1.0$. All of these growth rates are significantly lower than those found for planar jets (AR approaching infinity). Other values of M were examined, with similar results. From this plot, we see that the effect of reducing the aspect ratio is to increase the stability of the flow. As $AR \rightarrow 1$, the jet becomes neutrally stable, and no unstable modes were found using this code. This result agrees with that of Shen [41], who showed mathematically that inviscid axisymmetric jets are stable even though they possess an inflection point.

7. Conclusions

In this study, the stability characteristics of compressible free shear layers have been examined using linear stability theory. A reliable and efficient method for solving the stability equations governing the disturbances was developed and used successfully to find the growth rates, most amplified wavenumbers, and directions of propagation of disturbances for several two- and three-dimensional mean flow profiles.

The relative Mach number (in this study, equal to twice the convective Mach number) was shown to be the single most important parameter to characterize the stability of compressible mixing flows. The maximum growth rate of all profiles under study was found to decrease with increasing relative Mach number, and the form of this dependence was found for several cases. The normalized maximum growth rate was shown to be independent of the momentum thickness for shear layers, and of the half-radius for jets and wakes. For the jets, it was also seen that the most amplified wavenumber is also independent of the half-radius.

The most amplified wavenumber of the disturbances was found to be nearly independent of the relative Mach number for values of $M < 1$. For shear layer flows, the propagation angle of the most amplified wavelength was found to be zero for $M < 1.2$, and closely approximated by $M \cos \phi = 1.2$ for $M \geq 1.2$. For jet flows, it was found that all of the most amplified disturbances are two-dimensional.

The eigenfunctions were calculated for each disturbance and found to vary widely, depending on the wavenumber and relative Mach number. The jet eigenfunctions were

found to be symmetric or antisymmetric for all cases studied. The full flowfield disturbances were calculated from the eigenfunctions, and they proved to be great assistance in picturing the form of the vorticity disturbances in the flow. The placement of the upper wall was examined and was shown not to influence the growth rate of the disturbances until it came within two or three characteristic widths of the shear layer or jet, although it did have some effect on the eigenfunctions, tending to push the maximum point down towards the lower wall.

The effect of superimposing profiles was slight except to include both the shear layer and jet modes, unless the portions of the two profiles started to overlap, forming a new type of profile. This superposition result might be expected, since the governing equations were linearized. However, for some cases where the profiles merged, an increase in the maximum growth rate was observed. This confirmed qualitatively experimental results seen by King and Schetz.

Flowfield calculations for shear layers with pressure mismatch were performed with the code CFL3DE to compute velocity profiles for use in the stability code. The cases studied corresponded to experimental cases studied by Sullins and Gilreath. The velocity profiles were examined to determine which of the test cases might have improved mixing compared to the baseline case. The stability results were compared with the experimentally measured spreading rates and found to give good qualitative agreement.

A three-dimensional version of the stability code was also developed and compared for simple cases with the two-dimensional code. When applicable, the 3-D

results gave excellent agreement with the 2-D stability code. Also, potentially important side wall effects were seen when shear layers were examined with the 3-D code.

Fully three-dimensional velocity profiles were also examined with the stability code. Three-dimensional jets were superimposed above a shear layer to closely approximate the experimental flows studied by King and Schetz. Cases where the growth rate increased significantly were again found.

Axisymmetric and elliptic jets were found to have much lower growth rates than 2-D planar jets. In fact, the axisymmetric jets were found to be stable at all wavenumbers examined. As the jet aspect ratio was increased, the growth rate increased rapidly and approached the characteristics of a planar jet.

References

1. King, P.S., "Combined Tangential-Normal Injection Into A Supersonic Flow", AIAA J. of Propulsion and Power, vol. 7, no. 3, May-June 1991, pp. 420-30.
2. Bogdanoff, D.W., "Compressibility Effects on Turbulent Shear Layers", AIAA J., vol. 21, no. 6, 1983, pp. 926-27.
3. Papamoschou, D. and Roshko, A., "Observations of Supersonic Free Shear Layers", AIAA 86-0162, January 1986.
4. Ragab, S.A. and Wu, J.L., "Instabilities in the Free Shear Layer Formed by Two Supersonic Streams", AIAA 88-0038, January 1988.
5. Tam, C.K.W., and Hu, F.Q., "Instabilities of Supersonic Mixing Layers Inside a Rectangular Channel", AIAA 88-3675, July 1988.
6. Zhuang, M., Kubota, T., and Dimotakis, P.E., "On the Instabilities of Inviscid, Compressible Free Shear Layers", July 1988.
7. Lele, S.K., "Direct Numerical Simulation of Compressible Free Shear Flows", AIAA 89-0374, January 1988.
8. Landau, L., "On The Problem of Turbulence", C.R. Academy of Science, USSR, vol. 44, 1944, p. 311.
9. Pai, S.I., "On The Stability of Two-Dimensional Laminar Jet Flow", J. Aeronautical Science, vol. 18, 1951, pp. 731-42.
10. Hatanaka, "On The Stability of a Surface of Discontinuity in a Compressible Fluid" (in Japanese), H., J. Soc. Sci. Culture Japan, vol. 2, 1949, pp. 3-7, cited in App. Mechanics Review, vol. 2, 1949, p. 158.
11. Miles, J.W., "On the Disturbed Motion of a Plane Vortex Sheet", JFM, vol. 4, 1958, pp. 538-52.
12. Blumen, W., "Shear Layer Instabilities of an Inviscid Compressible Fluid", JFM, vol. 40, 1970, pp. 769-81.
13. Blumen, W., Drazin, P.G., and Billings, D.F., "Shear Layer Instabilities of an Inviscid Compressible Fluid, Pt. 2", JFM, vol. 71, 1975, pp. 305-16, 1975.

14. Drazin, P.G. and Davey, A., "Shear Layer Instabilities of an Inviscid Compressible Fluid, Pt 3.", JFM, vol. 82, 1977, pp. 255-60.
15. Michalke, A., " On the Inviscid Instability of the Hyperbolic Tangent Velocity Profile", JFM, vol. 19, 1964, pp. 543-56.
16. Ragab, S.A. and Wu, J.L., "Instabilities of Supersonic Shear Flows", AIAA 90-0712, January 1990.
17. Schubauer, G.B. and Skramstad, H.K., J. Aeronaut. Sci., vol. 14, pp. 69-78, 1947; also NACA Report 909.
18. Laufer, J. and Vrebalovich, T., Proc. 9th Int. Congr. Appl. Mech., vol. 4, pp.121-31, 1957; Jet Propulsion Lab. Report 20-116, 1958; J. Fluid Mech., vol. 9, pp. 257-99, 1960.
19. Riley, J.J. and Metcalfe, R., "Direct Numerical Simulation of a Perturbed Mixing Layer", AIAA 80-0274, January 1980.
21. Sandham, N. and Reynolds, W., "The Compressible Mixing Layer: Linear Theory and Direct Simulation", AIAA 89-0371, January 1989.
20. McMurtry, P.A., Jou, W.H., Riley, J.J., and Metcalfe, R.W., "Direct Numerical Simulations of a Reacting Mixing Layer with Chemical Heat Release", AIAA J., vol. 24, no. 6, 1986, pp. 962-70.
22. Soetrisno, M., Eberhardt, D.S., Riley, J.J., and McMurtry, P.A., "A Study of Inviscid Supersonic Mixing Layers Using a Second-Order TVD Scheme", AIAA 88-3676, July 1988.
23. Gilreath, H.E. and Sullins, G.A., "Investigation of the Mixing of Parallel Supersonic Streams", Proceedings 9th ISABE Conference, Athens, Greece, 1989.
24. Greenough, J., Riley, J., Soetrisno, M., and Eberhardt, D., "The Effects of Walls On a Compressible Mixing Layer", AIAA 89-0372, January 1989.
25. White, F.M., *Viscous Fluid Flow*, McGraw Hill, 1974.
26. Rayleigh, Lord, *Sci. Papers*, vol. 1, pp. 474-87, Cambridge University Press, 1880.

27. Lessen, M., "On the Stability of Free Laminar Boundary Layer Between Parallel Streams", NACA Report 979, 1950.
28. Curle, N., "On the Hydrodynamic Stability in Unlimited Fields of Viscous Flow", Proc. Royal Soc. London A238, pp. 489-501, 1957.
29. Tatsumi, T. and Kakutani, T., "The Stability of a Two-Dimensional Laminar Jet", JFM, vol. 4, 1958, pp. 261-75.
30. Koshigoe, S. and Tubis, A., "Wave Structures in Jets of Arbitrary Shape. I. Linear Inviscid Spatial Instability Analysis", Phys. Fluids, vol. 29, no. 12, December 1986.
31. Koshigoe, S. and Tubis, A., "Wave Structures in Jets of Arbitrary Shape. II. Application of a Generalized Shooting Method to Linear Instability Analysis", Phys. Fluids, vol. 30, no. 6, June 1987.
32. Baty, R.S. and Morris, P.J., "Instability of Jets of Arbitrary Geometry", AIAA 89-1796, June 1989.
33. Morris, P.J., Giridharan, M.G., and Viswanathan, K., "Turbulent Mixing in Plane and Axisymmetric Shear Layers", AIAA 90-0708, January 1990.
34. Malik, M.R., "Numerical Methods for Hypersonic Boundary Layer Stability", J. Comp. Physics, vol. 86, no. 2, February 1990.
35. Lin, C.C., *The Theory of Hydrodynamic Stability*, Cambridge University Press, 1967.
36. Anderson, D.A., Tannehill, J.C., and Pletcher, R.H., *Computational Fluid Mechanics and Heat Transfer*, McGraw-Hill, 1984.
37. Gourlay, A.R. and Watson, G.A., *Computational Methods for Matrix Eigenproblems*, John Wiley and Sons, 1973.
38. Wilkinson, J.H., *The Algebraic Eigenvalue Problem*, Oxford University Press, 1965.
39. Sullins, G.A., Gilreath, H.E., Mattes, L.A., King, P.S., and Schetz, J.A., "Instabilities in Confined Supersonic Mixing Layers", Proceedings 10th ISABE Conference, Nottingham, England, 1991.

40. Newsome, R.W., Walters, R.W., and Thomas, J.L., "An Efficient Iteration Strategy for Upwind Relaxation Solutions to the Thin-Layer Navier-Stokes Equations", AIAA J., vol. 27, no. 9, pp. 1165-66, September 1989; also AIAA 87-1113-CP, June 1987.
41. Shen, S.F., "Stability of Laminar Flows", in *Theory of Laminar Flows*, Vol. IV, High Speed Aerodynamics and Jet Propulsion, Princeton University Press, 1964, pp. 719-853.

Figures

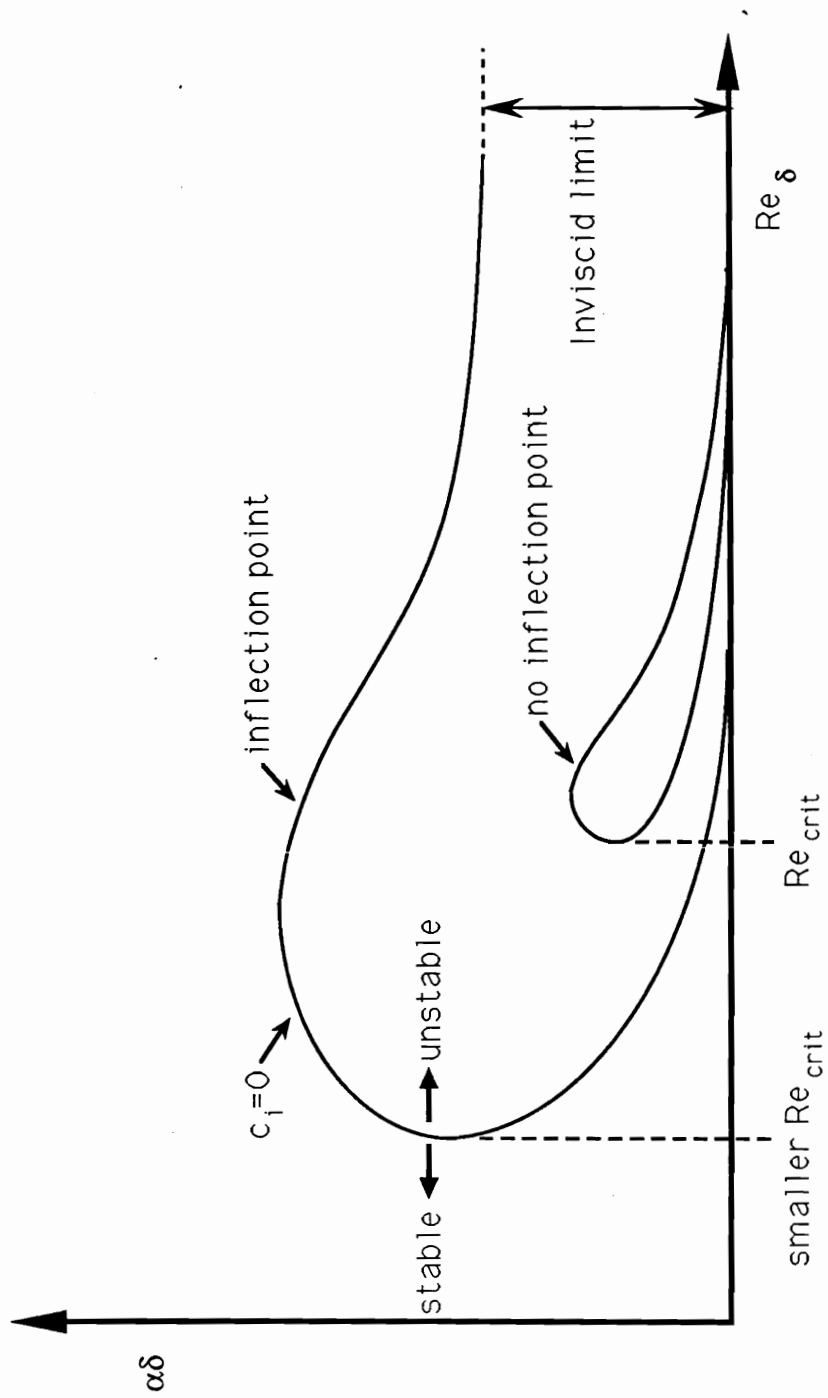


Figure 1.1 Neutral curves of the Orr-Sommerfeld equation; from White [25]

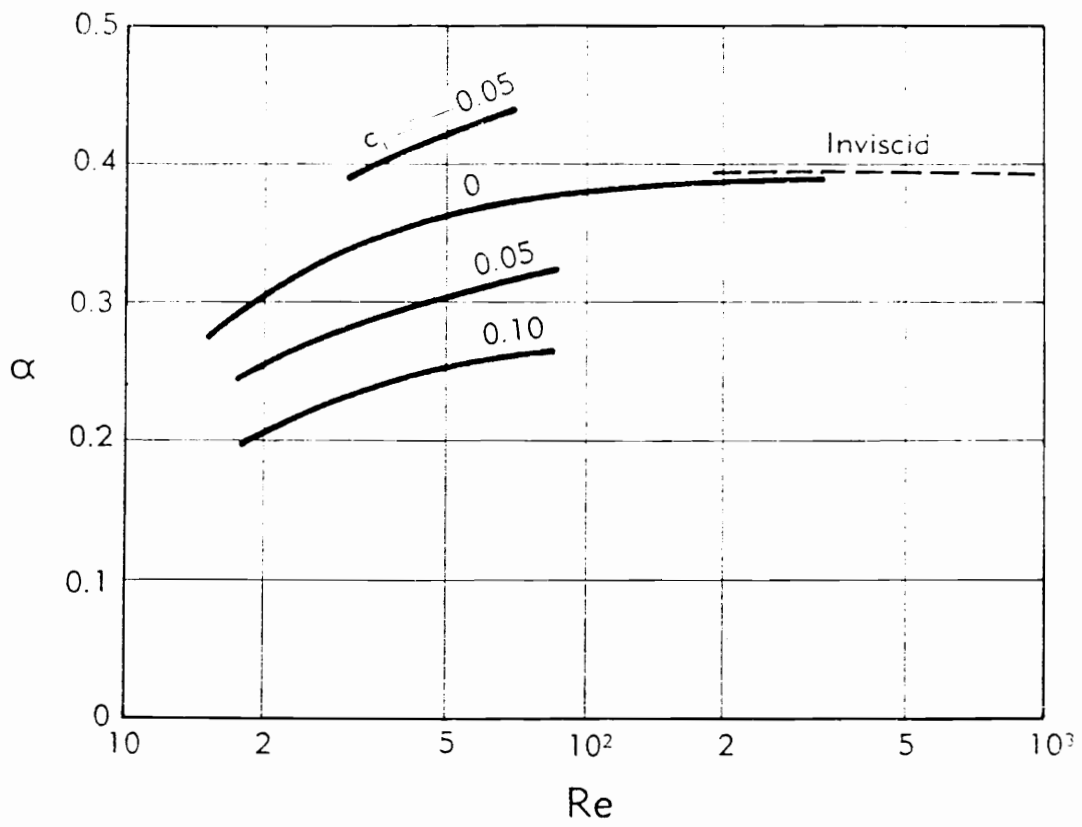


Figure 1.2 Stability of mixing between two parallel compressible flows; from Shen [41]

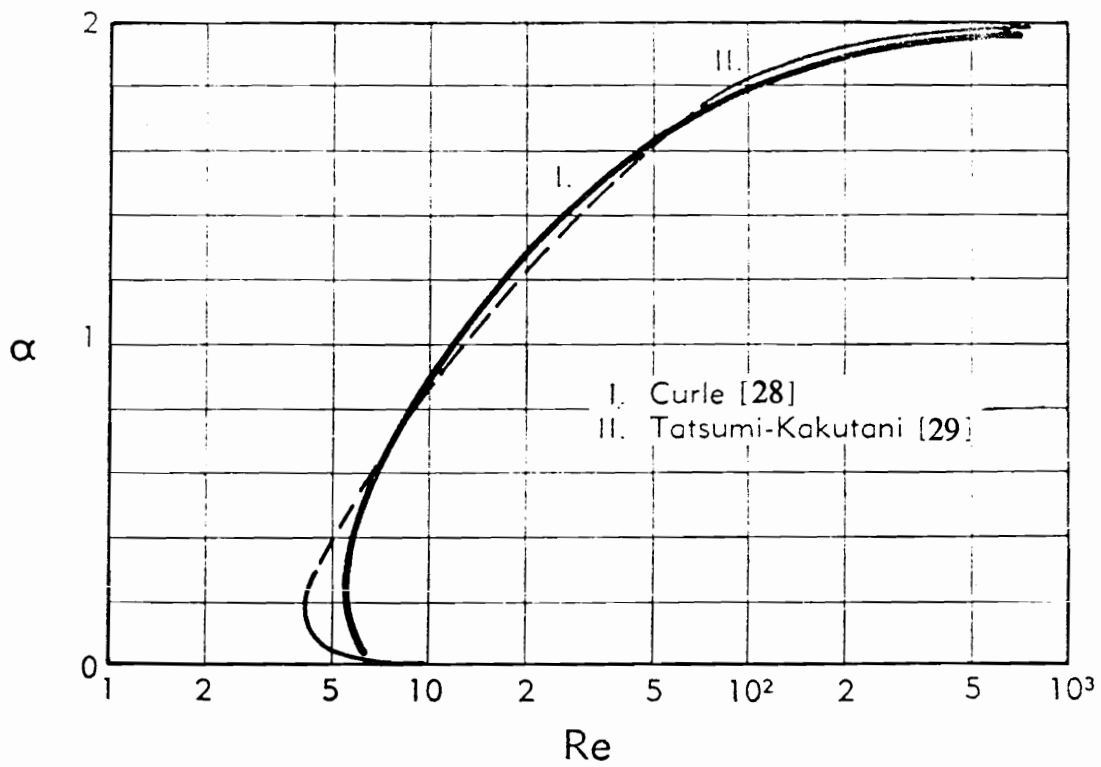


Figure 1.3 Neutral stability curve for compressible planar jets; from Shen [41]

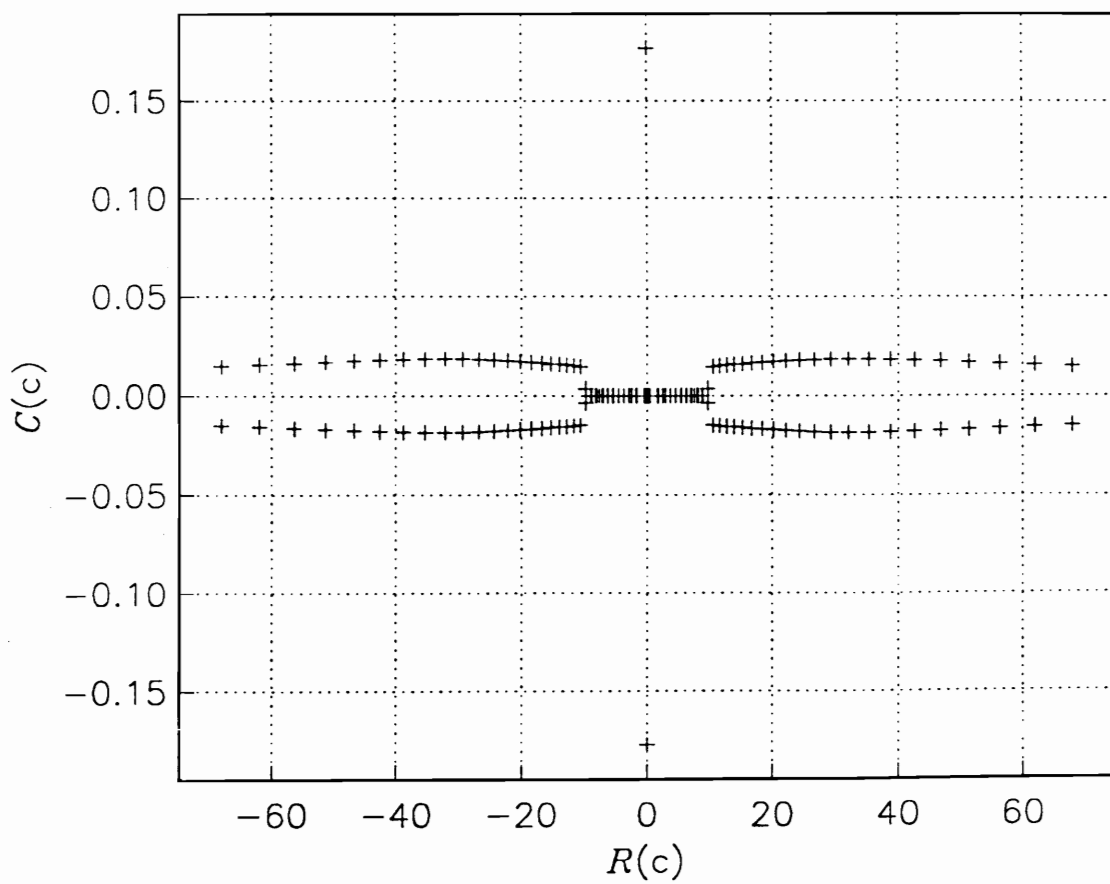


Figure 2.1 Eigenvalue spectrum: $M=0.5$, $\theta=0.05$, $k=3.0$

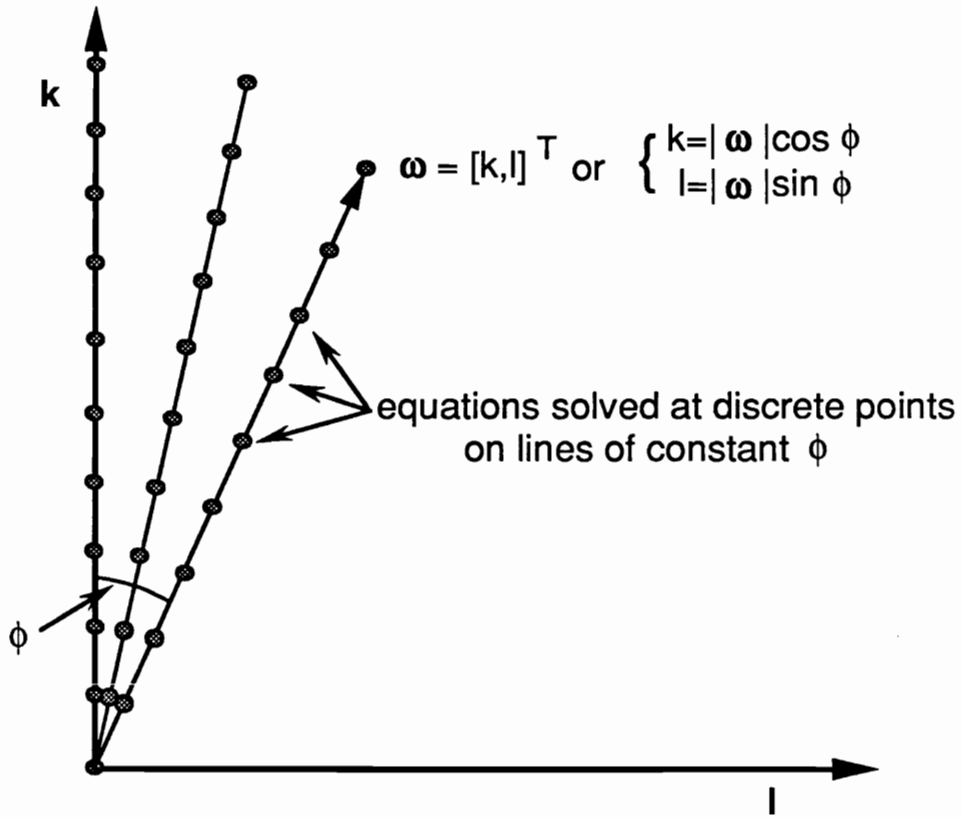


Figure 2.2 Computational k-l wavenumber plane

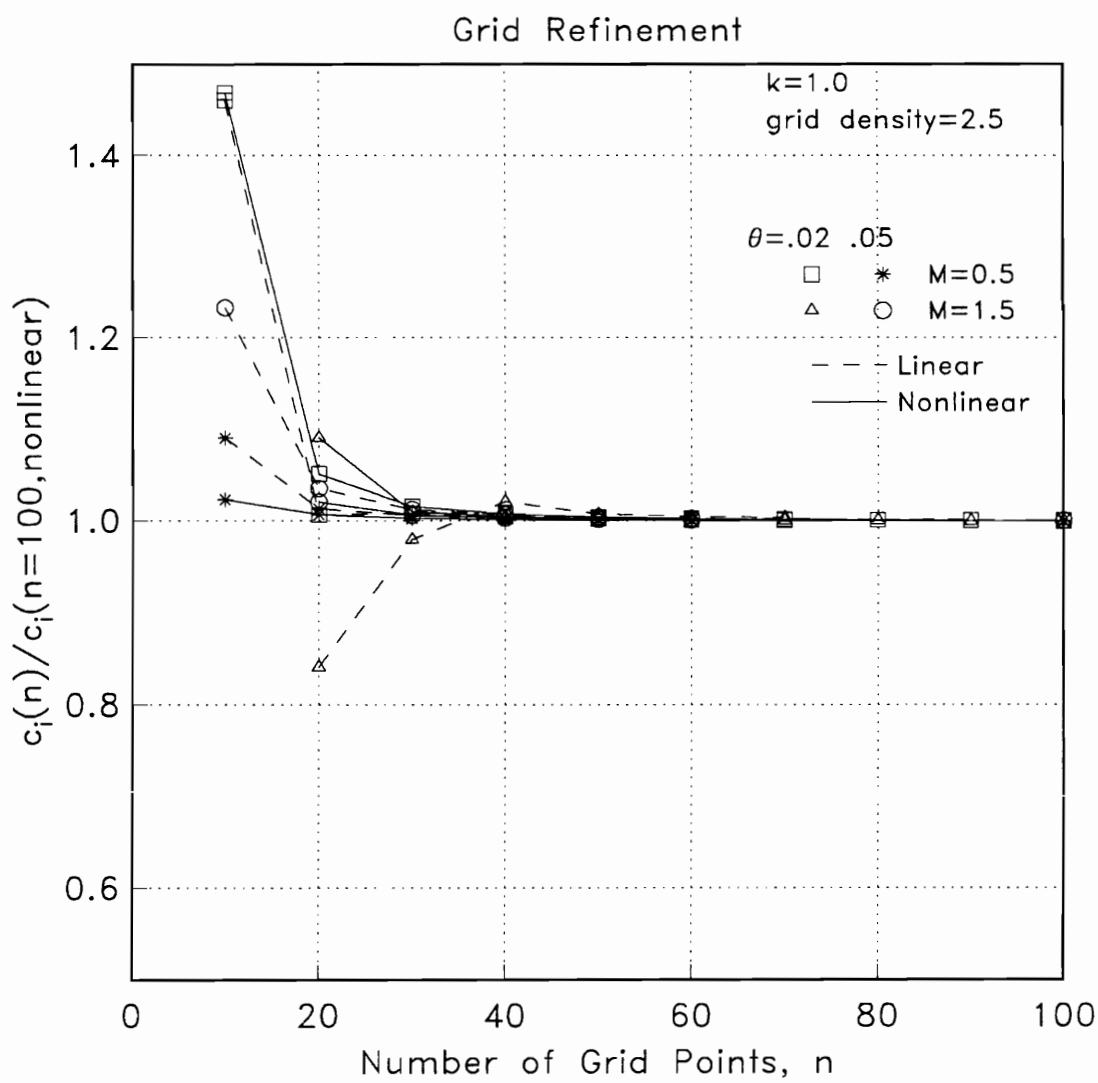


Figure 2.3 Grid refinement study: imaginary part of c for $M=0.5$ and 1.5 ,
 $\theta=0.02$ and 0.05

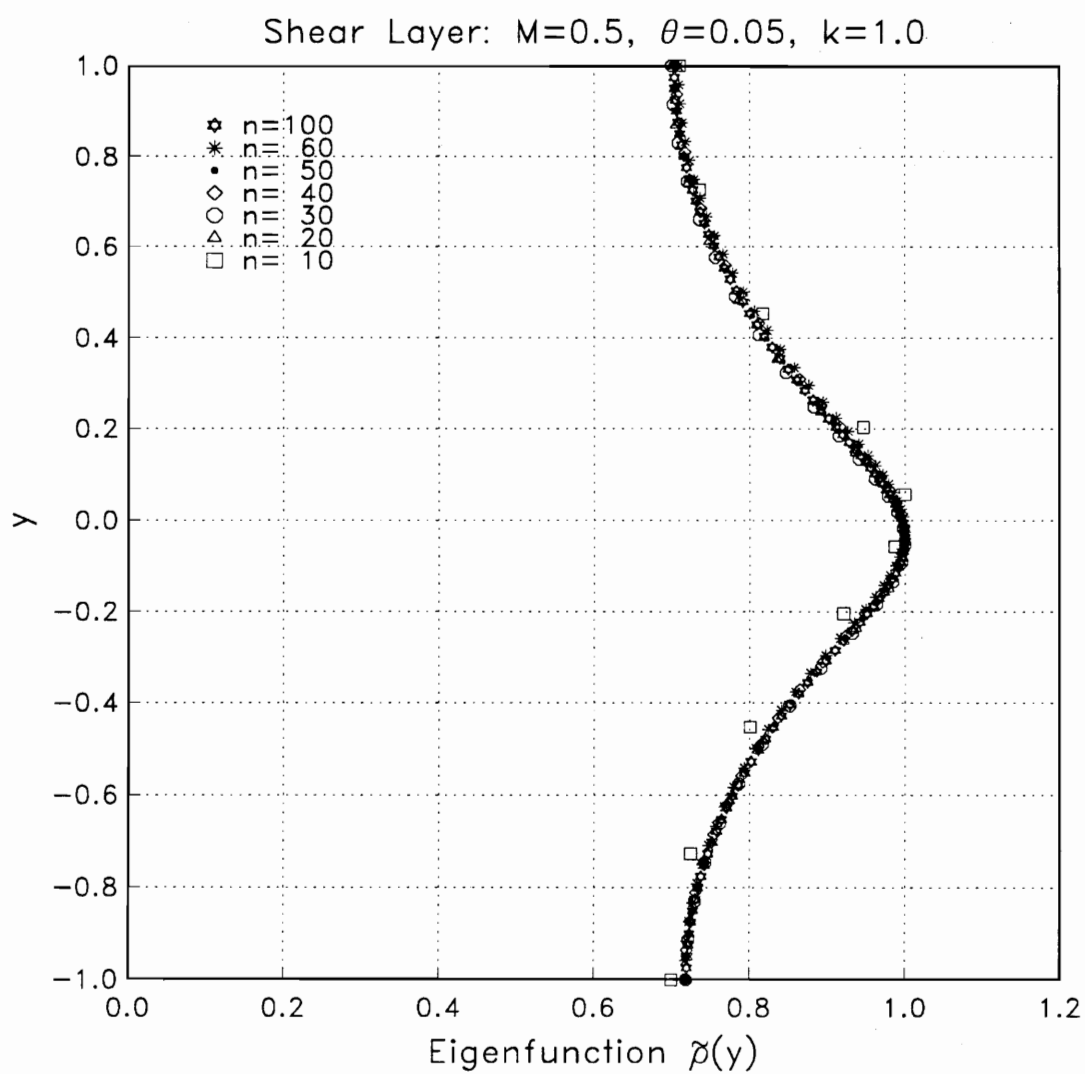


Figure 2.4 Grid refinement study: density eigenfunctions

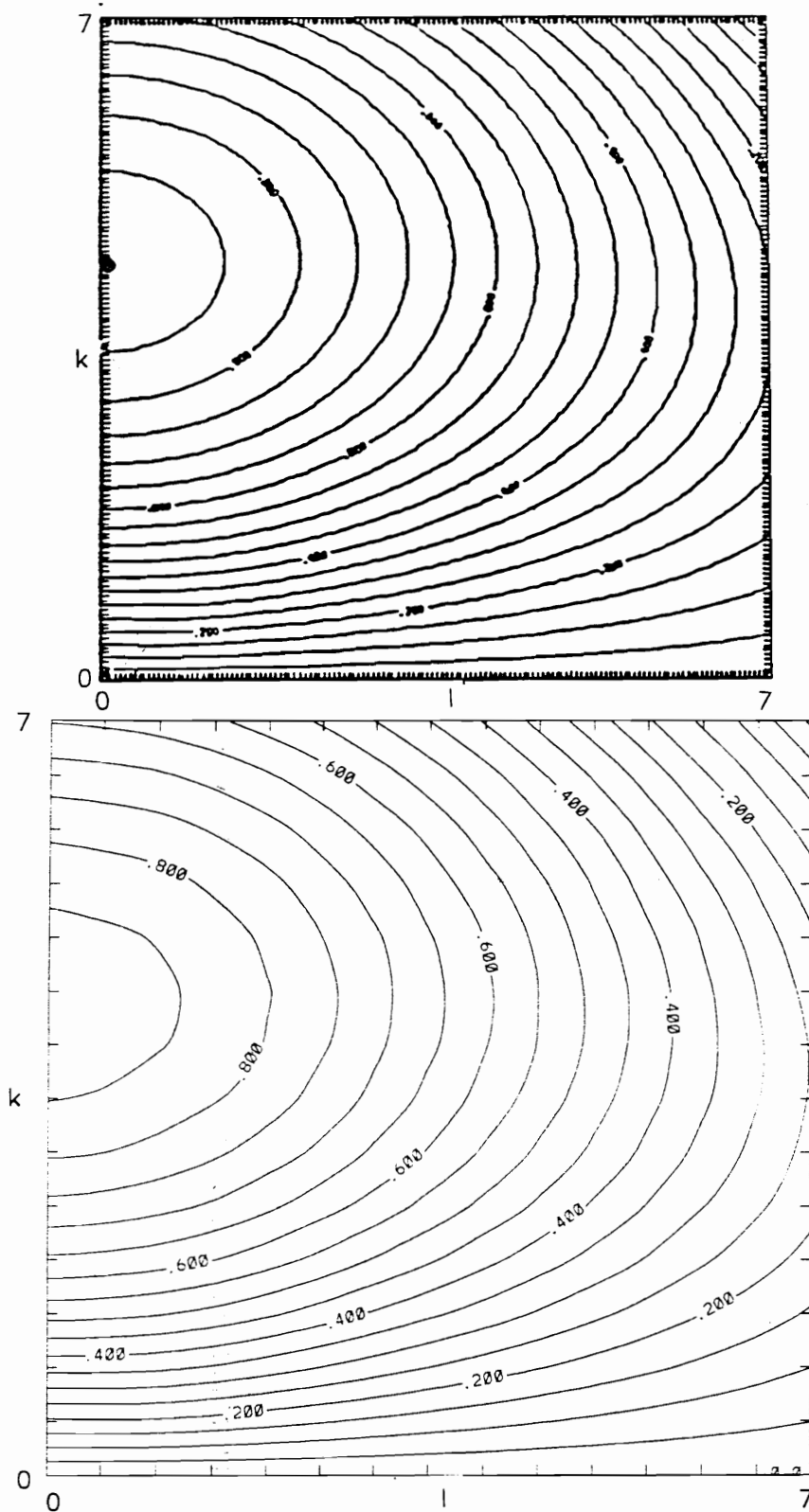


Figure 3.1 Shear layer: $M=0.5$, $\theta=0.03$; (a) from Greenough et al. [24],
(b) 2-D stability code

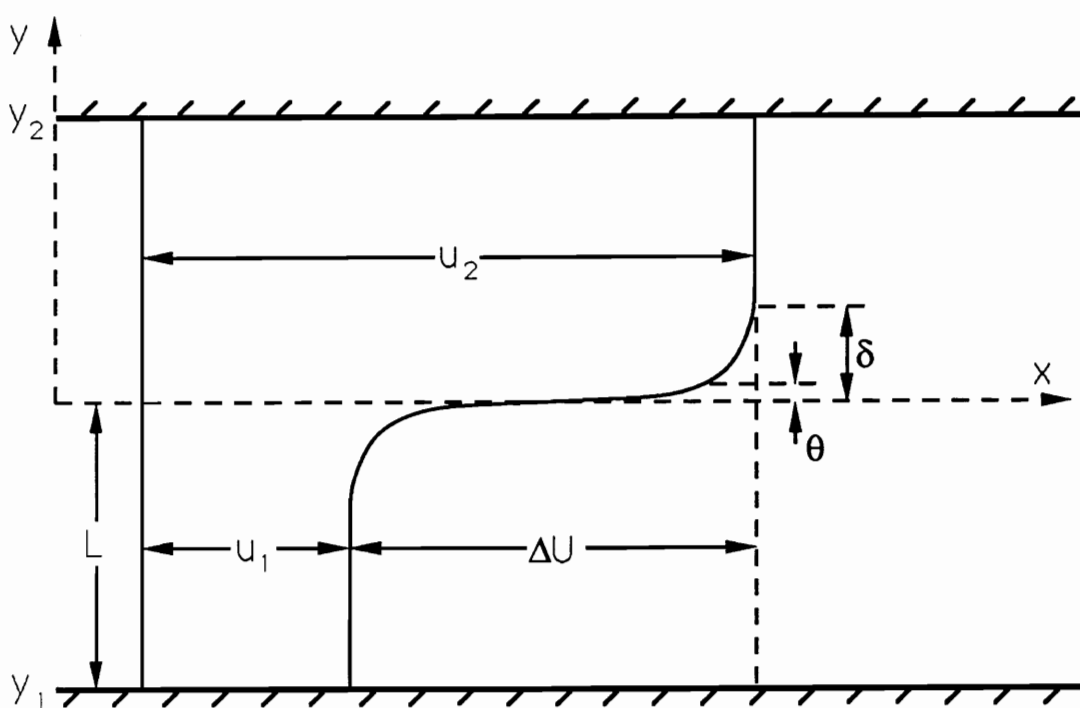


Figure 3.3 Typical shear layer flowfield parameters

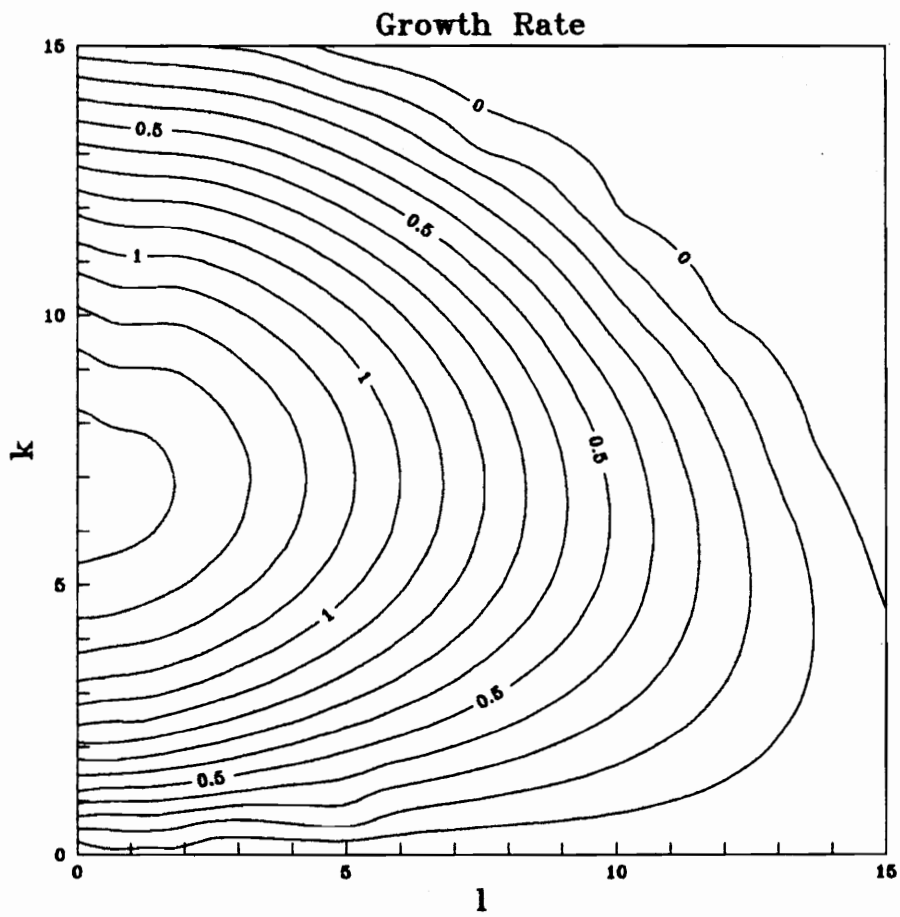


Figure 3.4 Shear layer growth rate surface: $\theta=0.02$, $M=0.05$, $d=1.0$

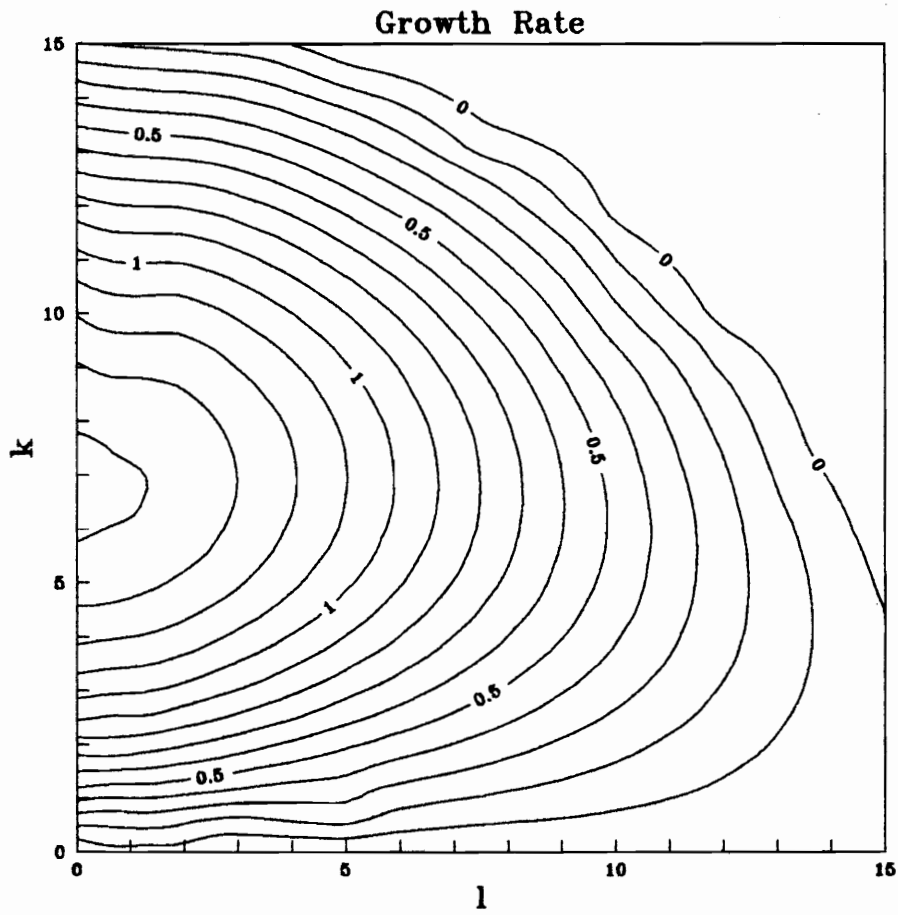


Figure 3.5 Shear layer growth rate surface: $\theta=0.02$, $M=0.25$, $d=1.0$

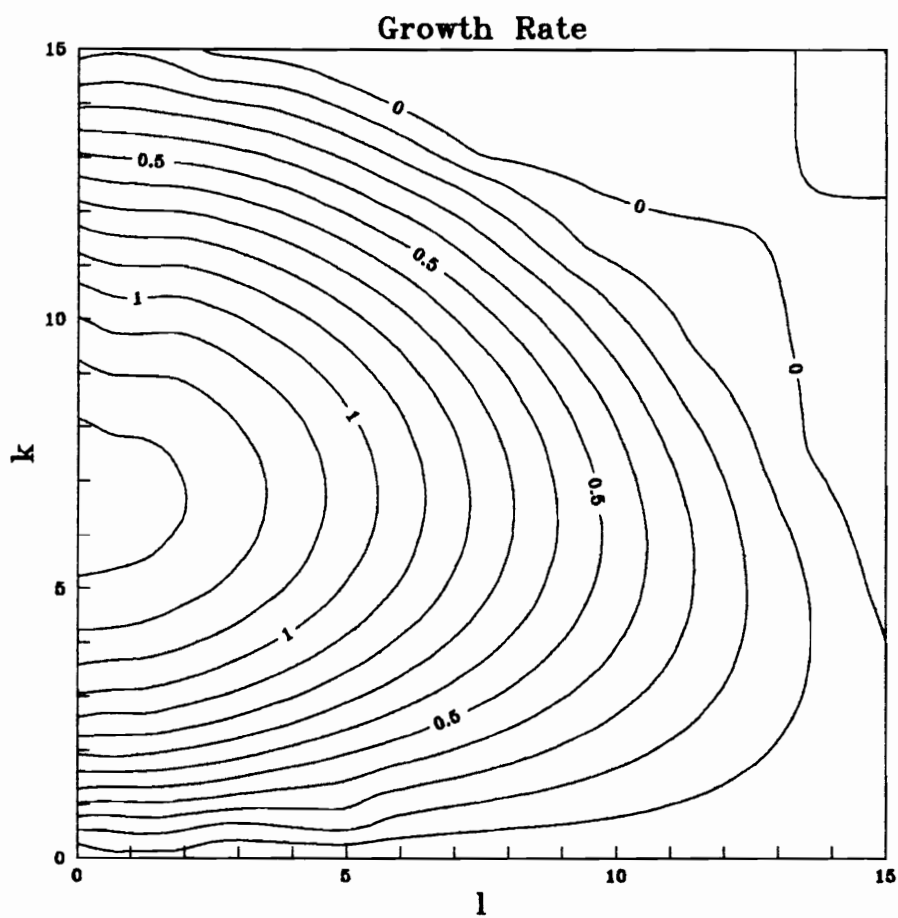


Figure 3.6 Shear layer growth rate surface: $\theta=0.02$, $M=0.50$, $d=1.0$

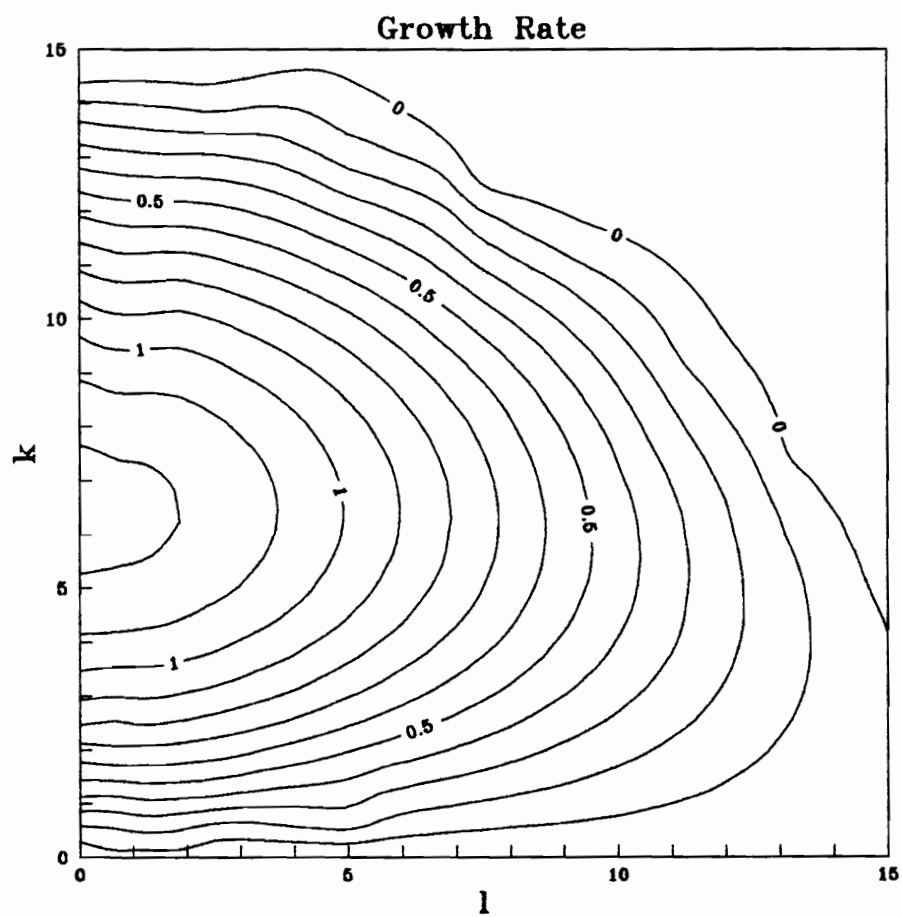


Figure 3.7 Shear layer growth rate surface: $\theta=0.02$, $M=0.75$, $d=1.0$

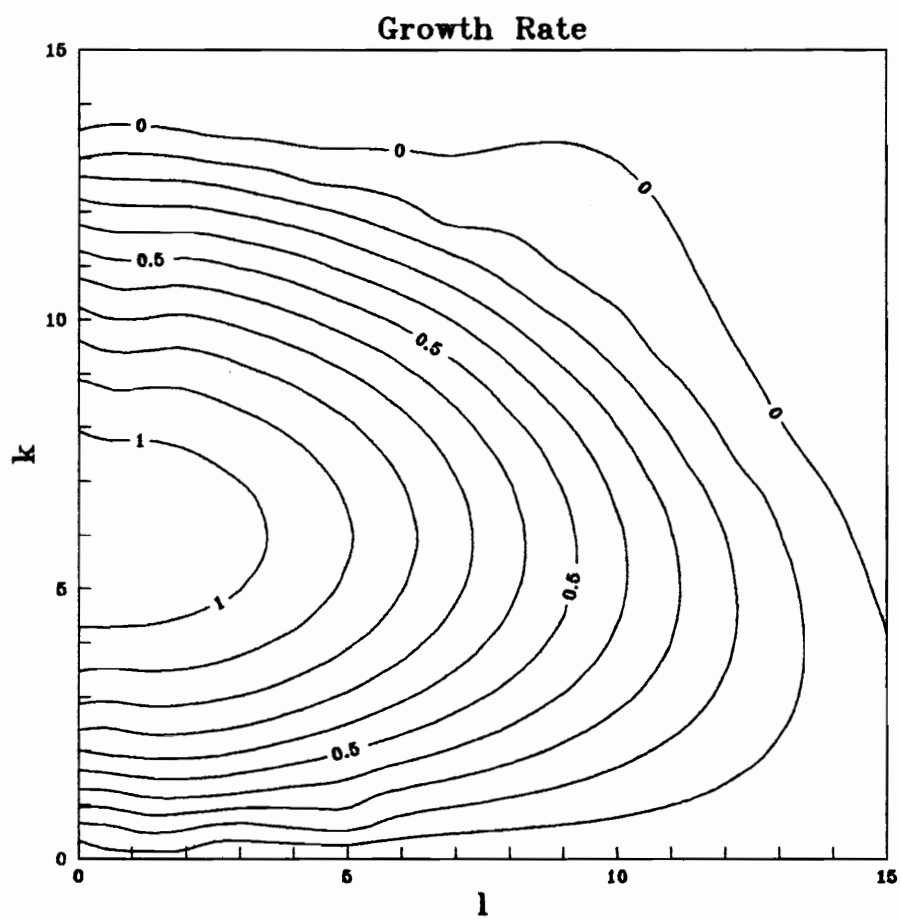


Figure 3.8 Shear layer growth rate surface: $\theta=0.02$, $M=1.00$, $d=1.0$

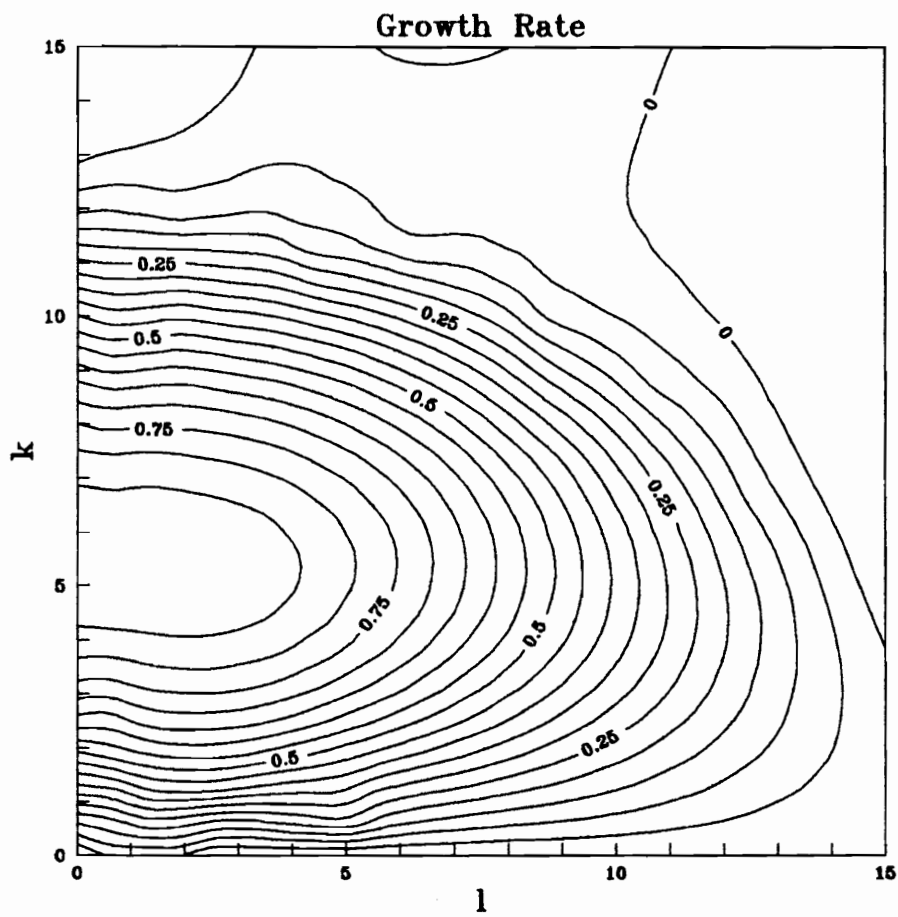


Figure 3.9 Shear layer growth rate surface: $\theta=0.02$, $M=1.25$, $d=1.0$

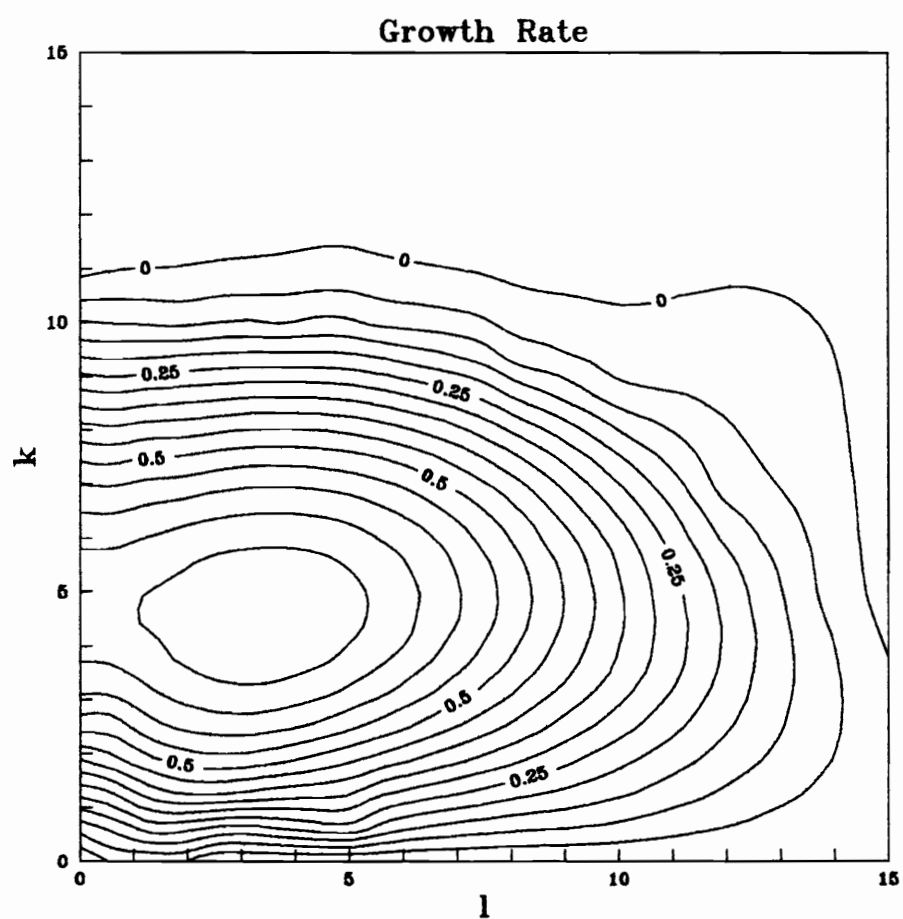


Figure 3.10 Shear layer growth rate surface: $\theta=0.02$, $M=1.50$, $d=1.0$

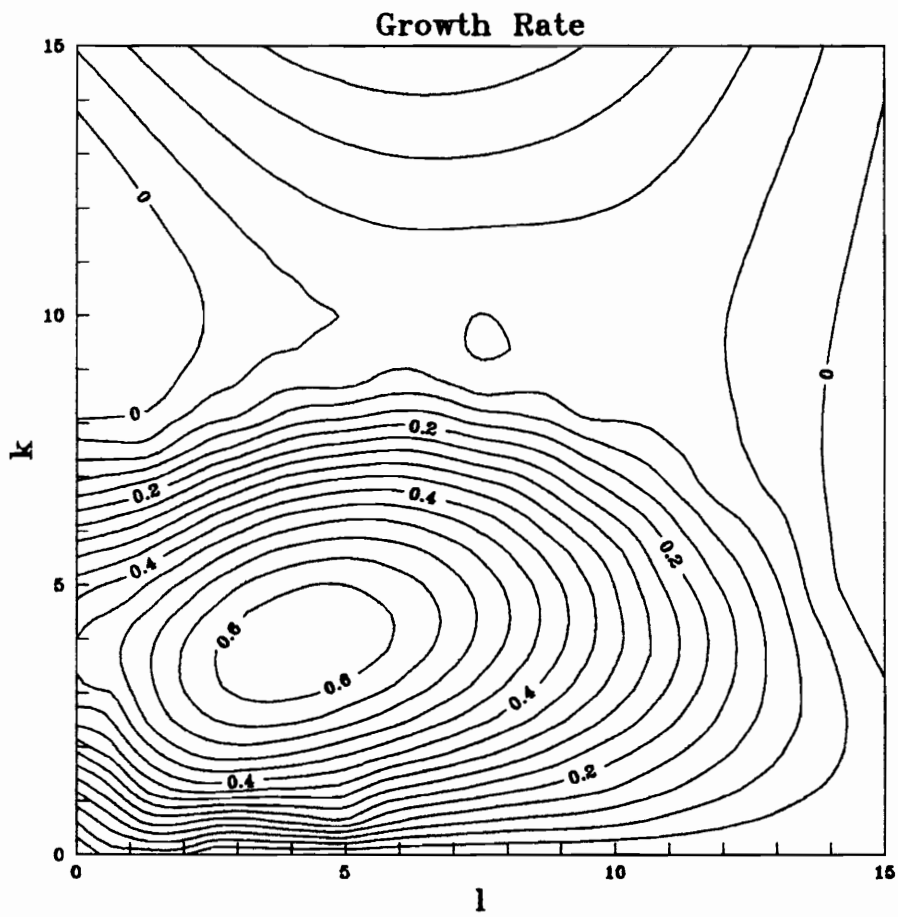


Figure 3.11 Shear layer growth rate surface: $\theta=0.02$, $M=1.75$, $d=1.0$

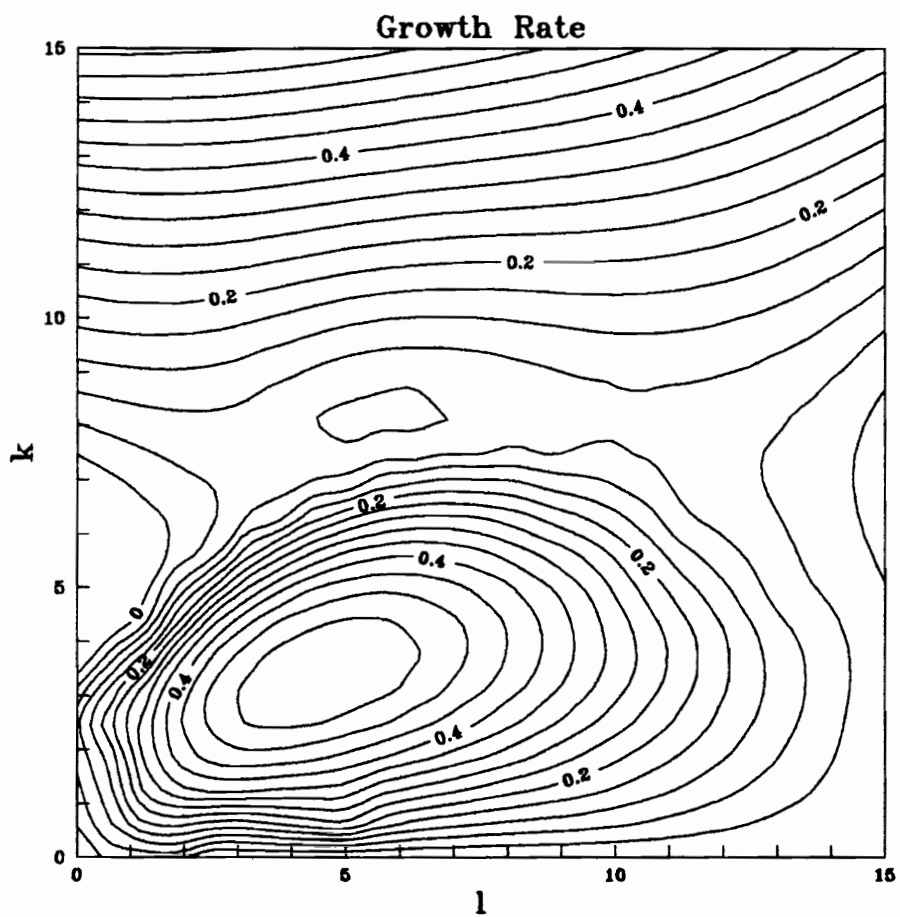


Figure 3.12 Shear layer growth rate surface: $\theta=0.02$, $M=2.00$, $d=1.0$

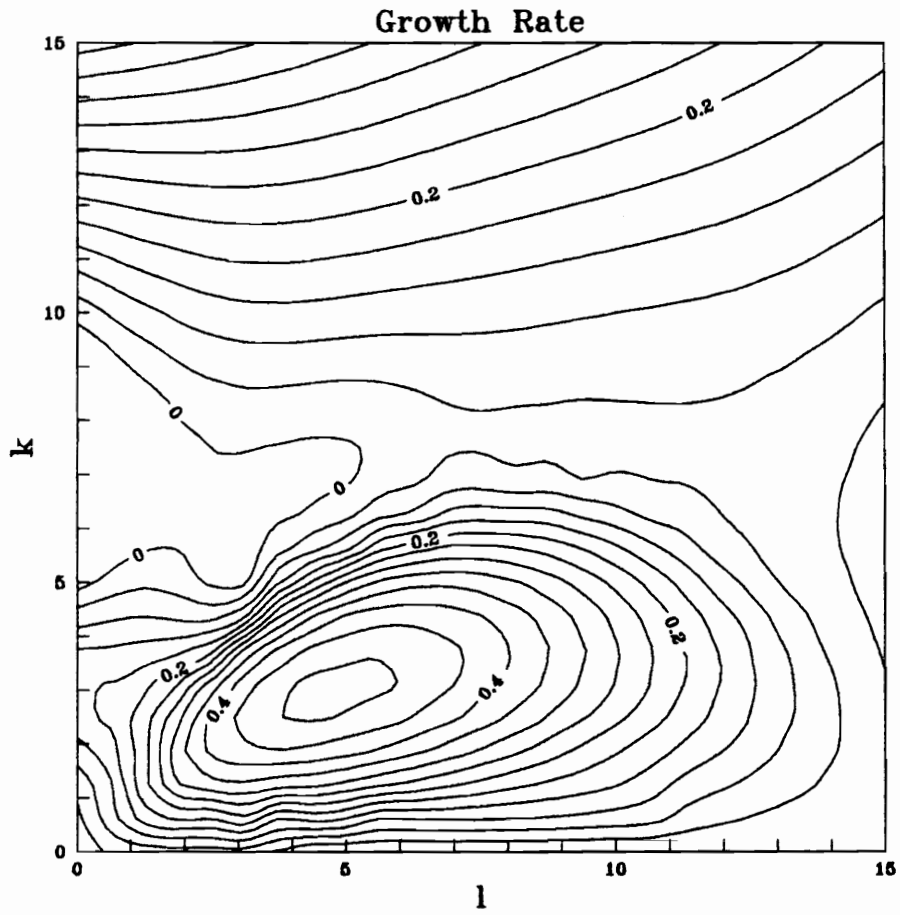


Figure 3.13 Shear layer growth rate surface: $\theta=0.02$, $M=2.25$, $d=1.0$

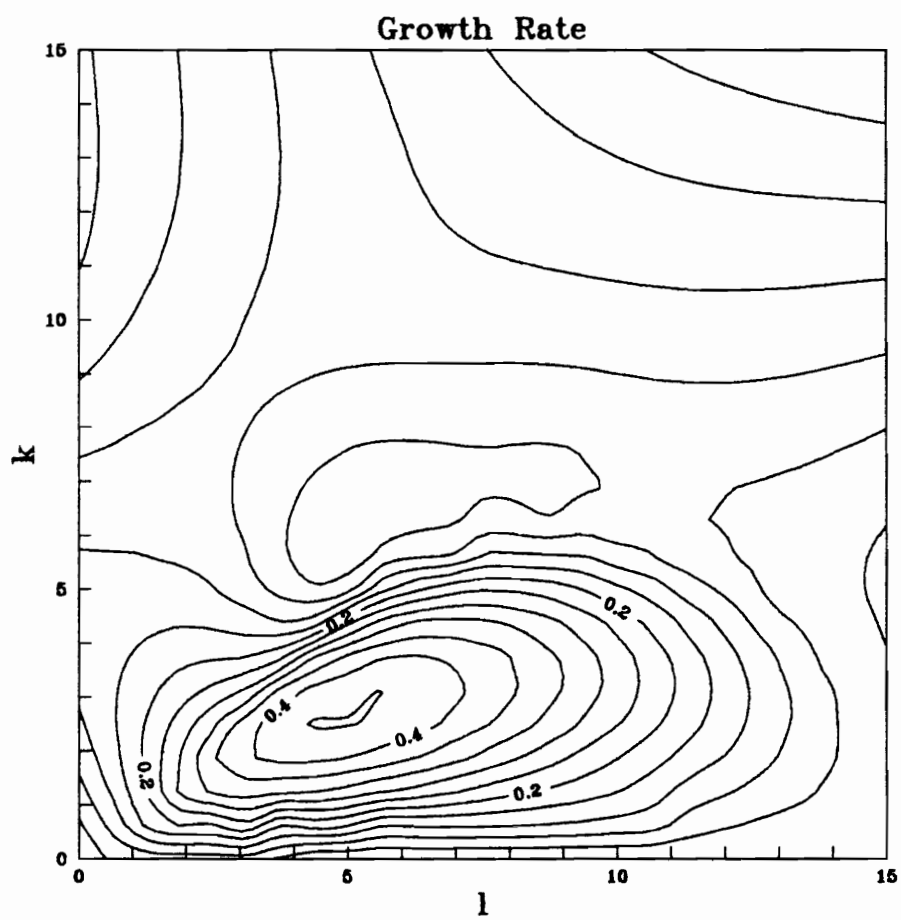


Figure 3.15 Shear layer growth rate surface: $\theta=0.02$, $M=2.75$, $d=1.0$

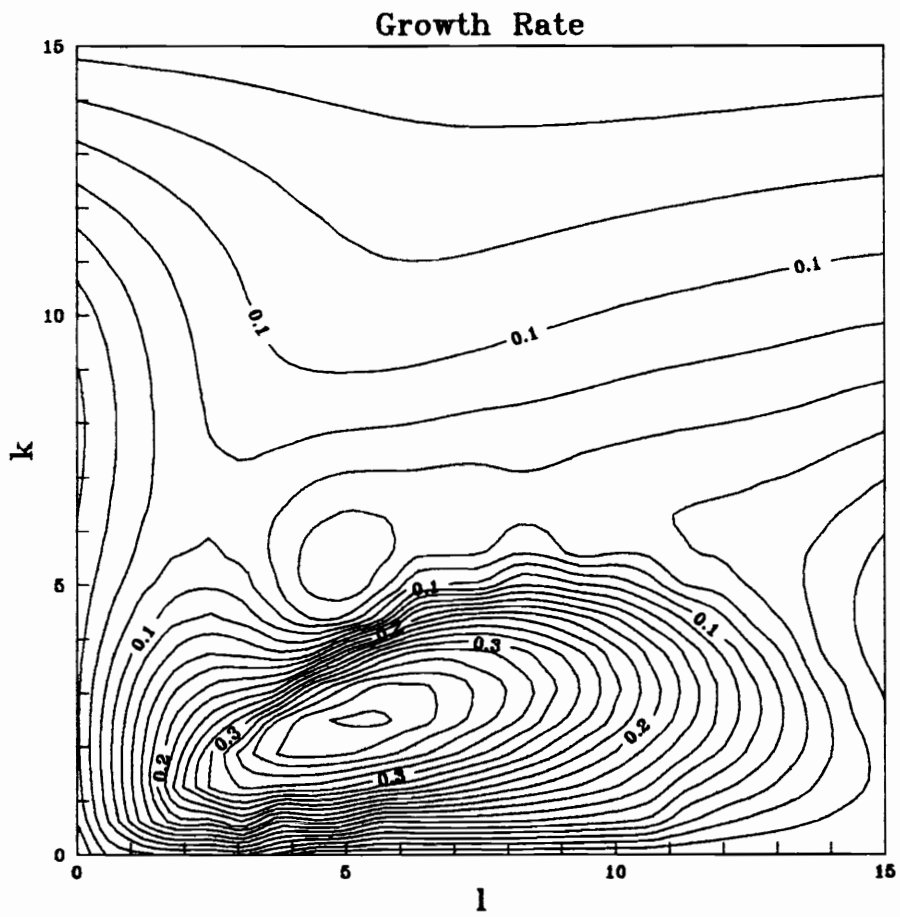


Figure 3.14 Shear layer growth rate surface: $\theta=0.02$, $M=2.50$, $d=1.0$

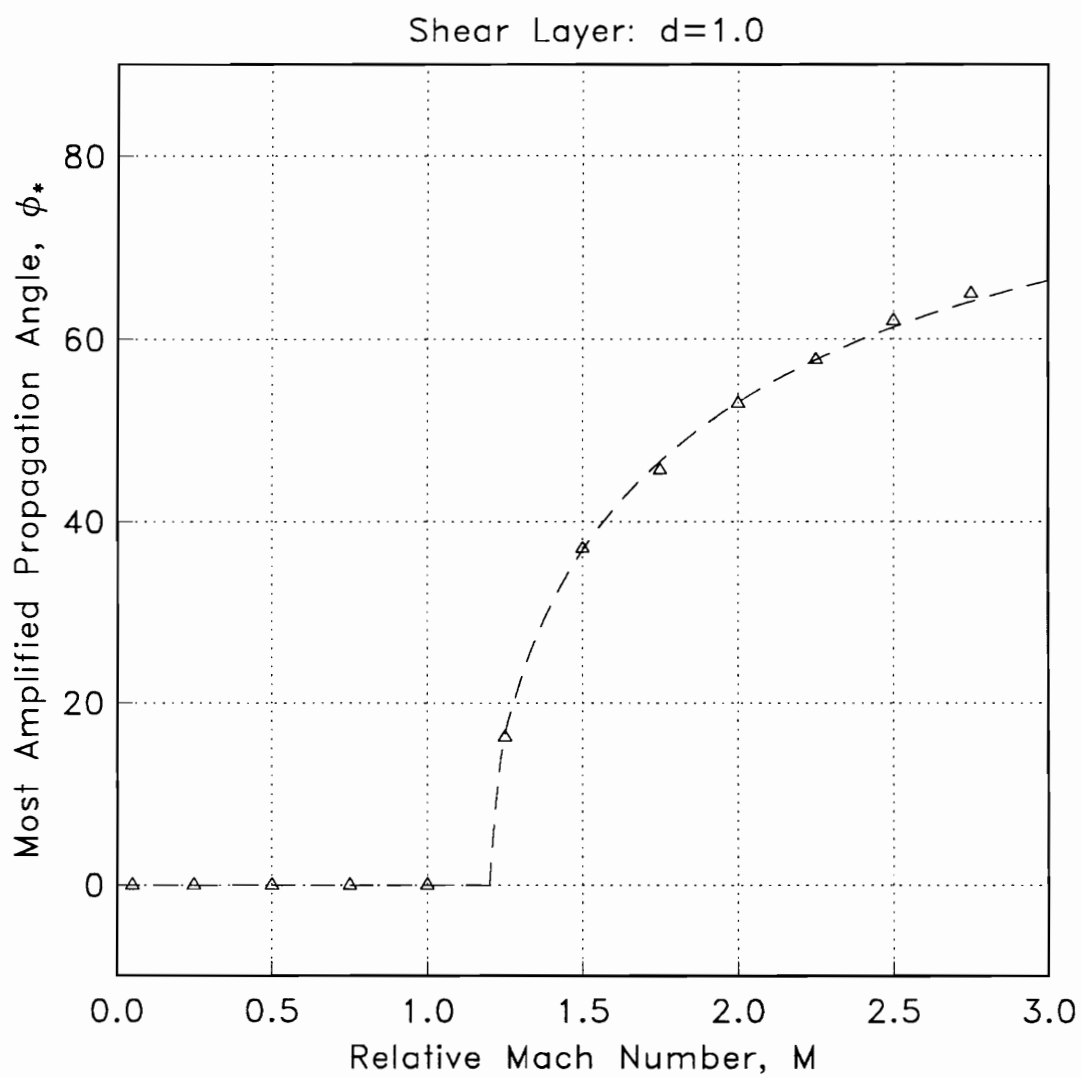


Figure 3.16 Shear layer most amplified propagation angle vs. relative Mach number

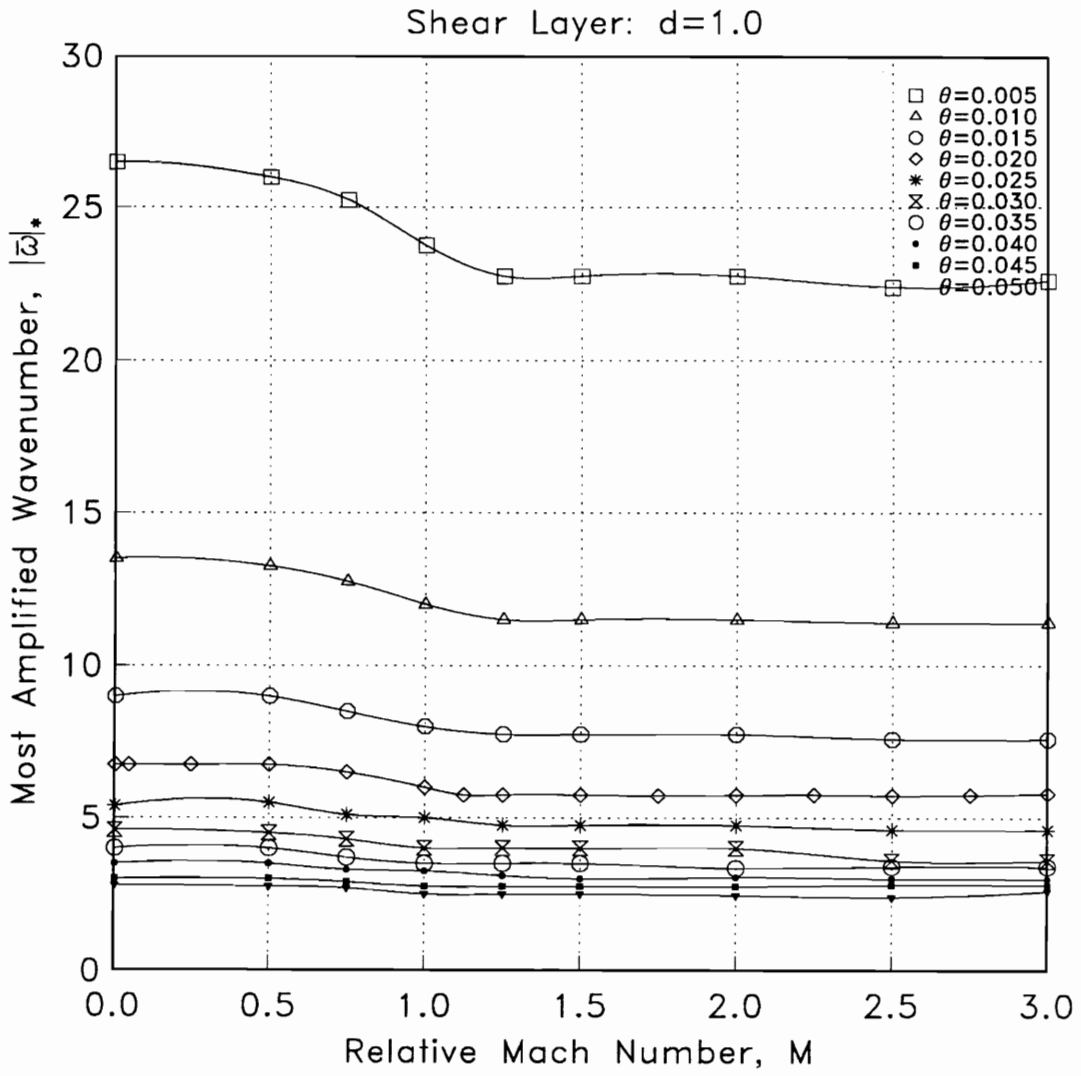


Figure 3.17 Shear layer most amplified wavenumber vs. relative Mach number

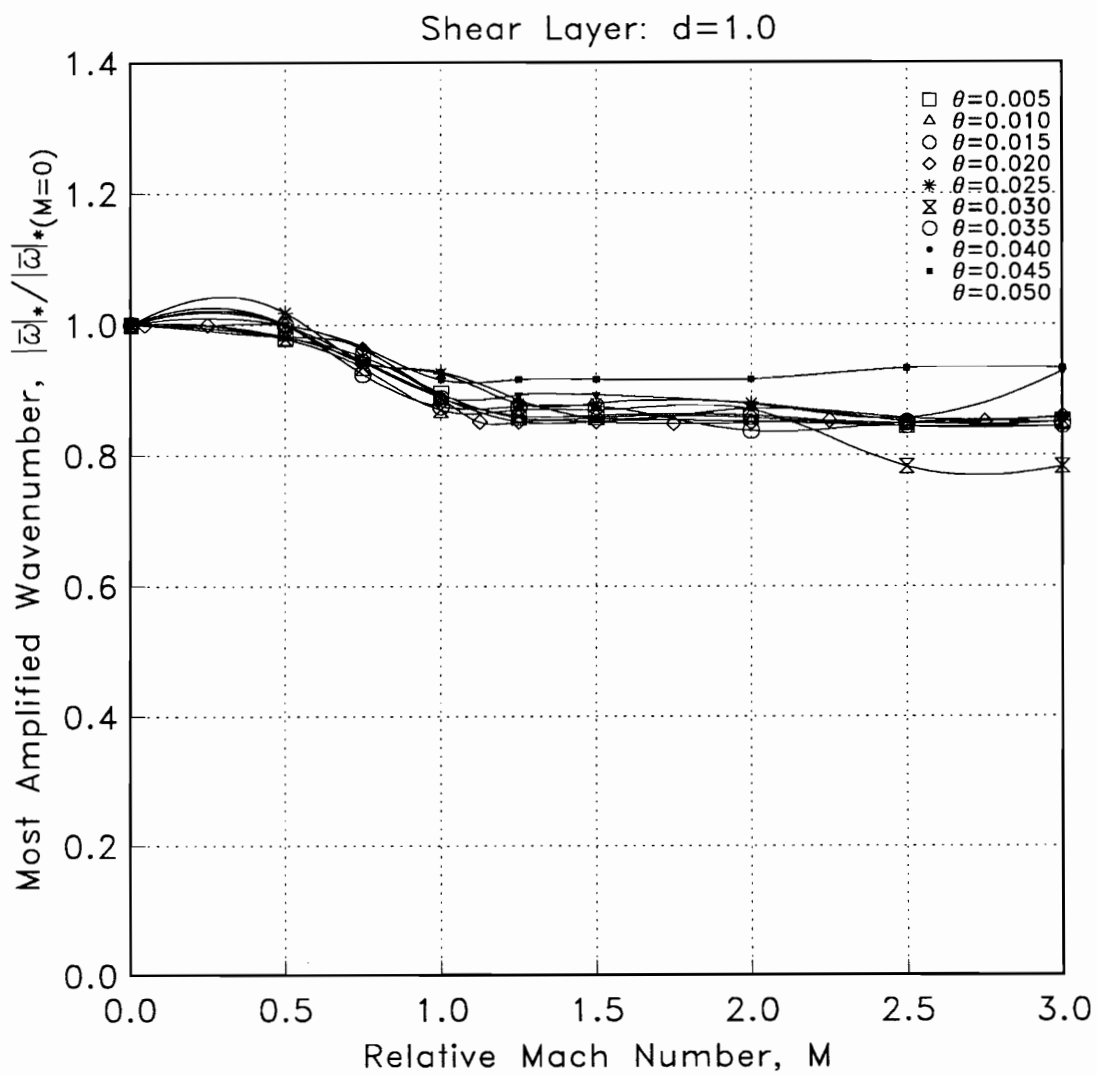


Figure 3.18 Shear layer most amplified wavenumber (collapsed) vs. relative Mach number

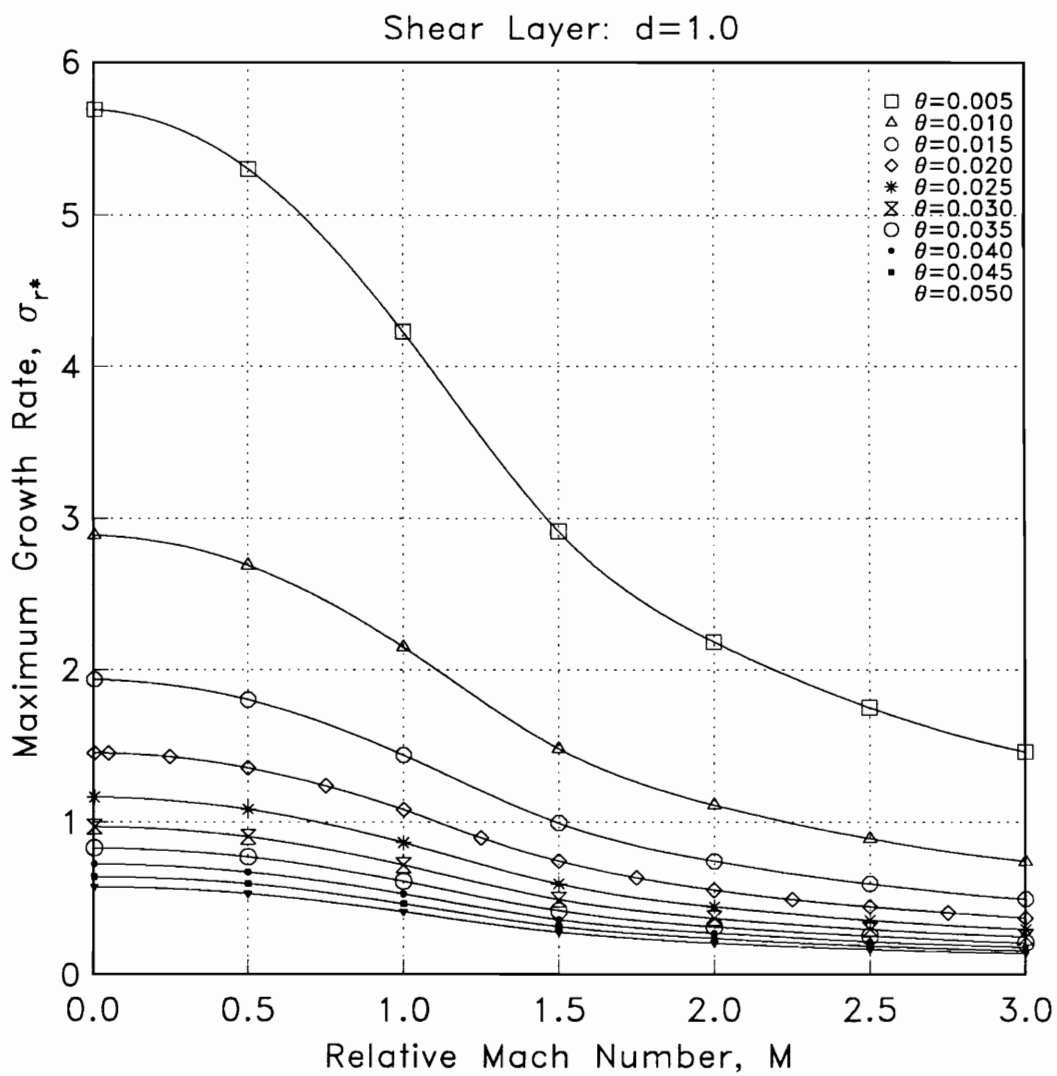


Figure 3.19 Shear layer maximum growth rate vs. relative Mach number

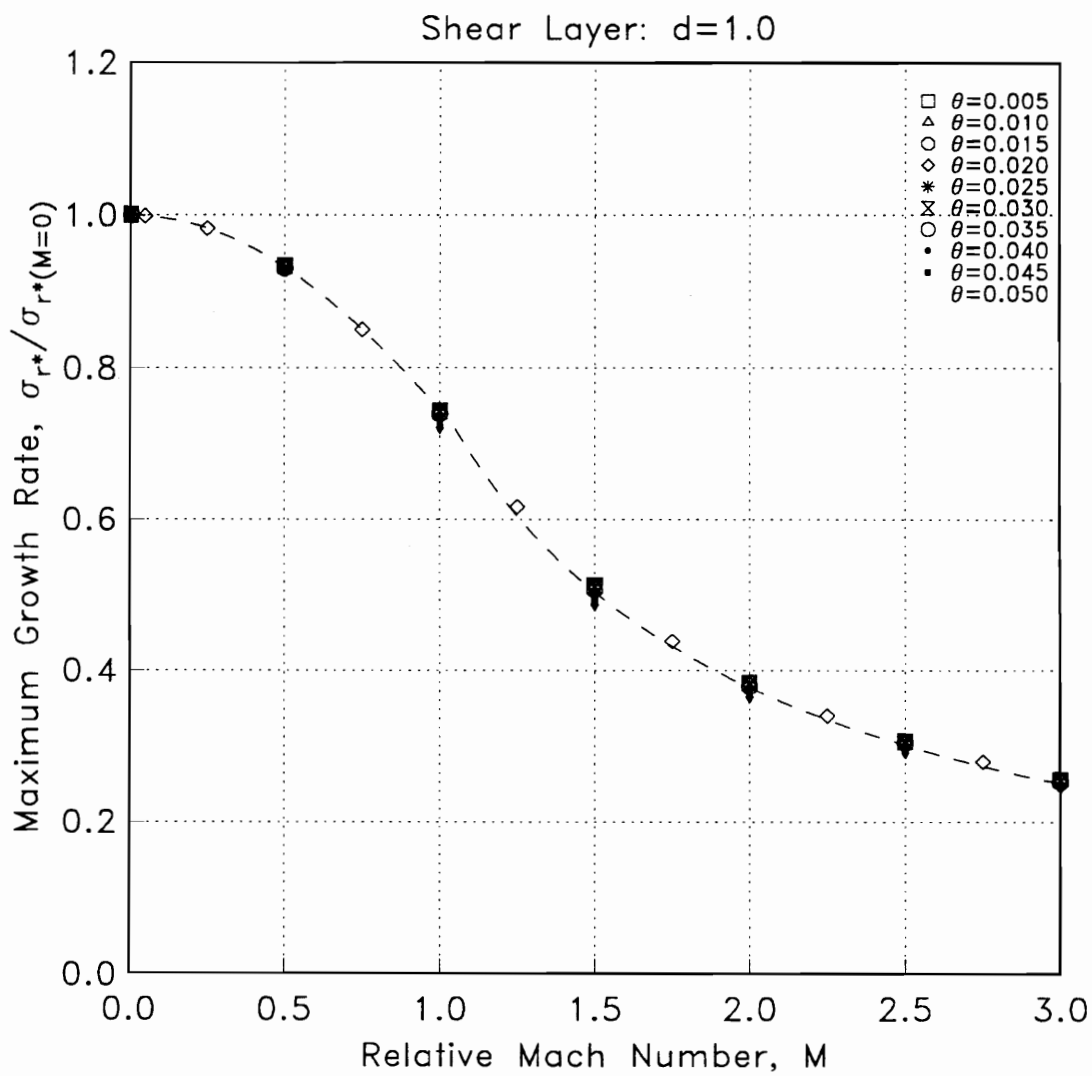


Figure 3.20 Shear layer maximum growth rate (collapsed) vs. relative Mach number

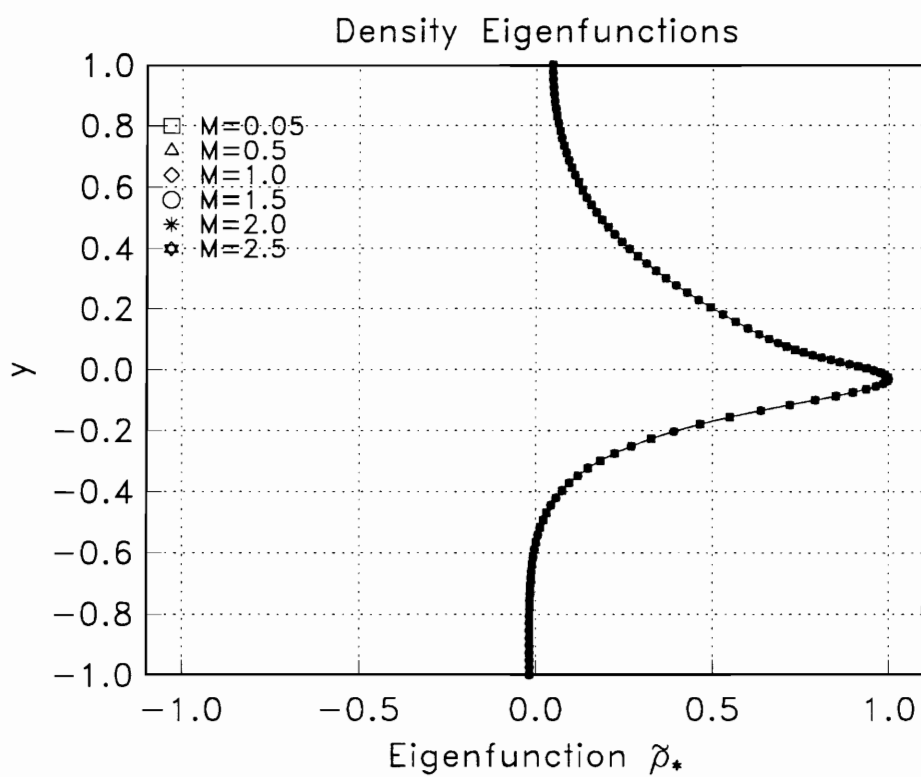


Figure 3.21 Shear layer density eigenfunctions vs. relative Mach number

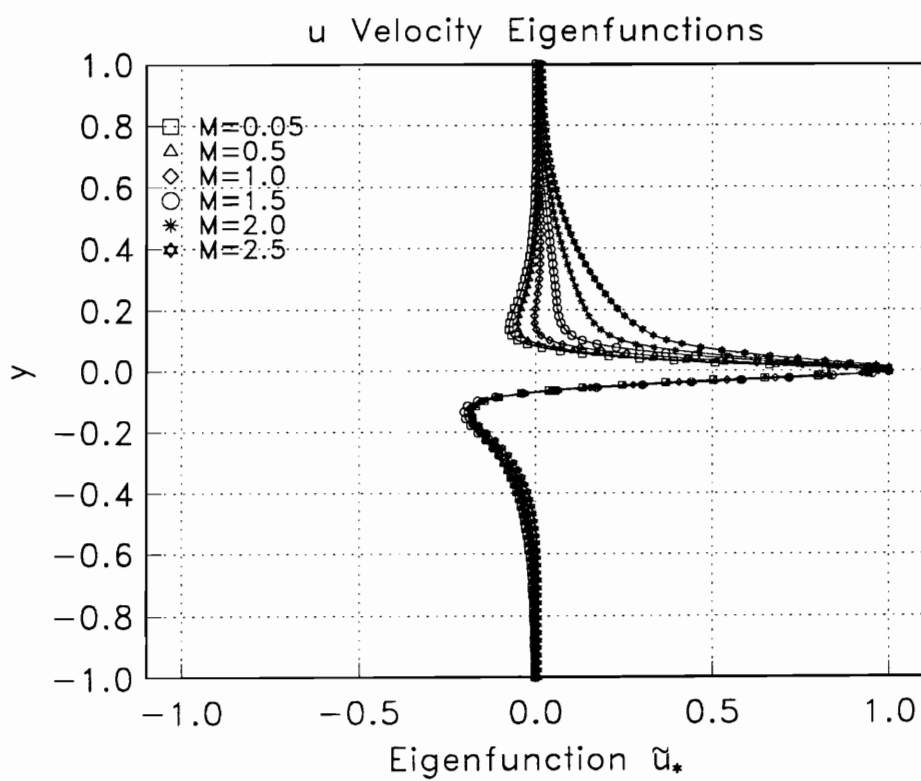


Figure 3.22 Shear layer u velocity eigenfunctions vs. relative Mach number

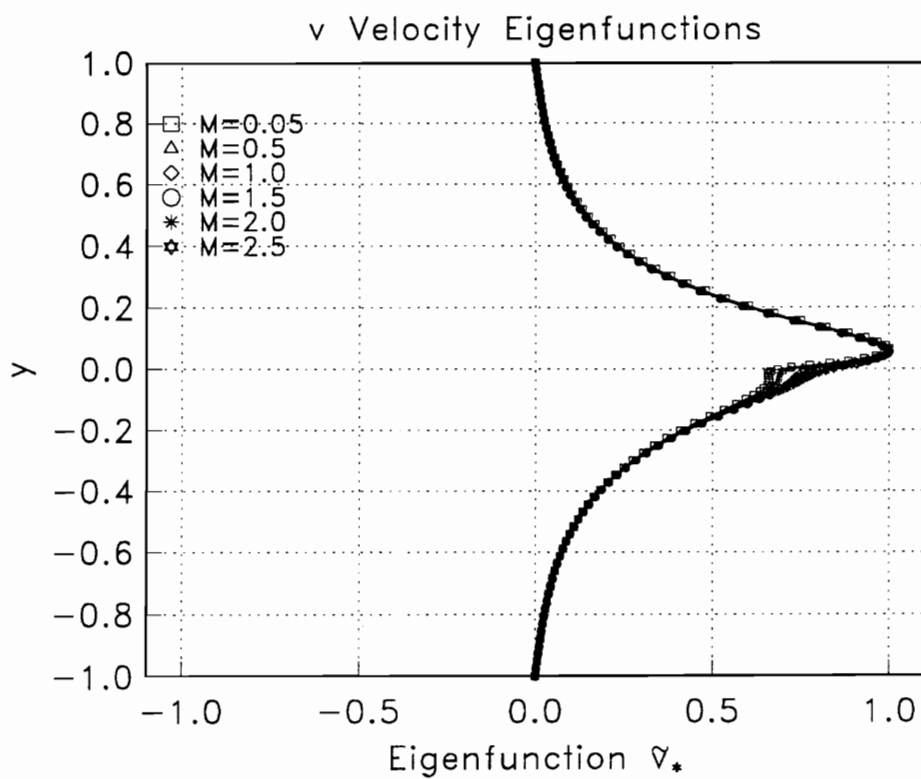


Figure 3.23 Shear layer v velocity eigenfunctions vs. relative Mach number

CONTOUR LEVELS

0.00000
0.10000
0.20000
0.30000
0.40000
0.50000
0.60000
0.70000
0.80000
0.90000
1.00000

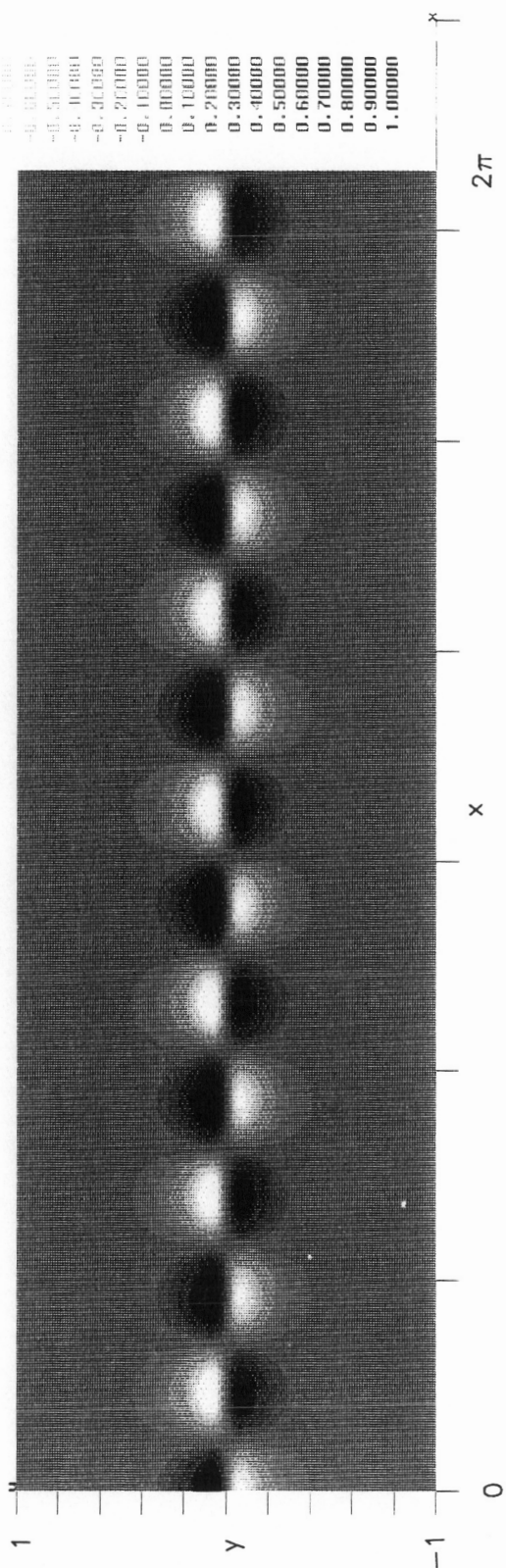


Figure 3.24 Shear layer density disturbance $p'(x,y,z=0,t=0)$; $M=0.5$, $\theta=0.02$, $k=6.75$

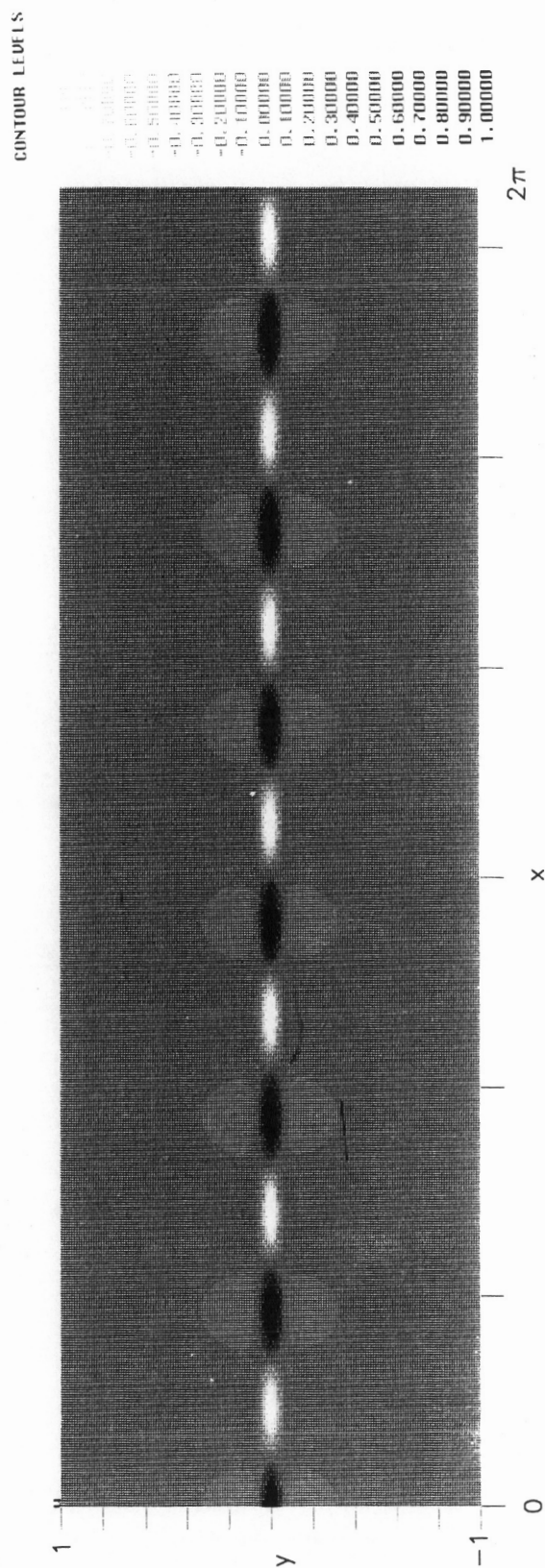
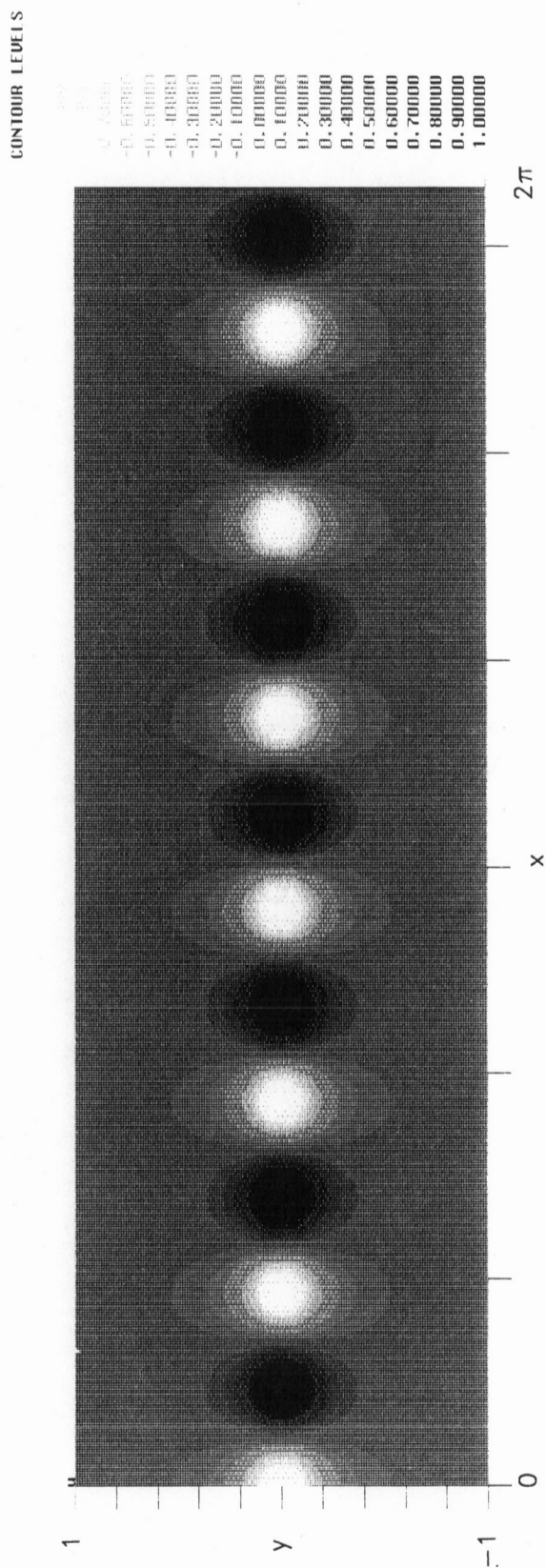


Figure 3.25 Shear layer velocity disturbance $u'(x, y, z=0, t=0)$; $M=0.5$, $\theta=0.02$, $k=6.75$



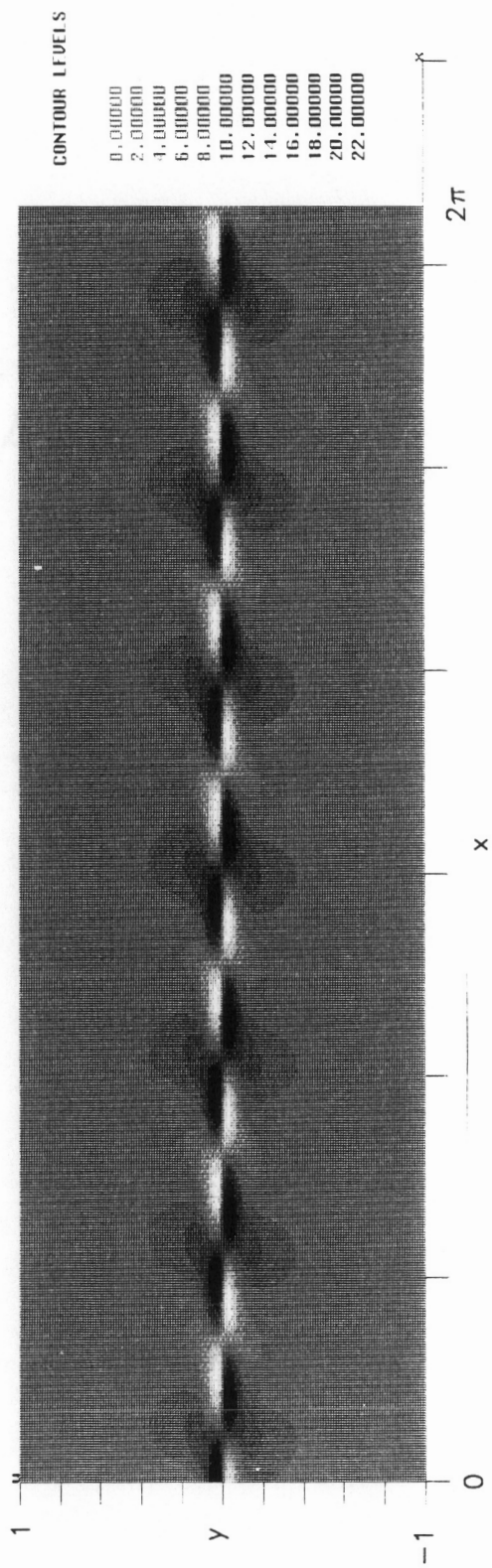


Figure 3.27 Shear layer vorticity disturbance $\Omega'_z(x, y, z=0, t=0)$; $M=0.5$, $\theta=0.02$, $k=6.75$

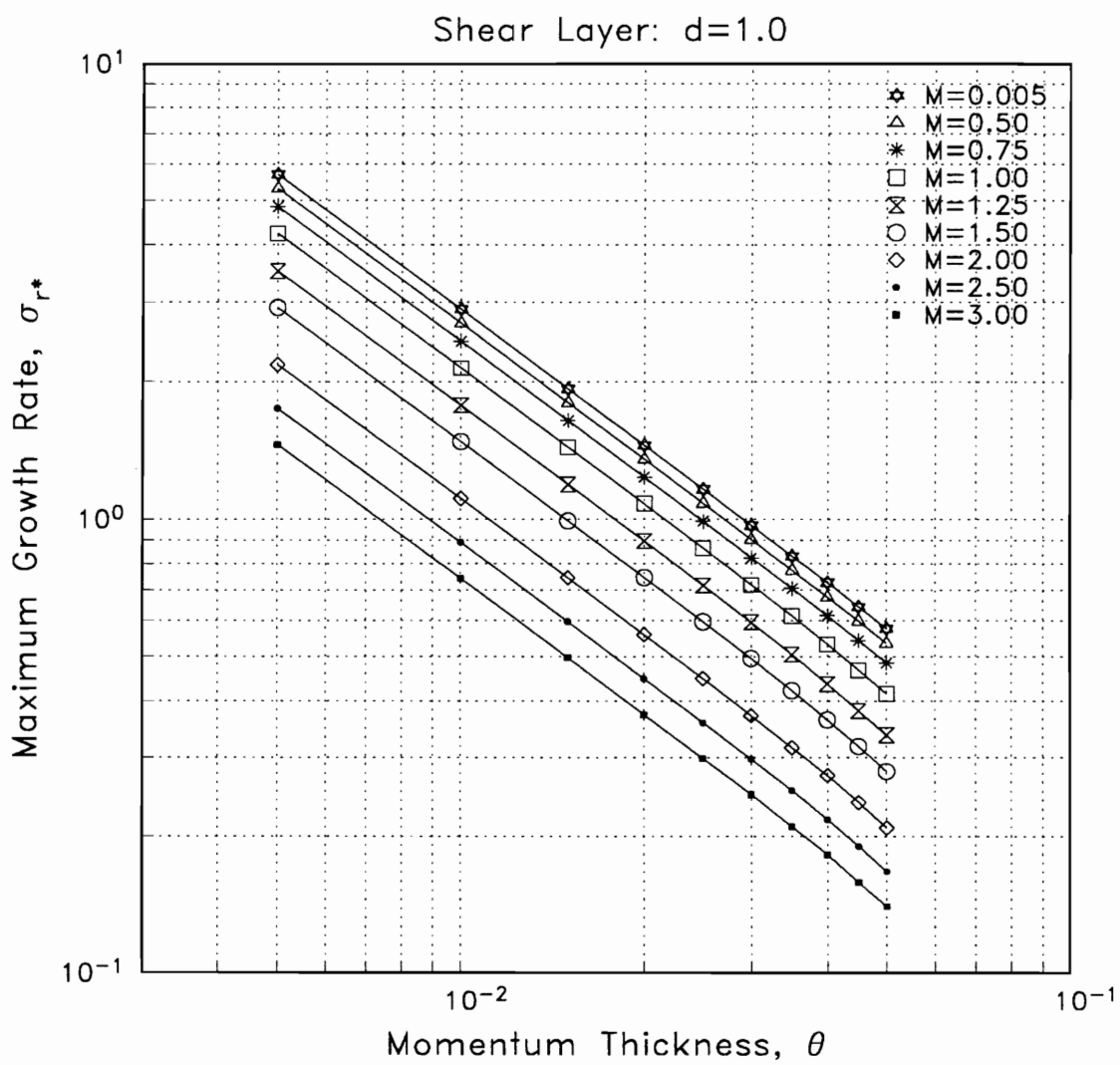


Figure 3.28 Shear layer maximum growth rate vs. momentum thickness

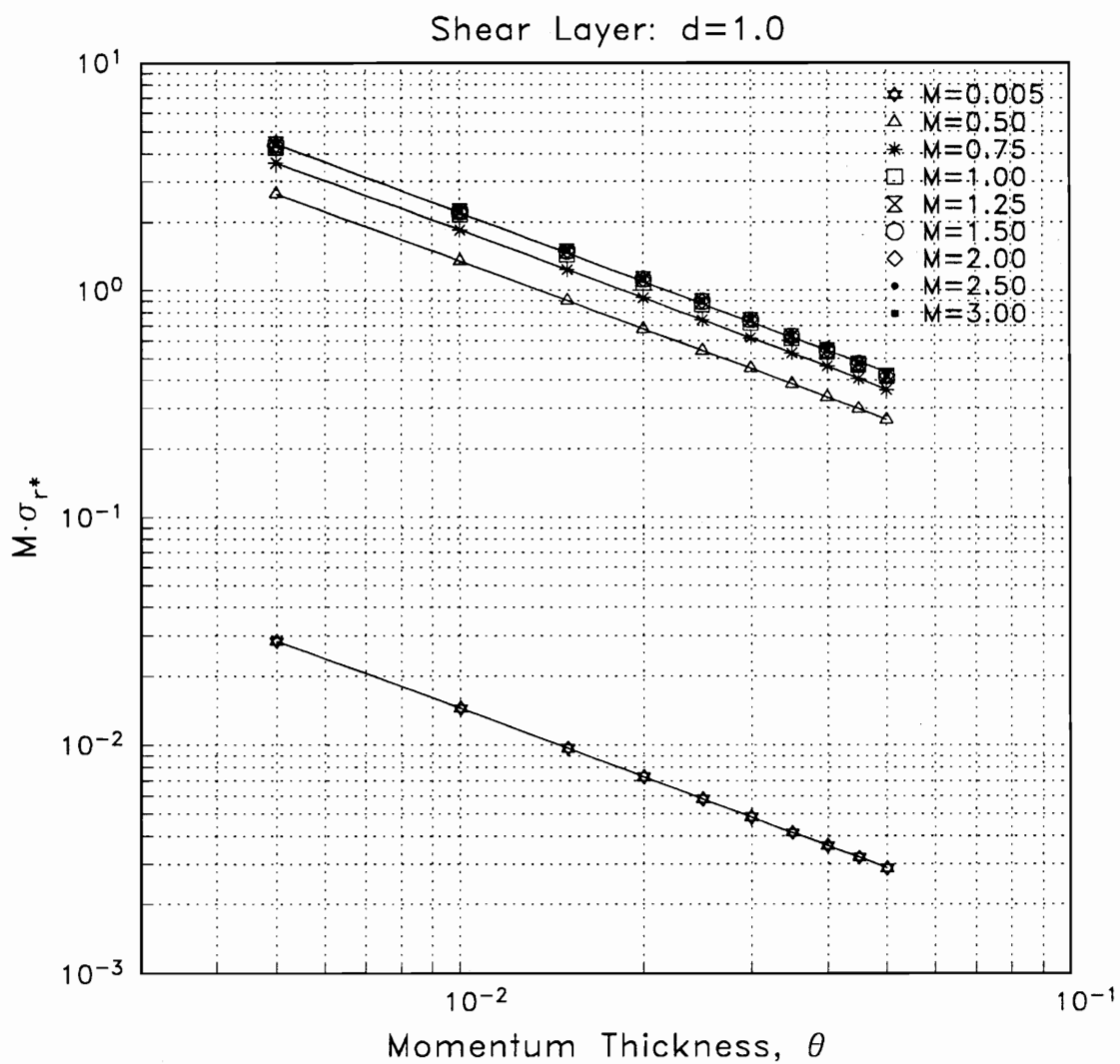


Figure 3.29 Shear layer maximum dimensional growth rate vs. momentum thickness

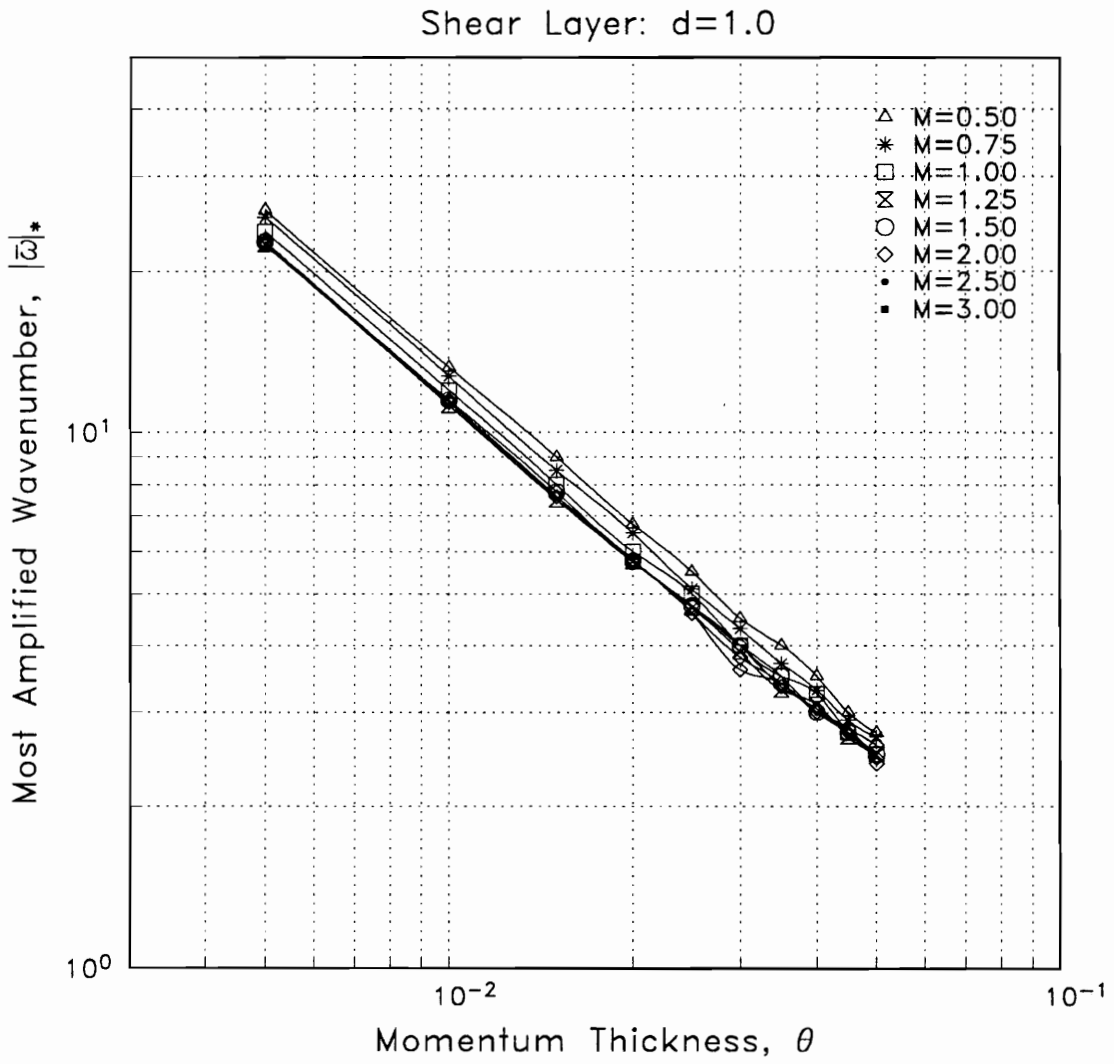


Figure 3.30 Shear layer most amplified wavenumber vs. momentum thickness

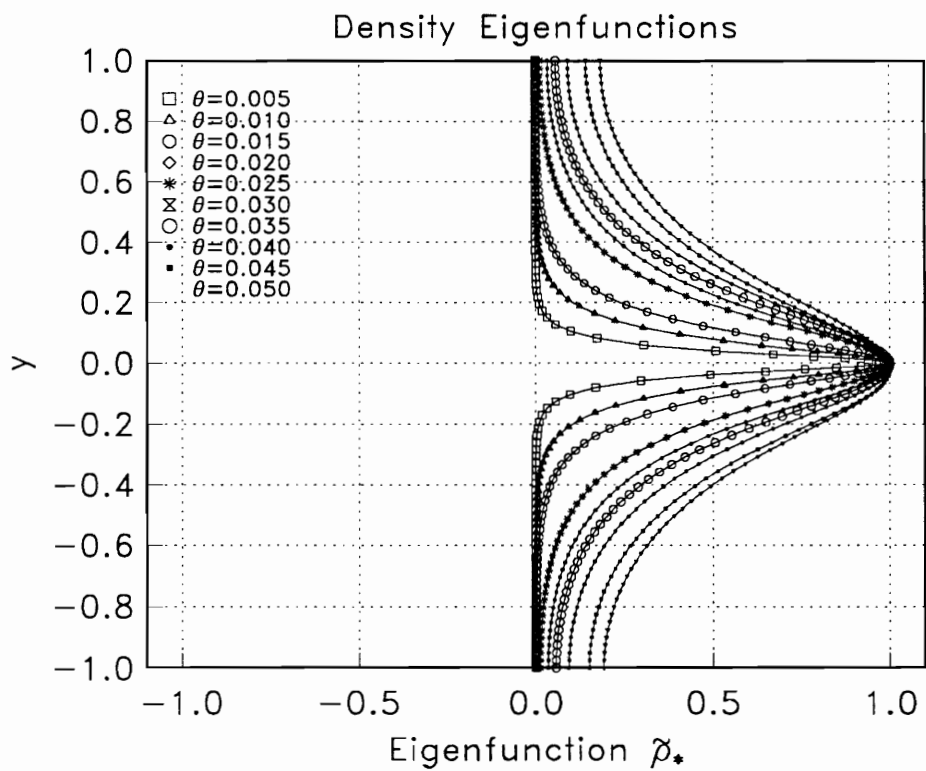


Figure 3.31 Shear layer density eigenfunctions vs. momentum thickness

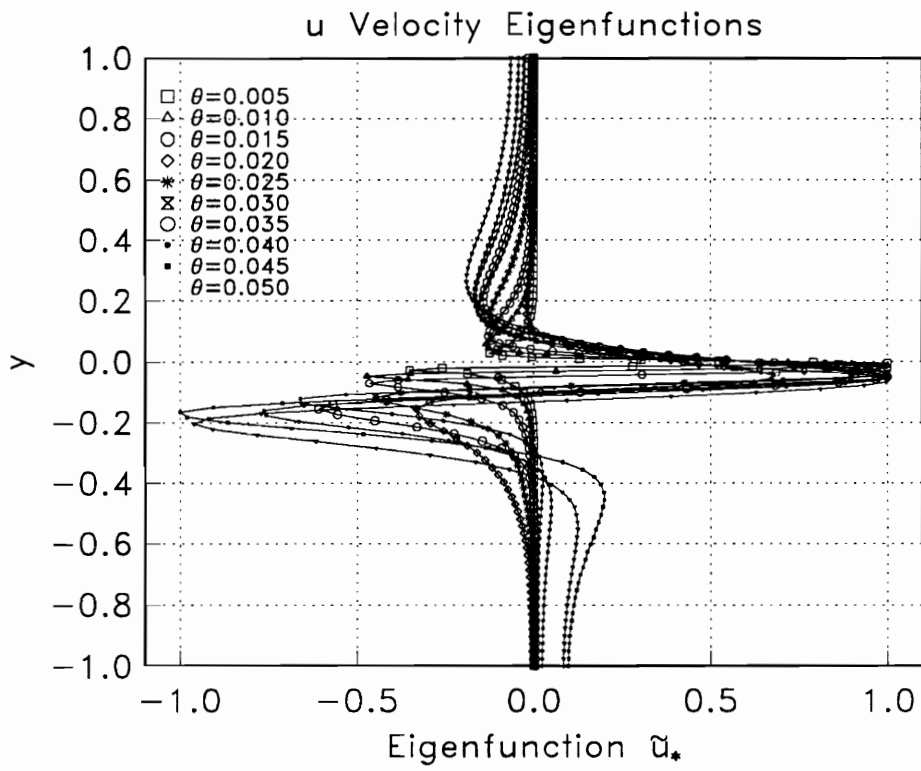


Figure 3.32 Shear layer u velocity eigenfunctions vs. momentum thickness

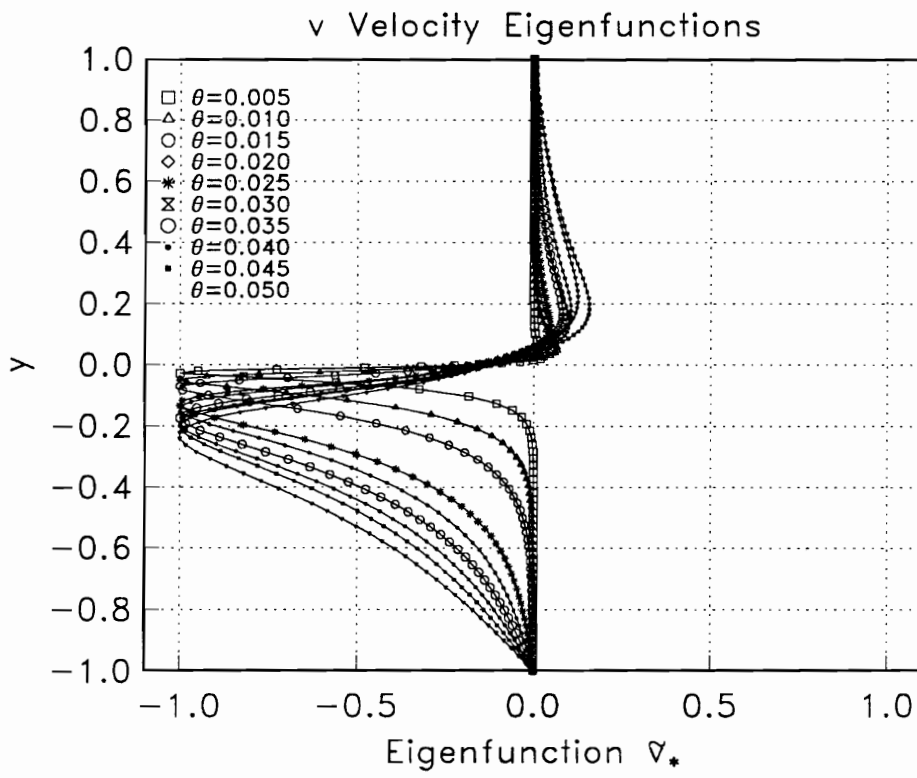


Figure 3.33 Shear layer v velocity eigenfunctions vs. momentum thickness

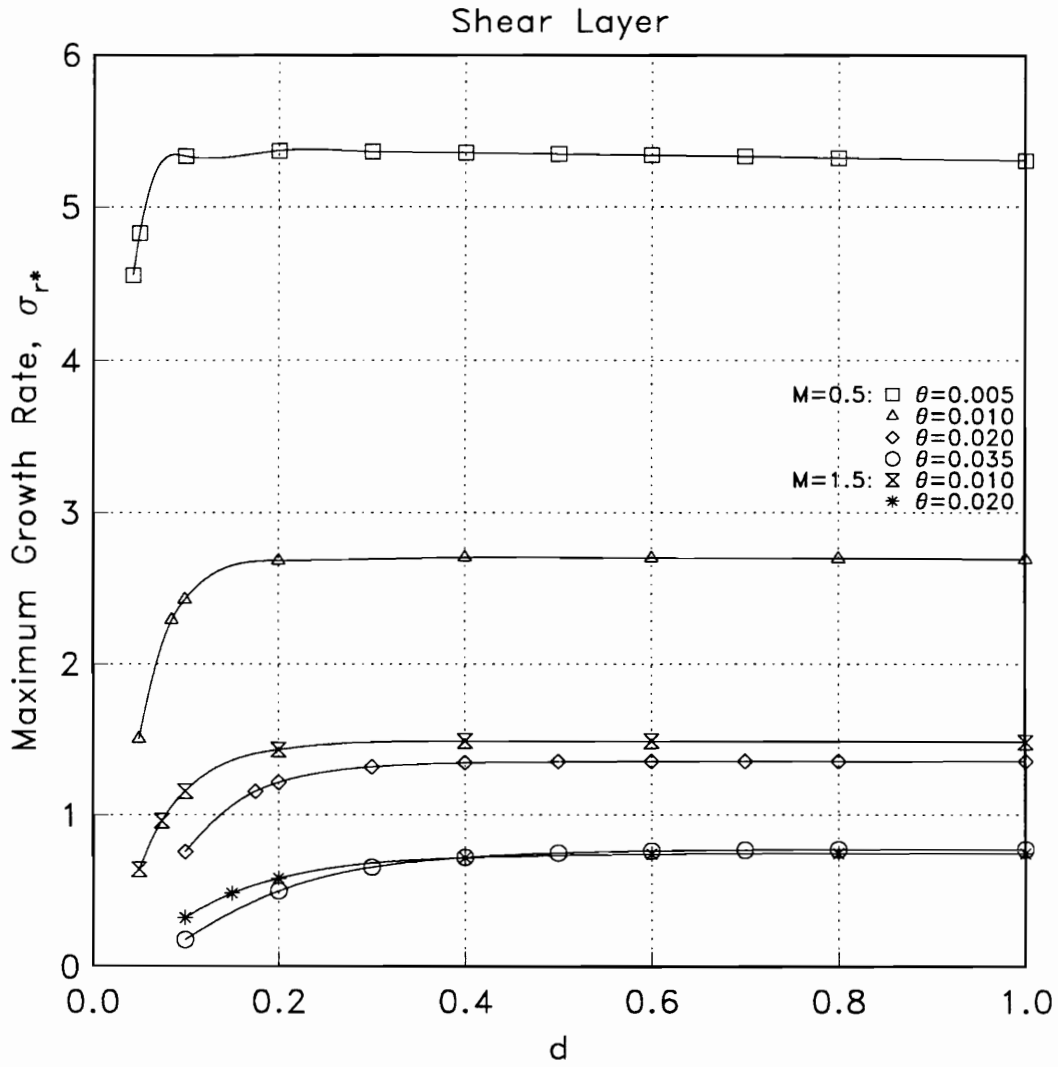


Figure 3.34 Shear layer maximum growth rate vs. wall placement

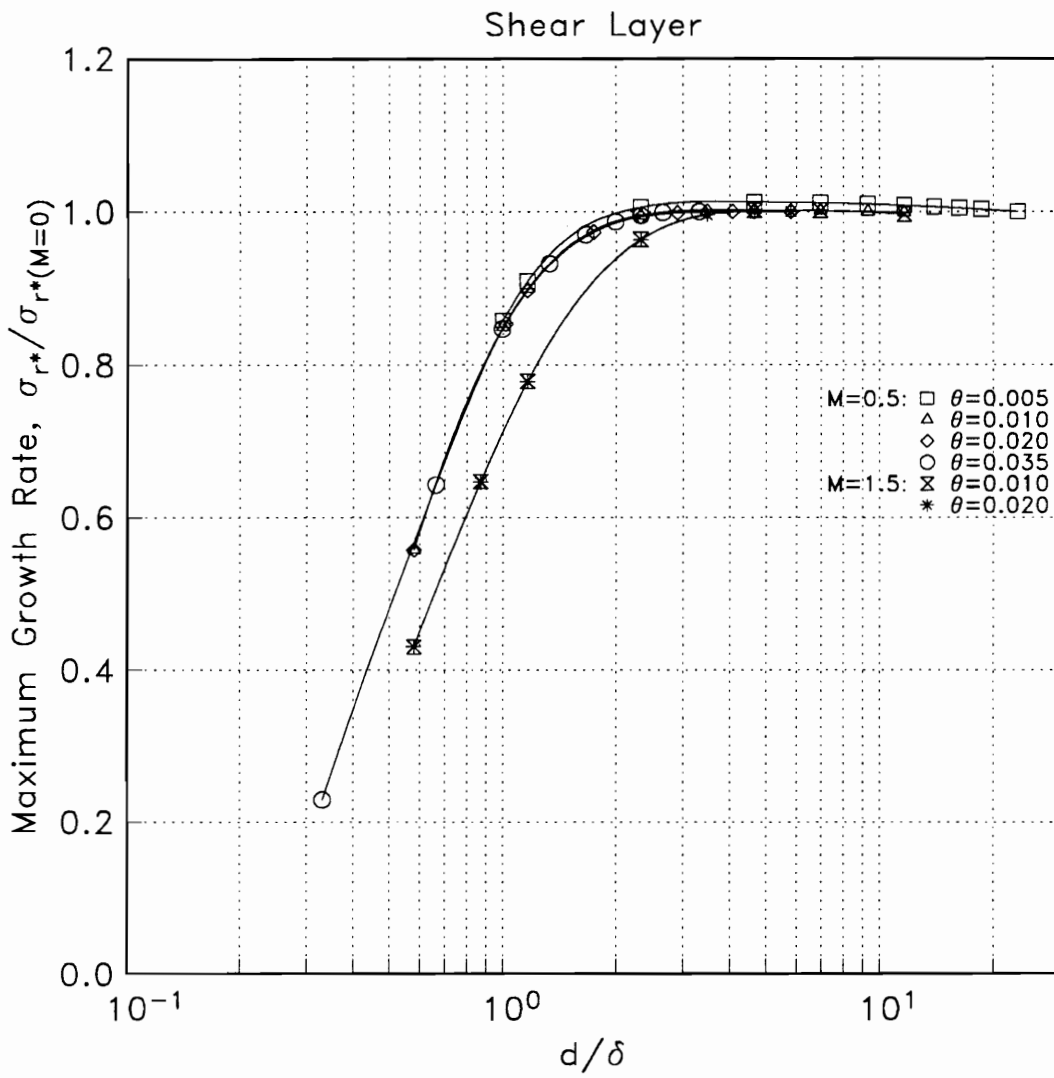


Figure 3.35 Shear layer maximum growth rate (collapsed) vs. wall spacing

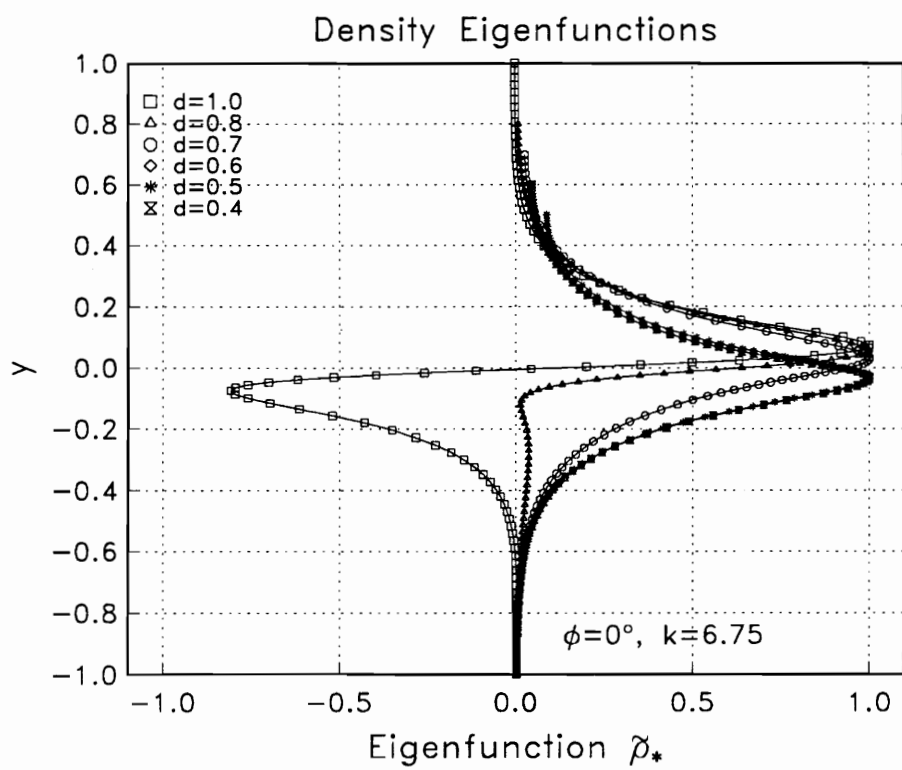


Figure 3.36 Shear layer density eigenfunctions vs. wall spacing

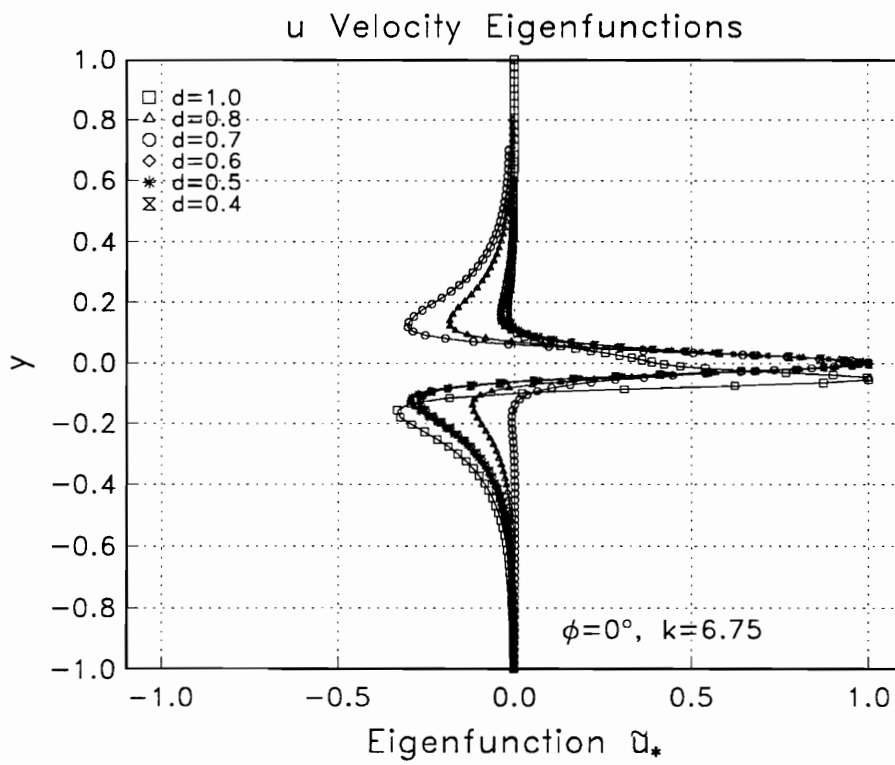


Figure 3.37 Shear layer u velocity eigenfunctions vs. wall spacing

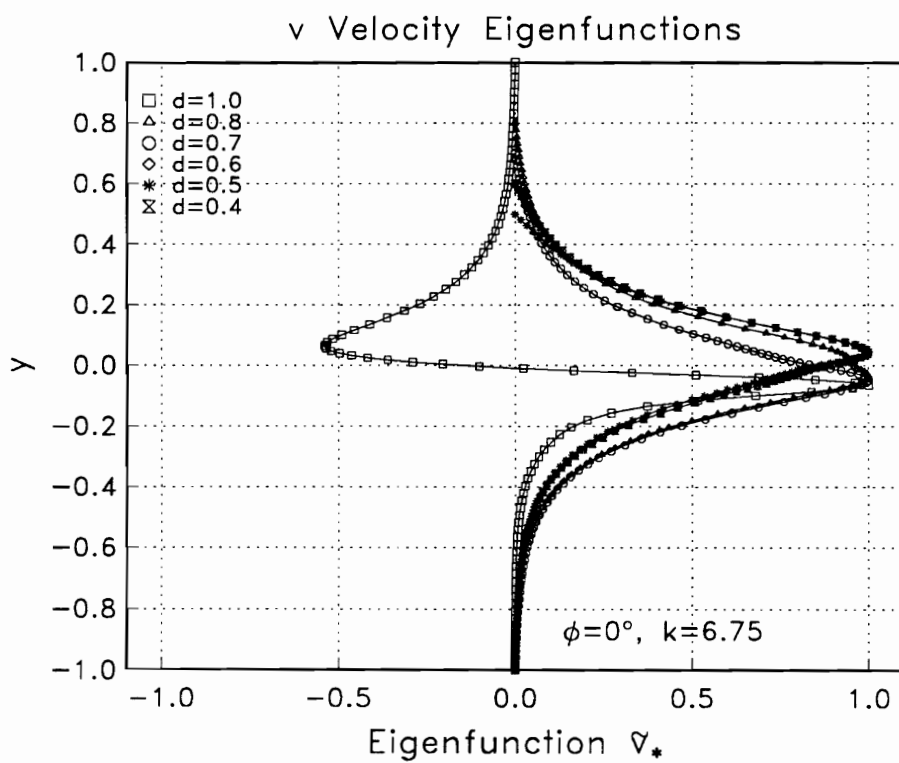


Figure 3.38 Shear layer v velocity eigenfunctions vs. wall spacing

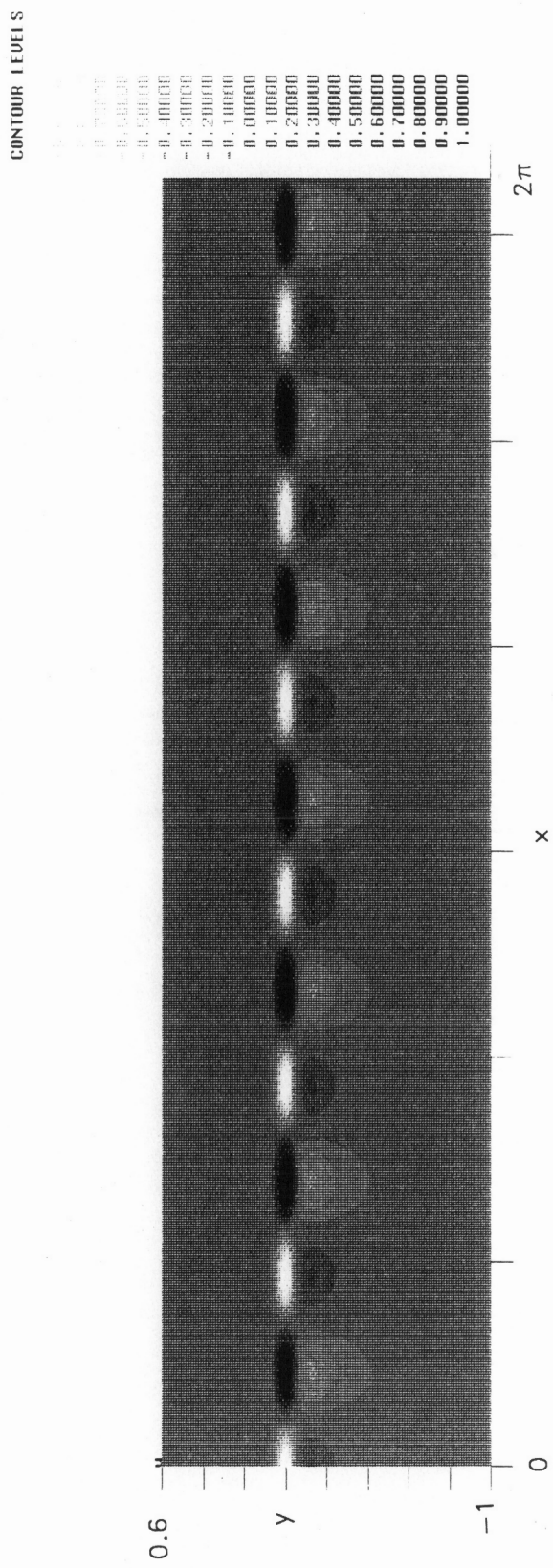


Figure 3.40 Shear layer u velocity eigenfunction $u'(x, y, z=0, t=0)$; $M=0.5$, $\theta=0.02$, $d=0.6$, $k=6.75$

CONTOUR LEVELS

0.00000
0.10000
0.20000
0.30000
0.40000
0.50000
0.60000
0.70000
0.80000
0.90000
1.00000

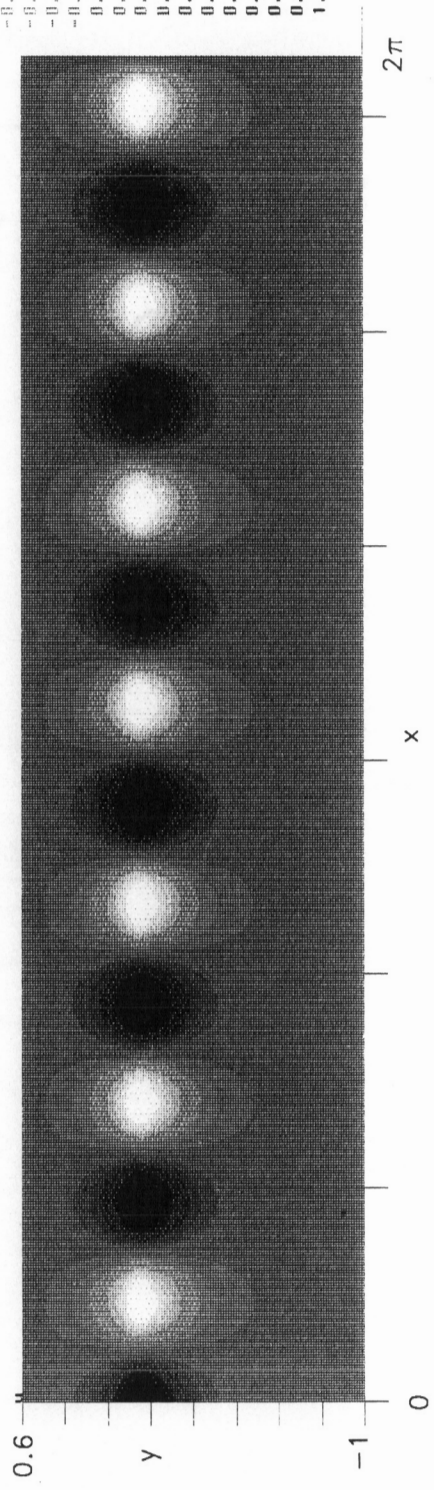


Figure 3.41 Shear layer v velocity eigenfunction $v'(x,y,z=0,t=0)$; $M=0.5$, $\theta=0.02$, $d=0.6$, $k=6.75$

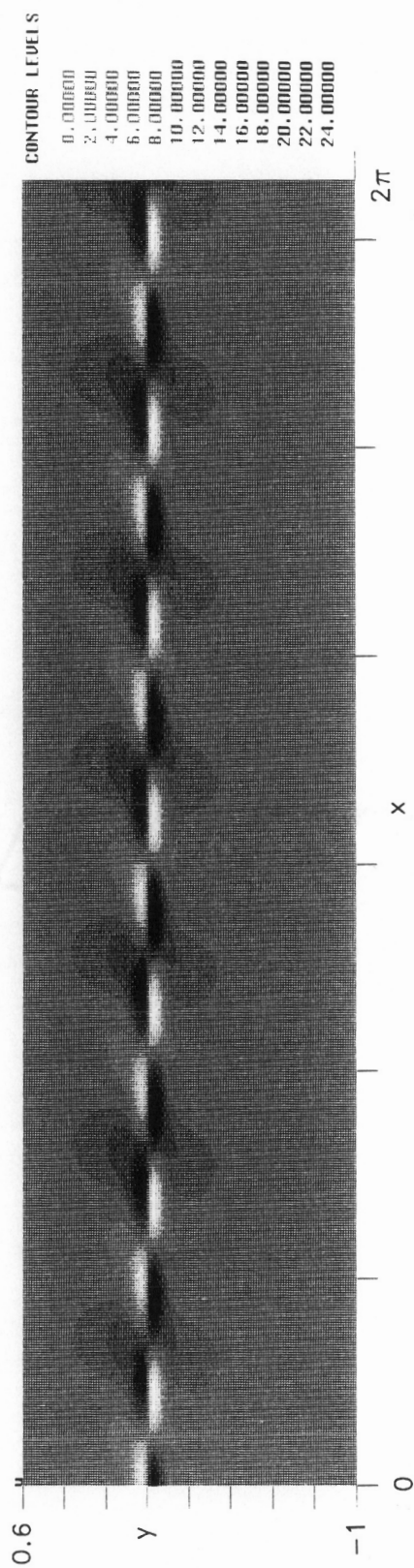


Figure 3.42 Shear layer vorticity eigenfunction $\Omega'_z(x, y, z=0, t=0)$; $M=0.5$, $\theta=0.02$, $d=0.6$, $k=6.75$

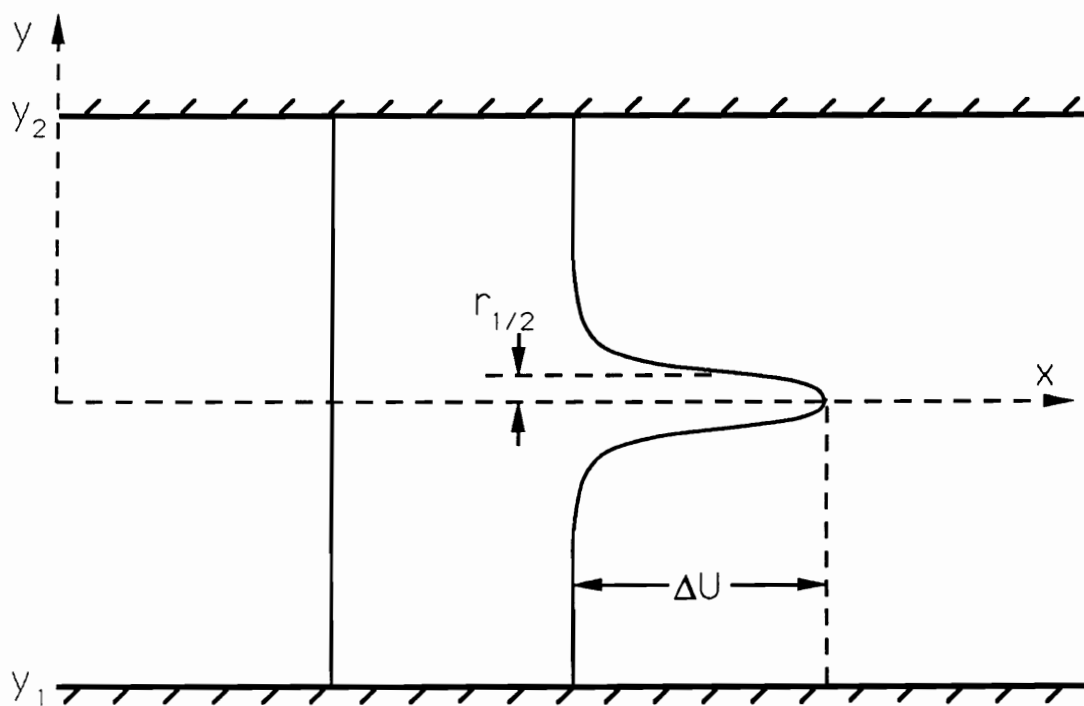


Figure 3.43 Typical planar jet flowfield parameters

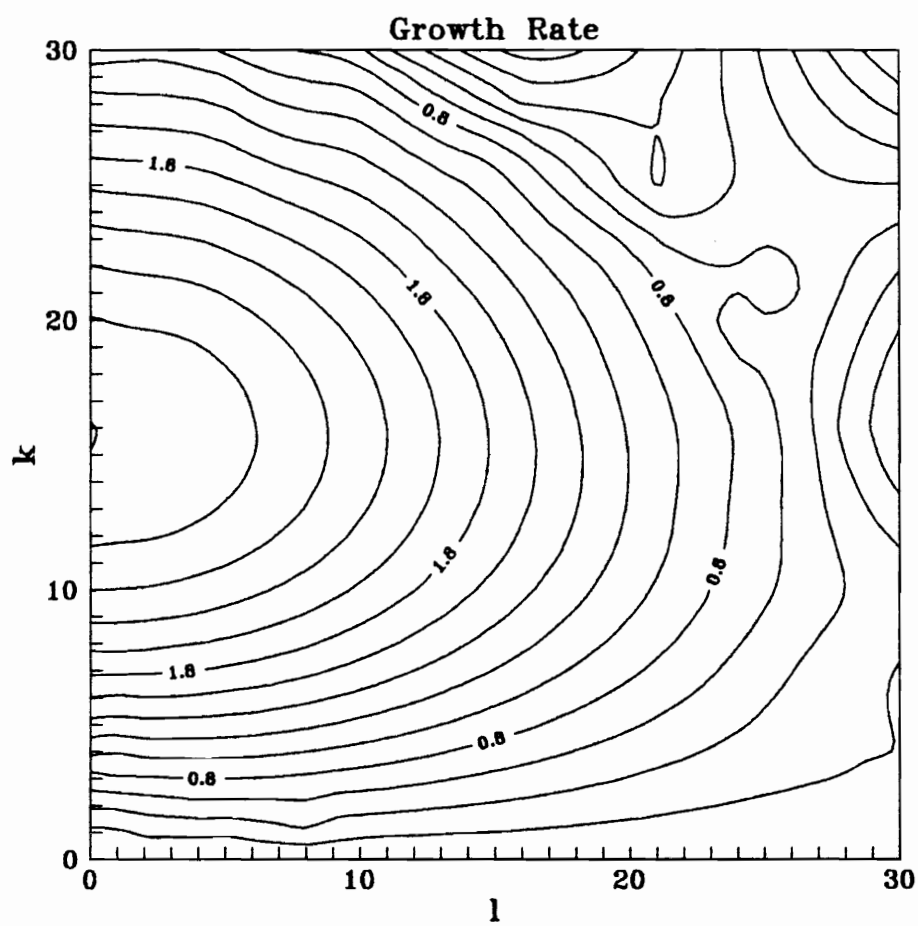


Figure 3.44 Planar jet growth rate surface; $M=0.25$, $r_{1/2}=0.05$

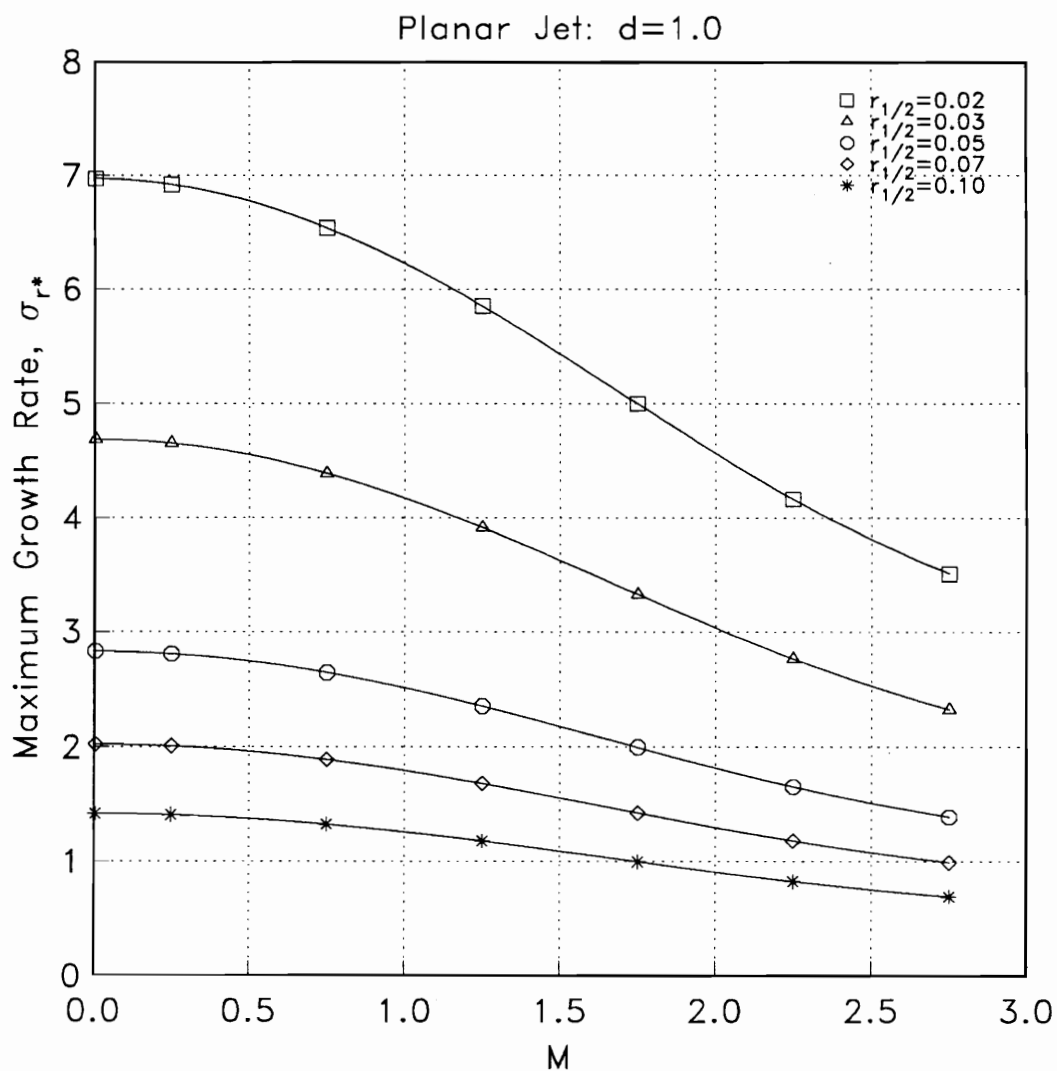


Figure 3.45 Planar jet maximum growth rate vs. relative Mach number

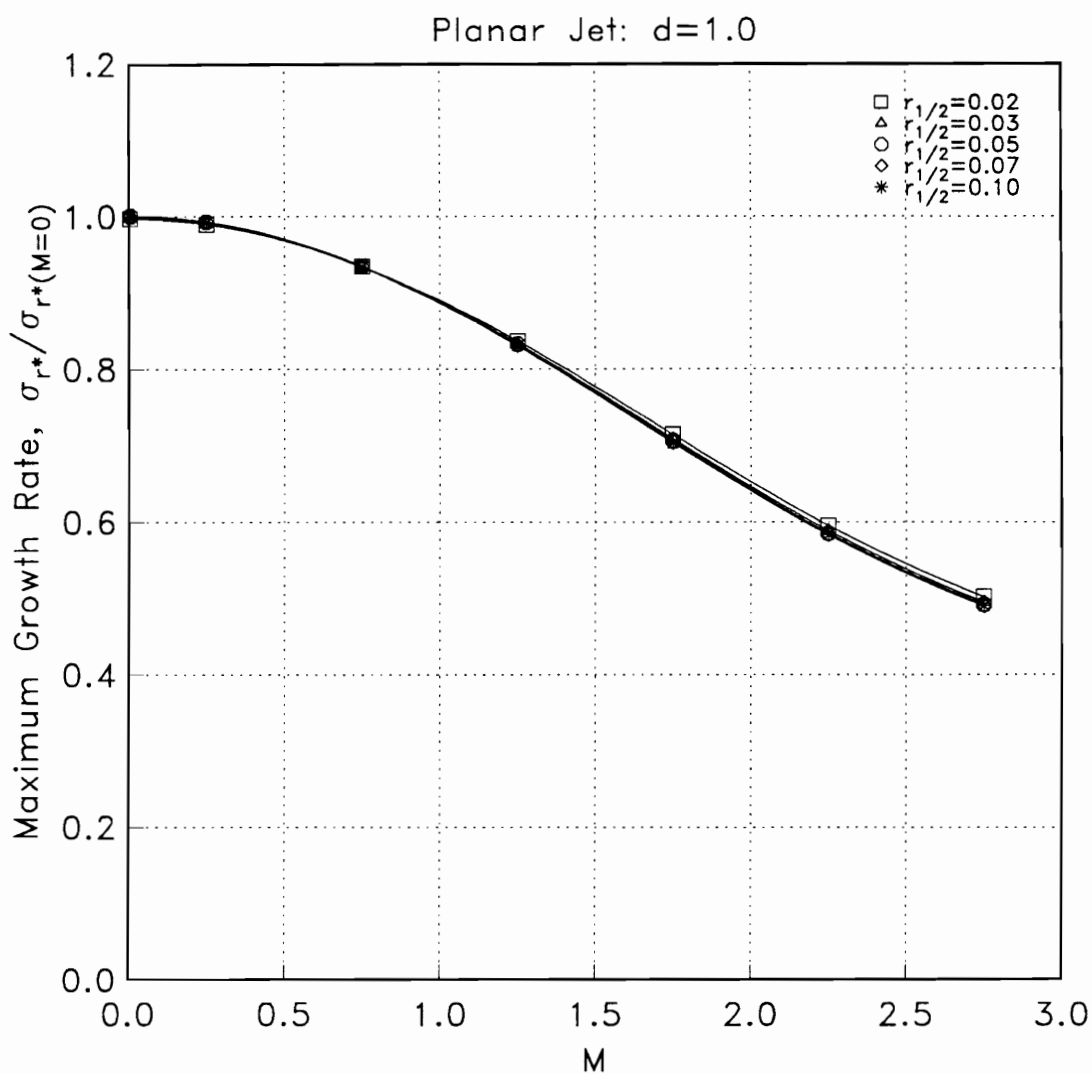


Figure 3.46 Planar jet maximum growth rate (collapsed) vs. relative Mach number

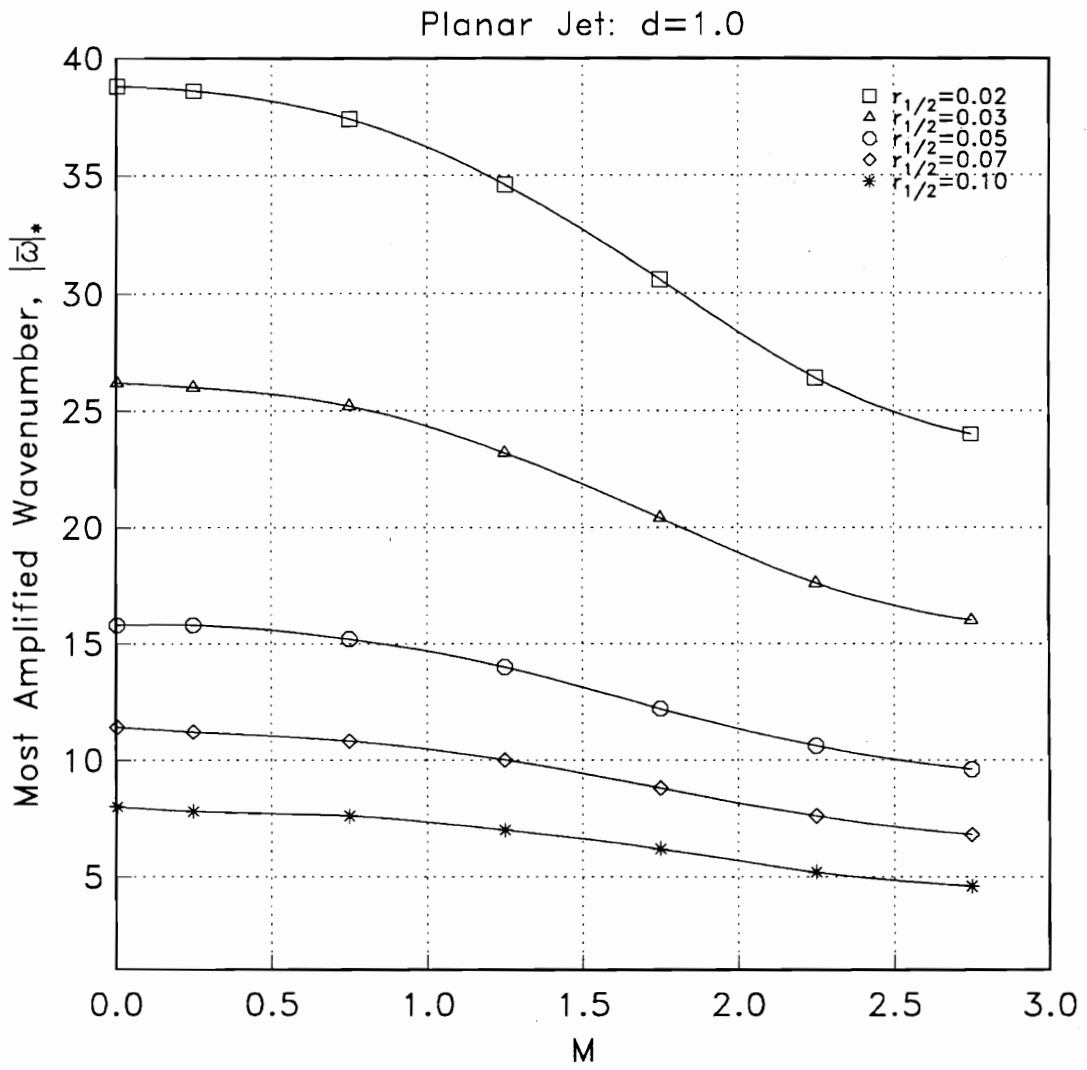


Figure 3.47 Planar jet most amplified wavenumber vs. relative Mach number

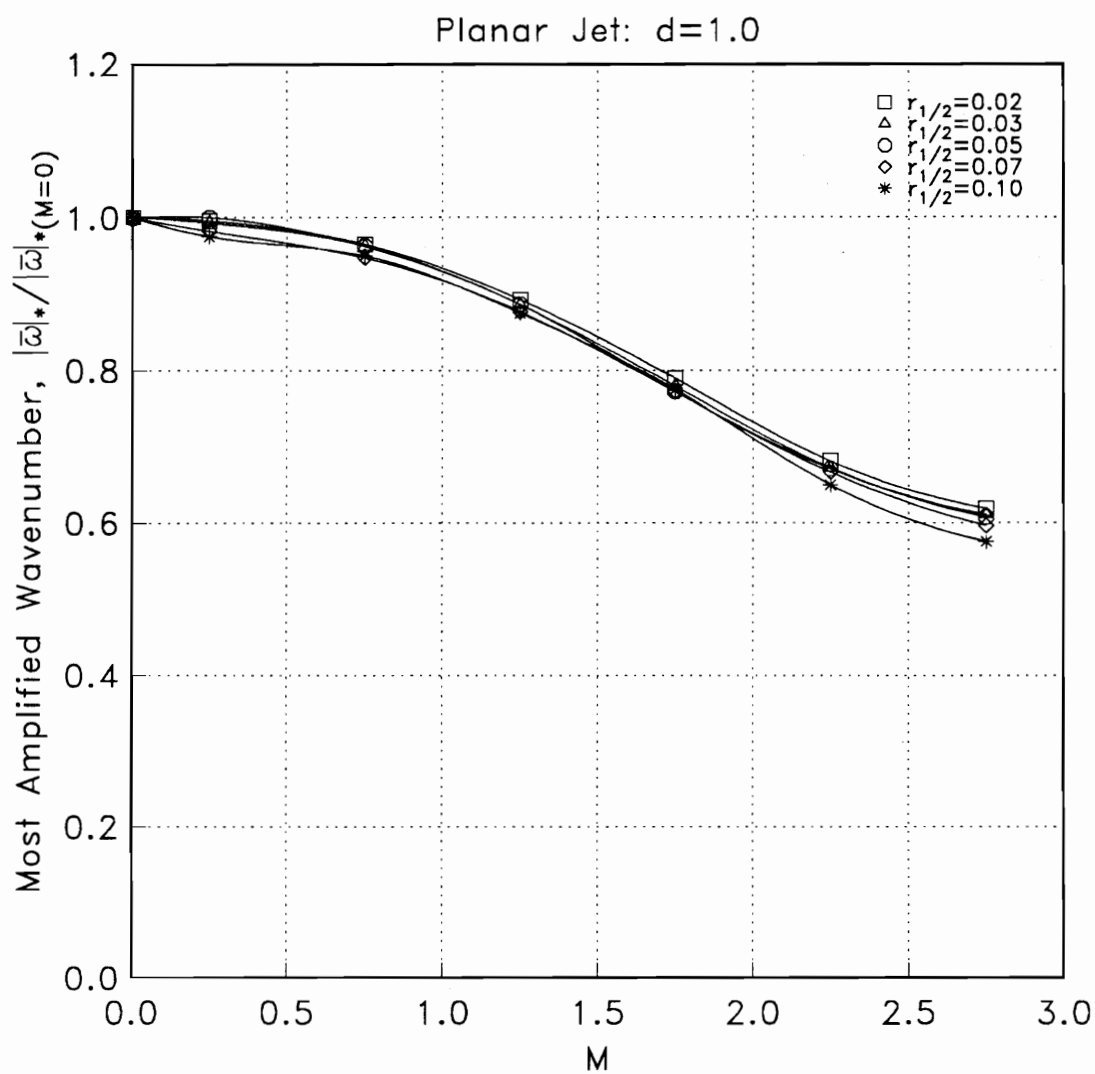


Figure 3.48 Planar jet most amplified wavenumber (collapsed) vs. relative Mach number

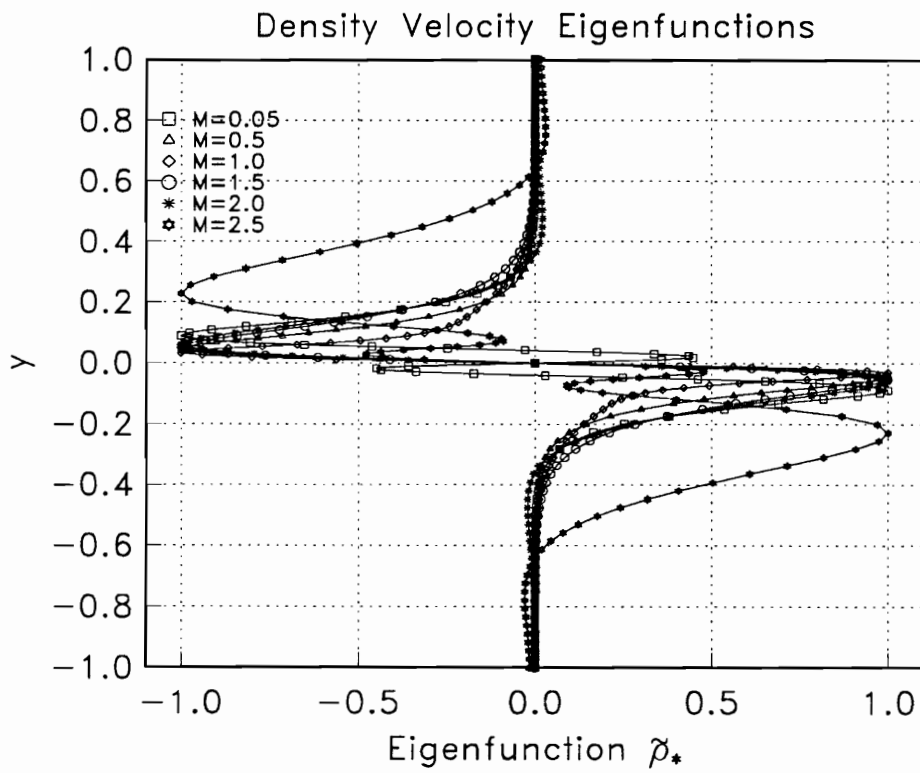


Figure 3.49 Planar jet density eigenfunctions vs. relative Mach number

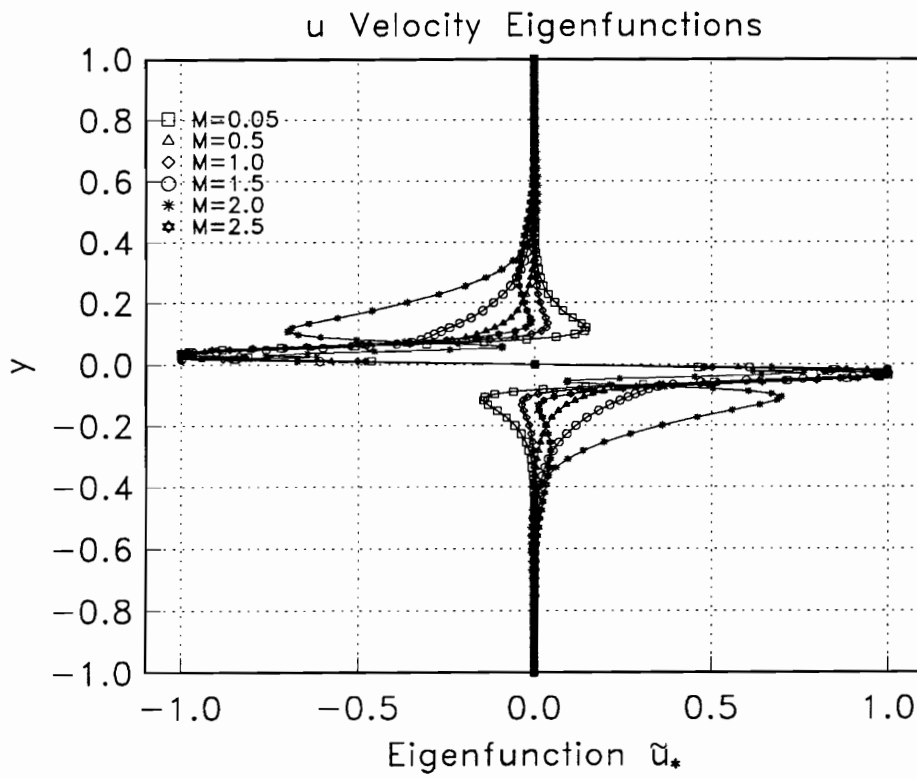


Figure 3.50 Planar jet u velocity eigenfunctions vs. relative Mach number

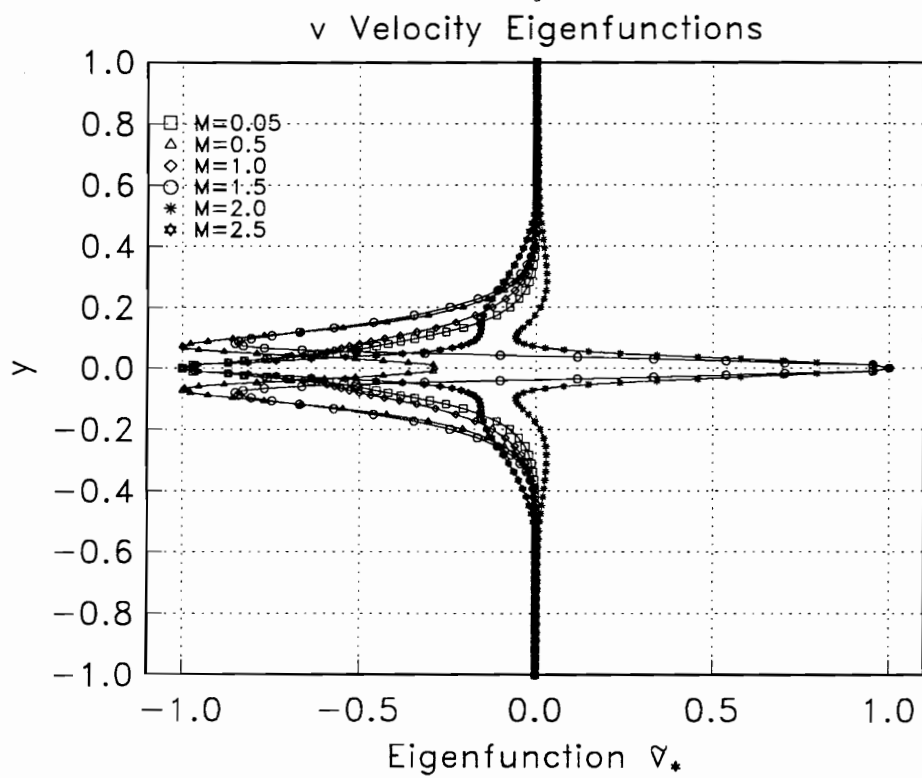


Figure 3.51 Planar jet v velocity eigenfunctions vs. relative Mach number

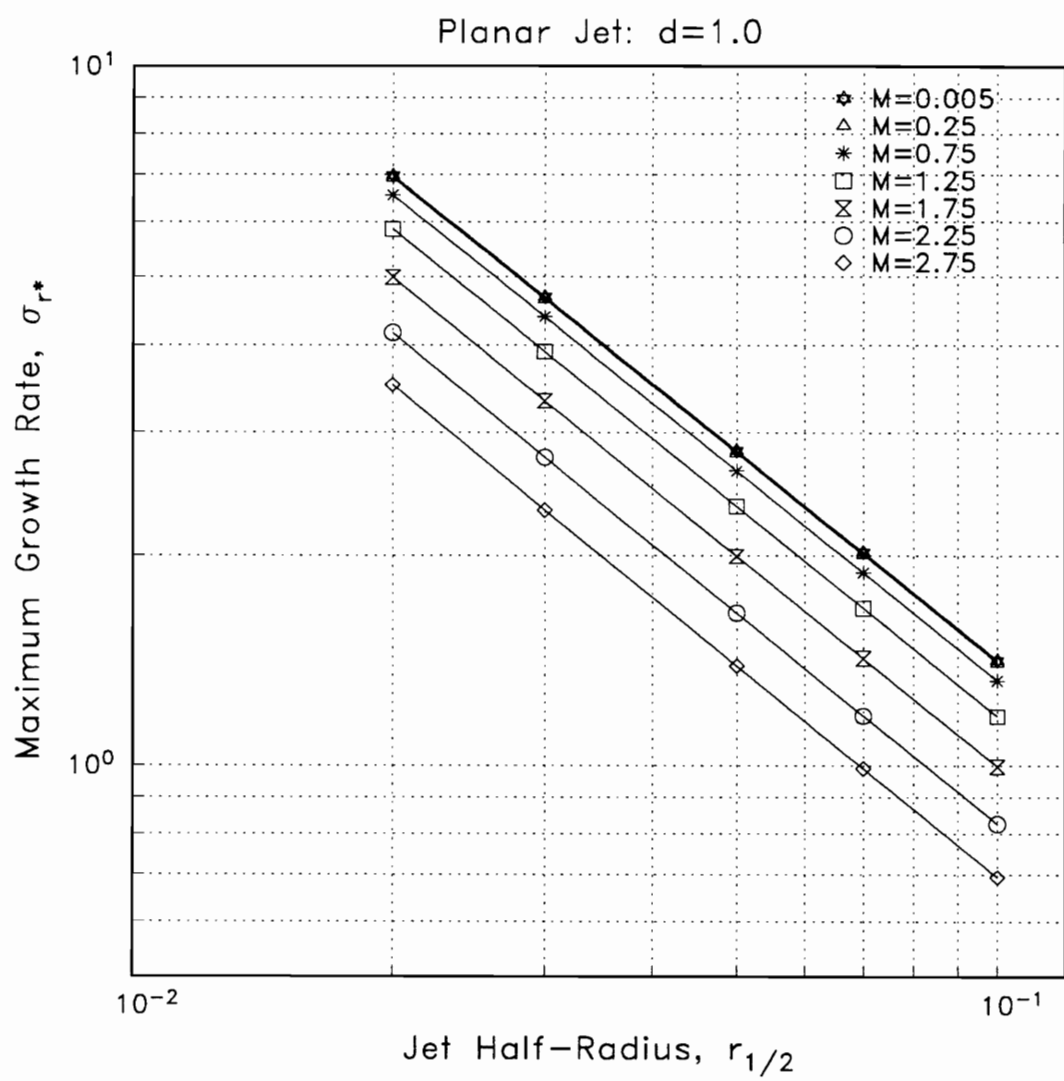


Figure 3.52 Planar jet maximum growth rate vs. jet half-radius

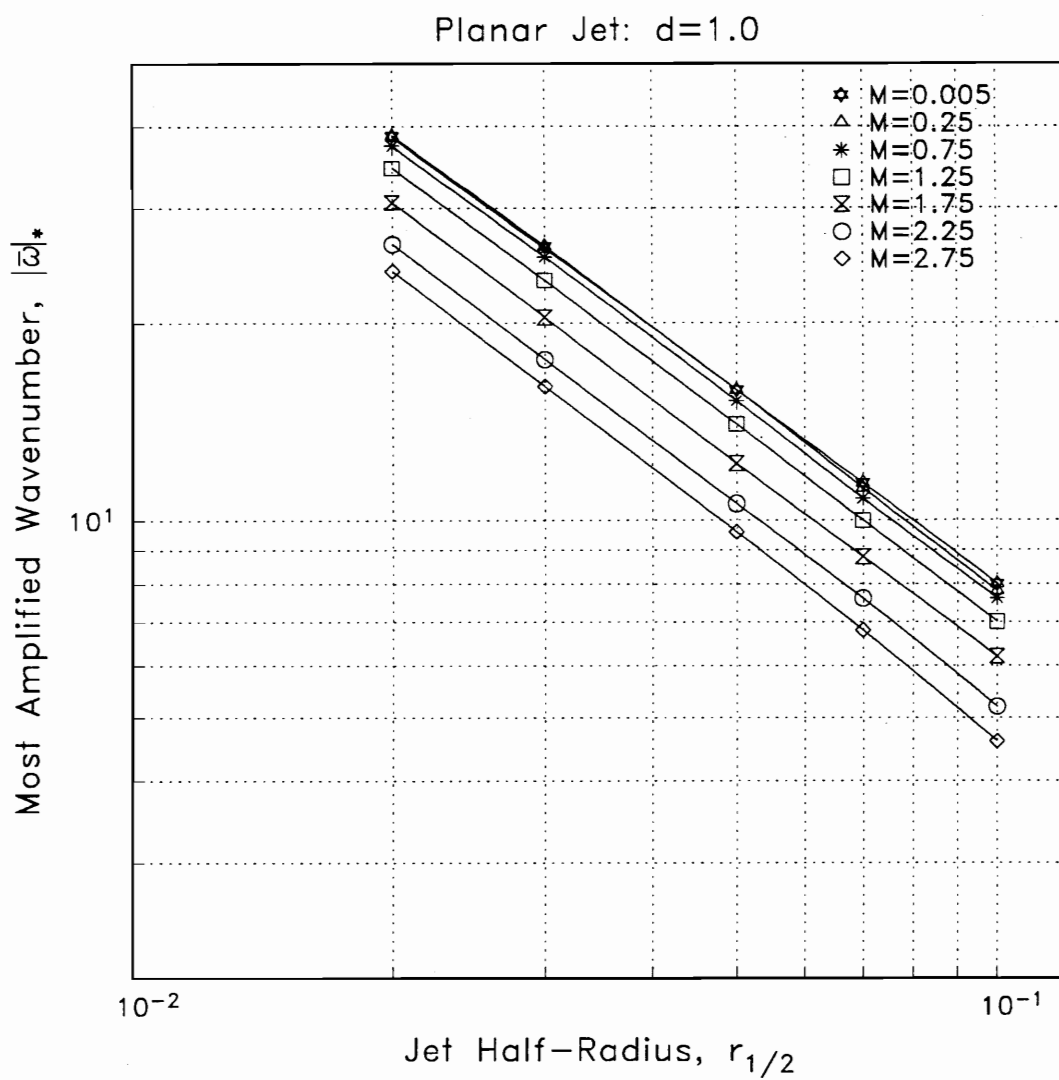


Figure 3.53 Planar jet most amplified wavenumber vs. jet half-radius

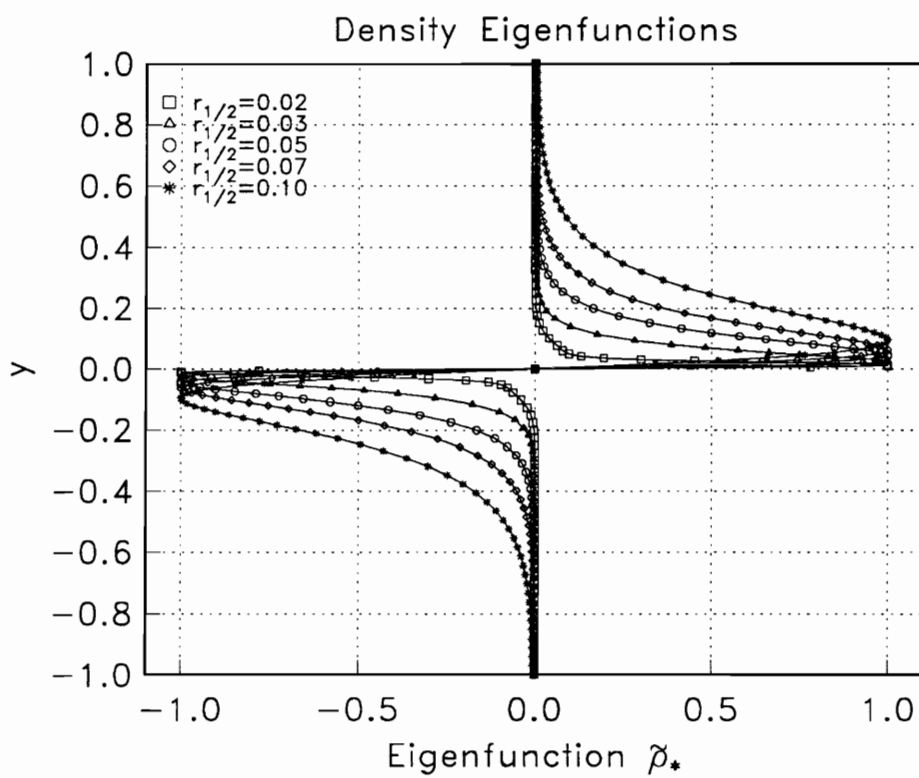


Figure 3.54 Planar jet density eigenfunctions vs. jet half-radius

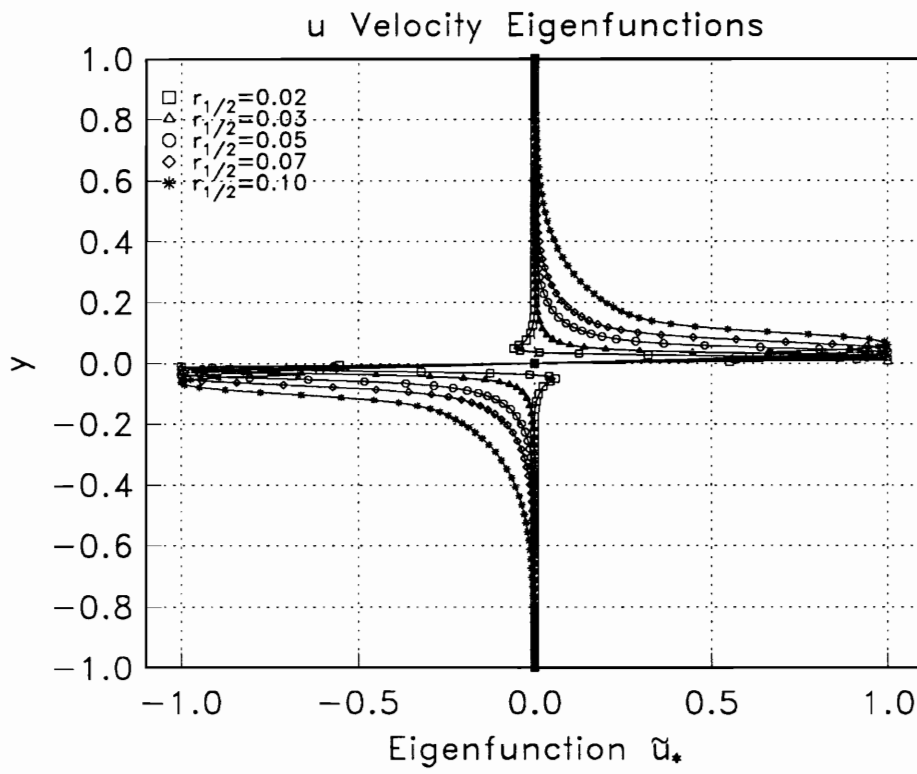


Figure 3.55 Planar jet u velocity eigenfunctions vs. jet half-radius

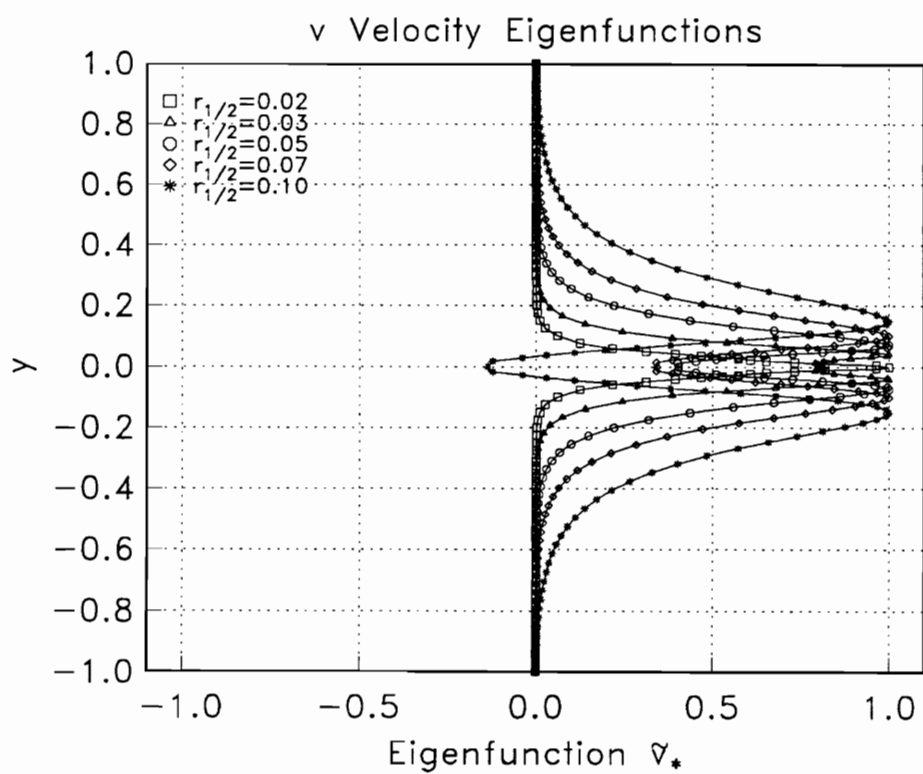


Figure 3.56 Planar jet v velocity eigenfunctions vs. jet half-radius

CONTOUR LEVELS

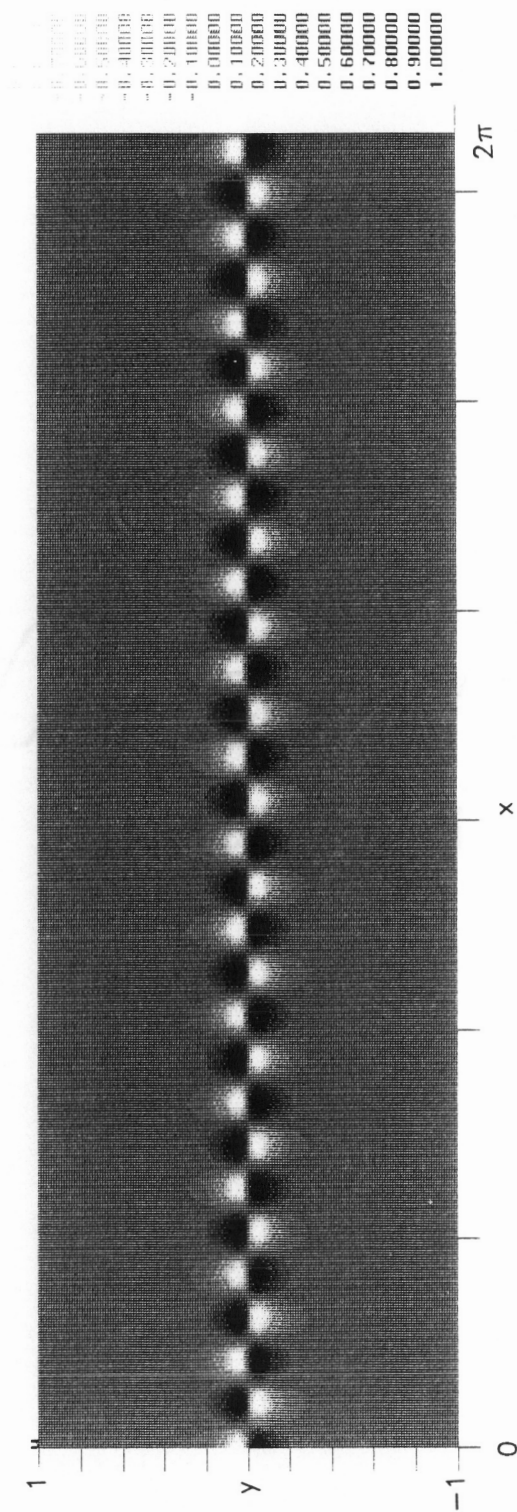


Figure 3.57 Planar jet density disturbance $\rho'(x,y,z=0,t=0)$; $M=0.75$, $r_{1/2}=0.05$, $k=15.2$

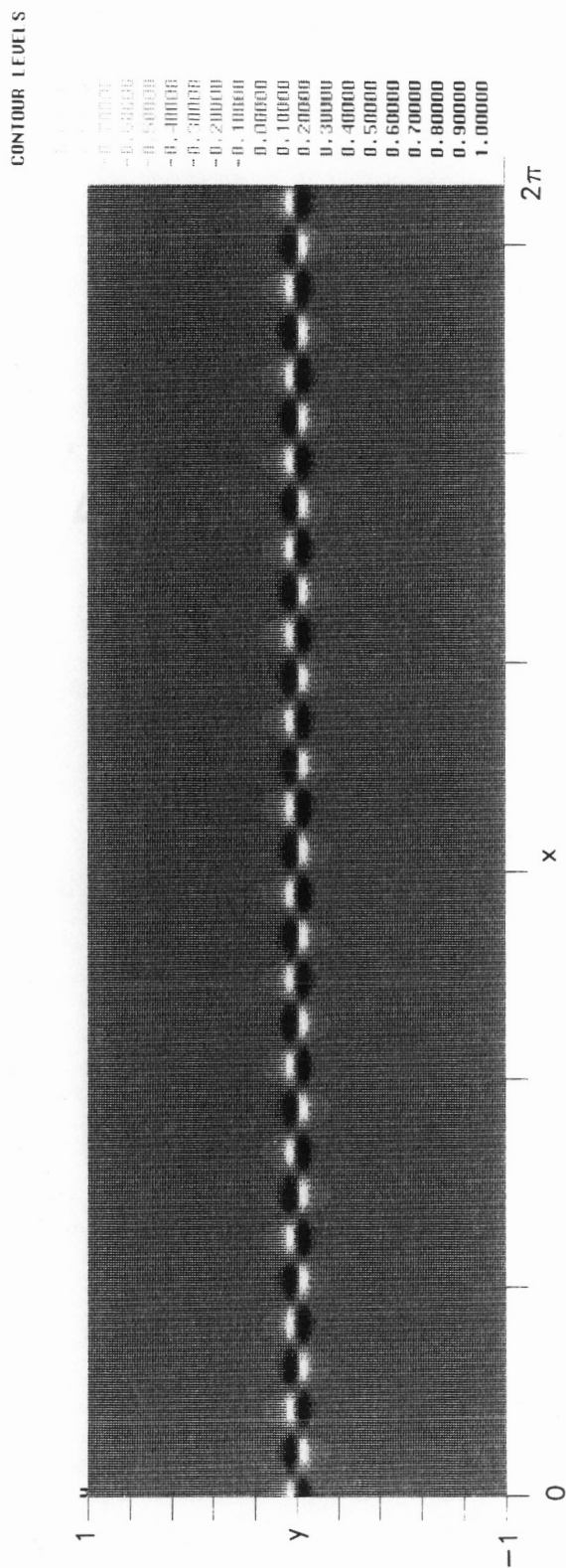


Figure 3.58 Planar jet u velocity disturbance $u'(x, y, z=0, t=0)$; $M=0.75$, $r_{1/2}=0.05$, $k=15.2$

CONTOUR LEVELS

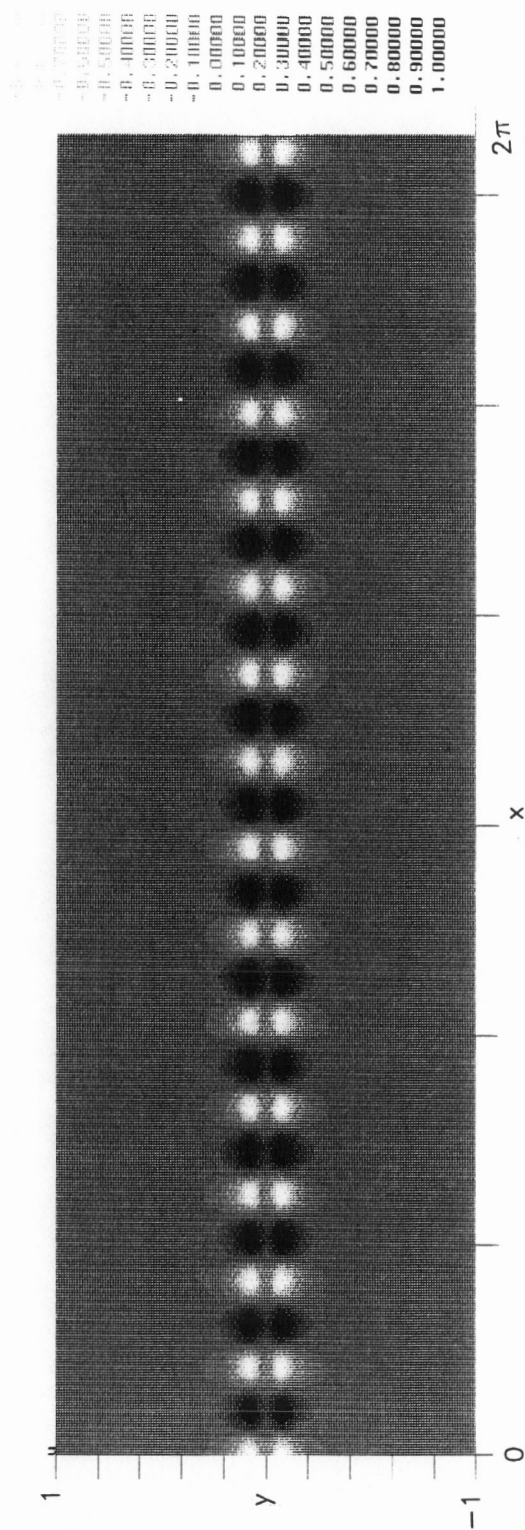


Figure 3.59 Planar jet v velocity disturbance $v'(x,y,z=0,t=0)$; $M=0.75$, $r_{1/2}=0.05$, $k=15.2$

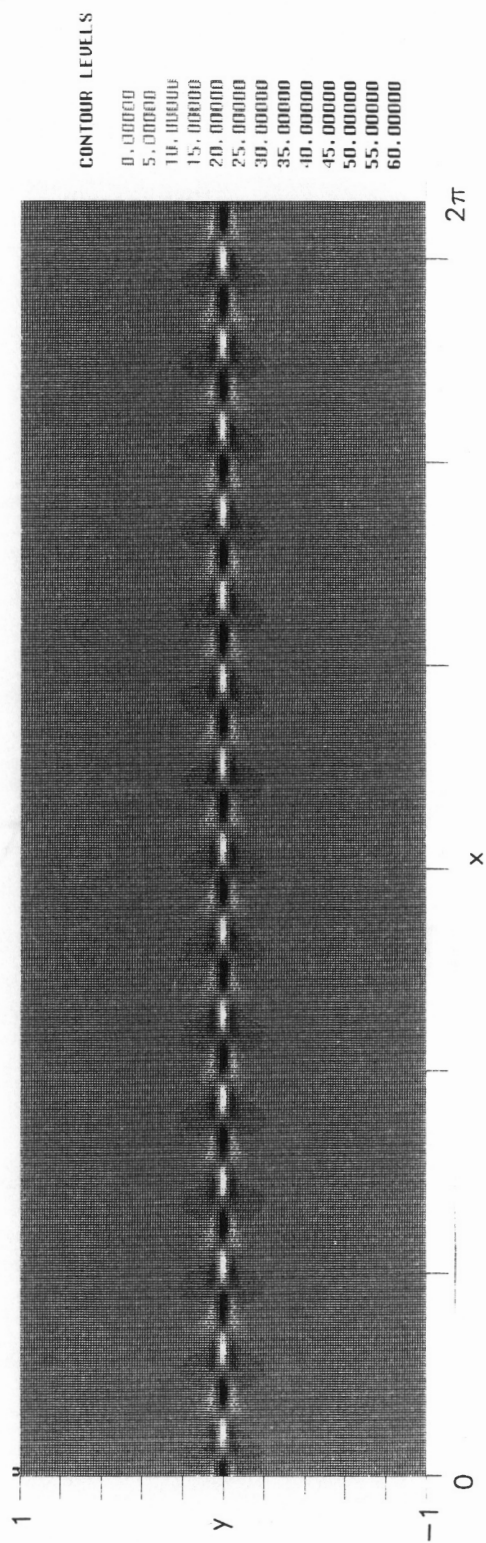


Figure 3.60 Planar jet vorticity disturbance $\Omega'_z(x,y,z=0,t=0)$; $M=0.75$, $r_{1/2}=0.05$, $k=15.2$

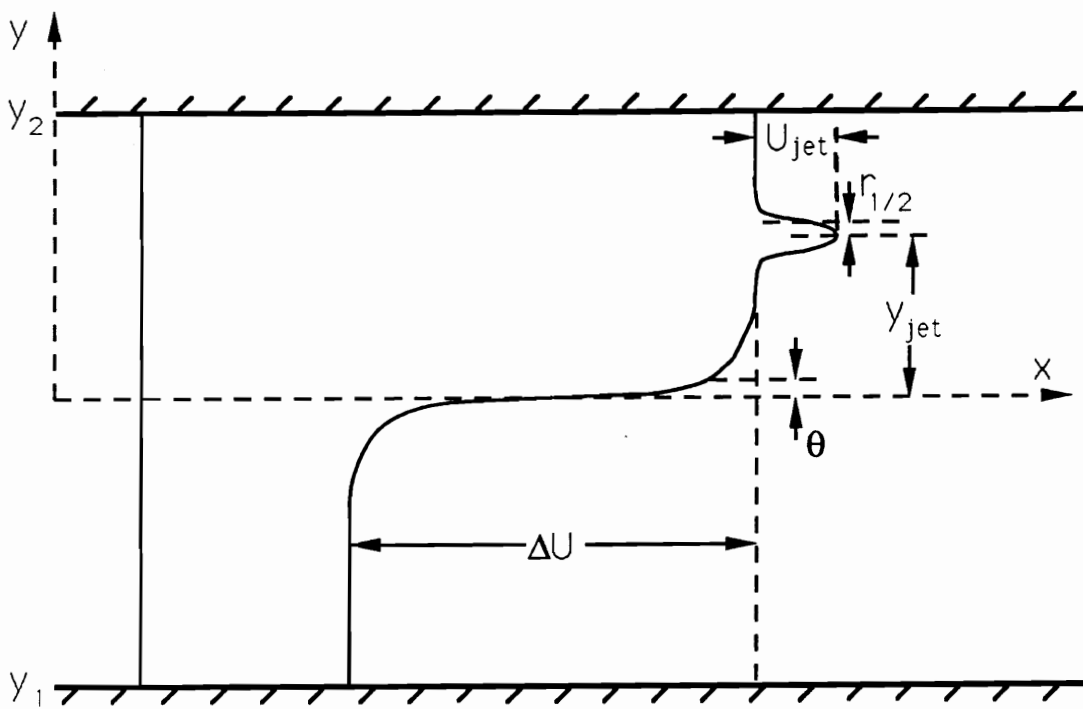


Figure 3.61 Typical jet/shear layer flowfield parameters

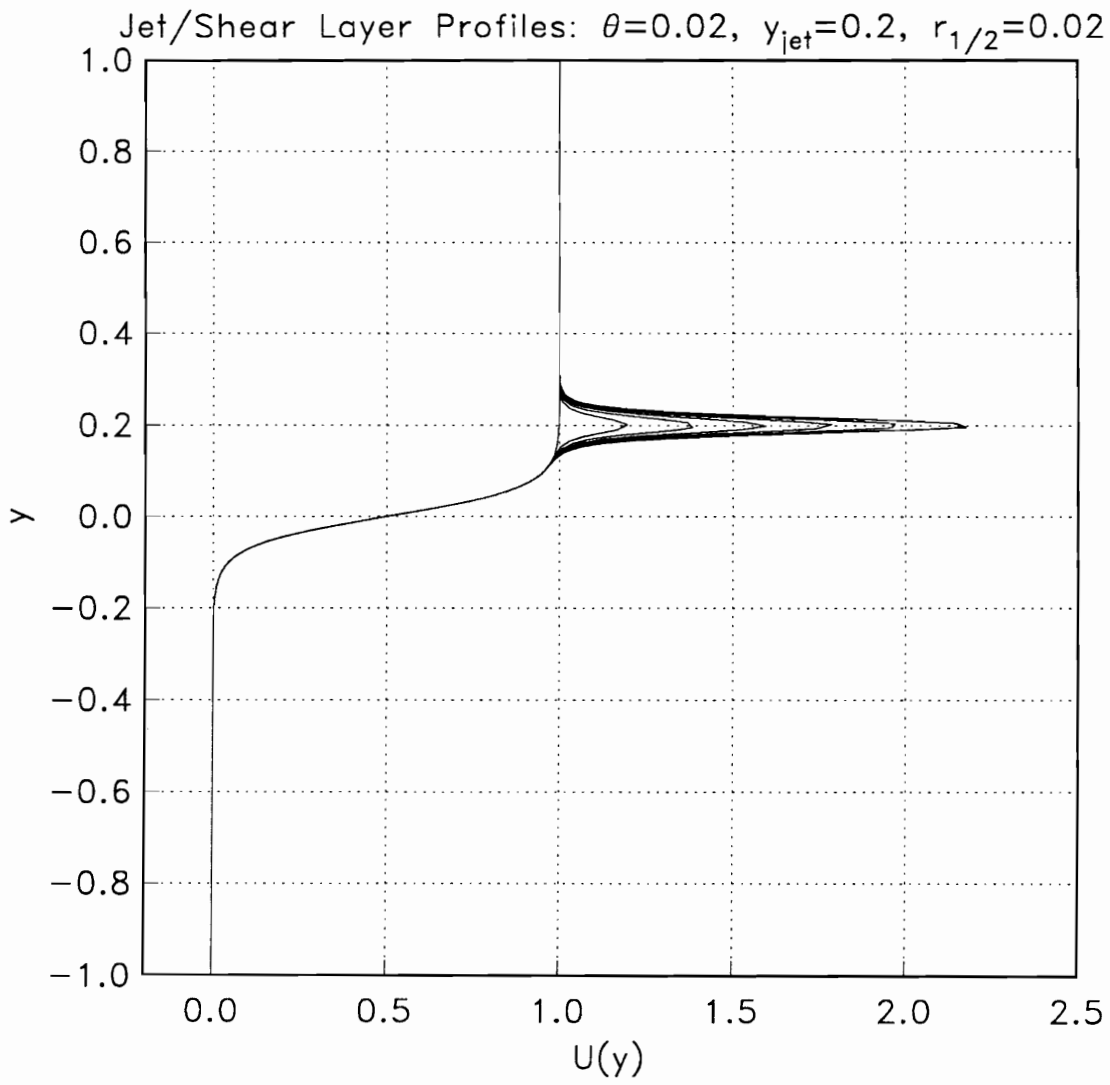


Figure 3.62 Typical jet/shear layer profiles vs. U_{jet} ; $\theta=0.02$, $y_{\text{jet}}=0.2$, $r_{1/2}=0.02$

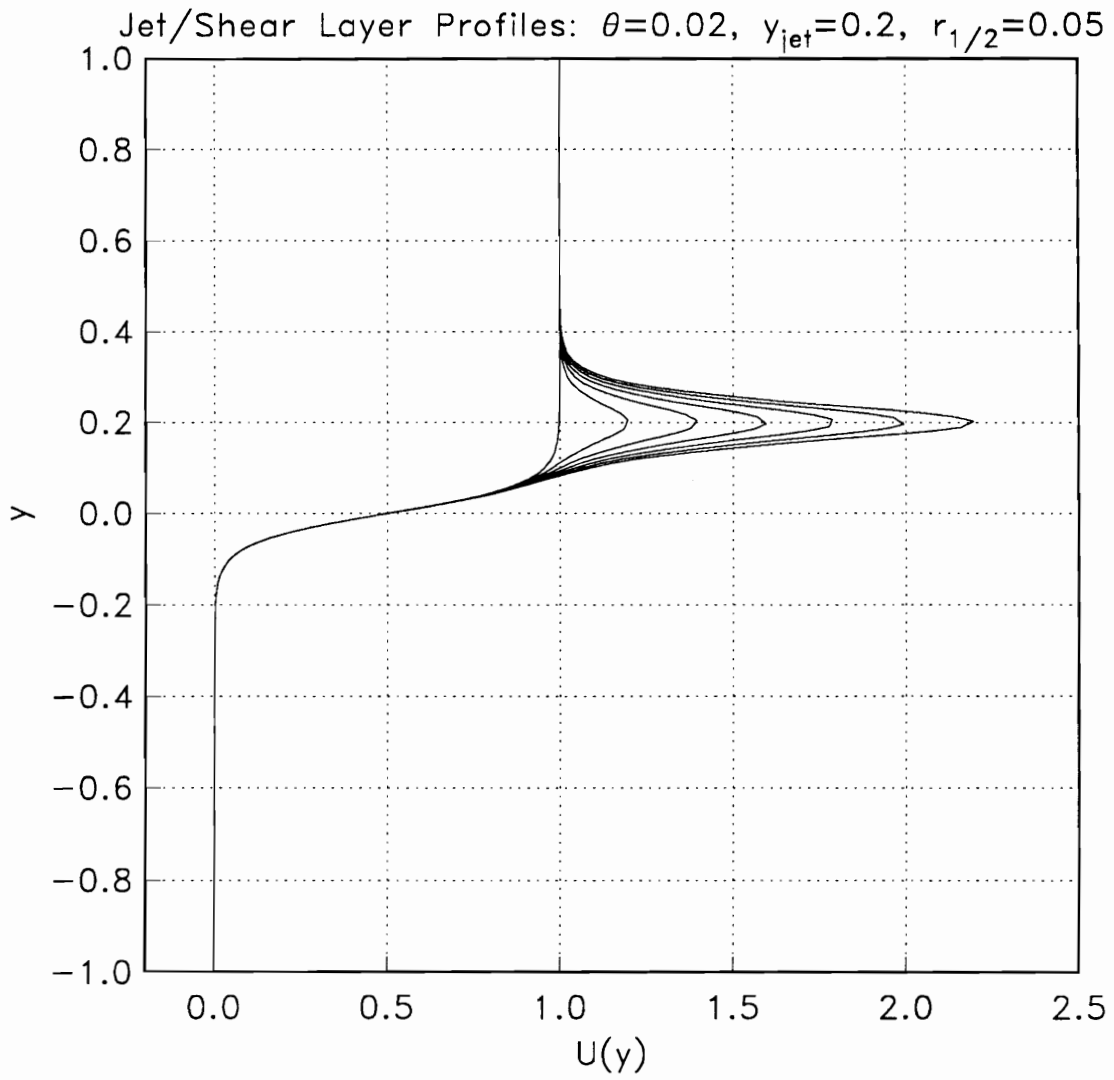


Figure 3.63 Typical jet/shear layer profiles vs. U_{jet} ; $\theta=0.02$, $y_{\text{jet}}=0.2$, $r_{1/2}=0.05$

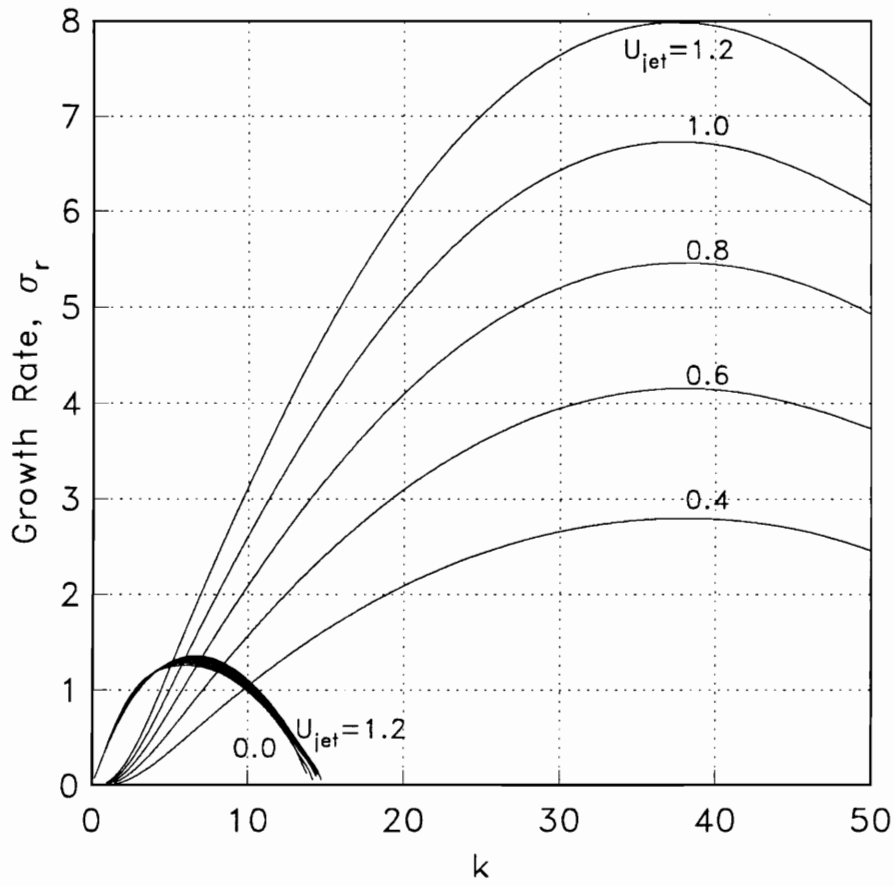


Figure 3.64 Jet/shear layer growth rates vs. k ; $M=0.5$, $\theta=0.02$, $y_{jet}=0.2$,
 $r_{1/2}=0.02$, $\phi=0$

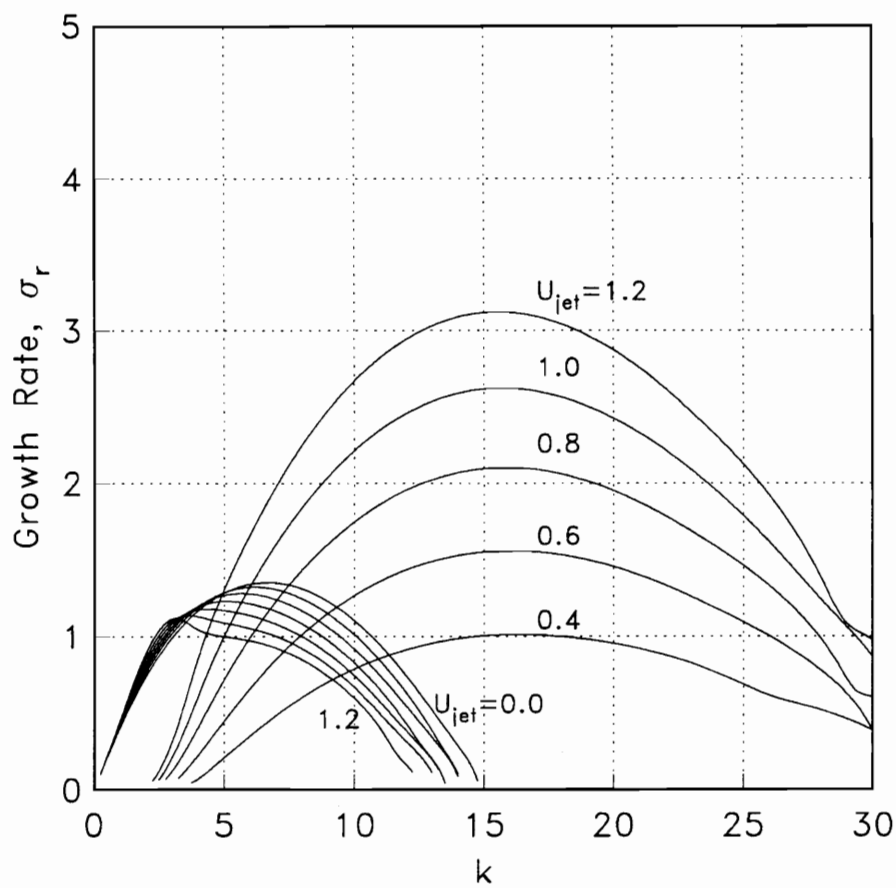


Figure 3.65 Jet/shear layer growth rates vs. k ; $M=0.5$, $\theta=0.02$, $y_{jet}=0.2$,
 $r_{1/2}=0.05$, $\phi=0$

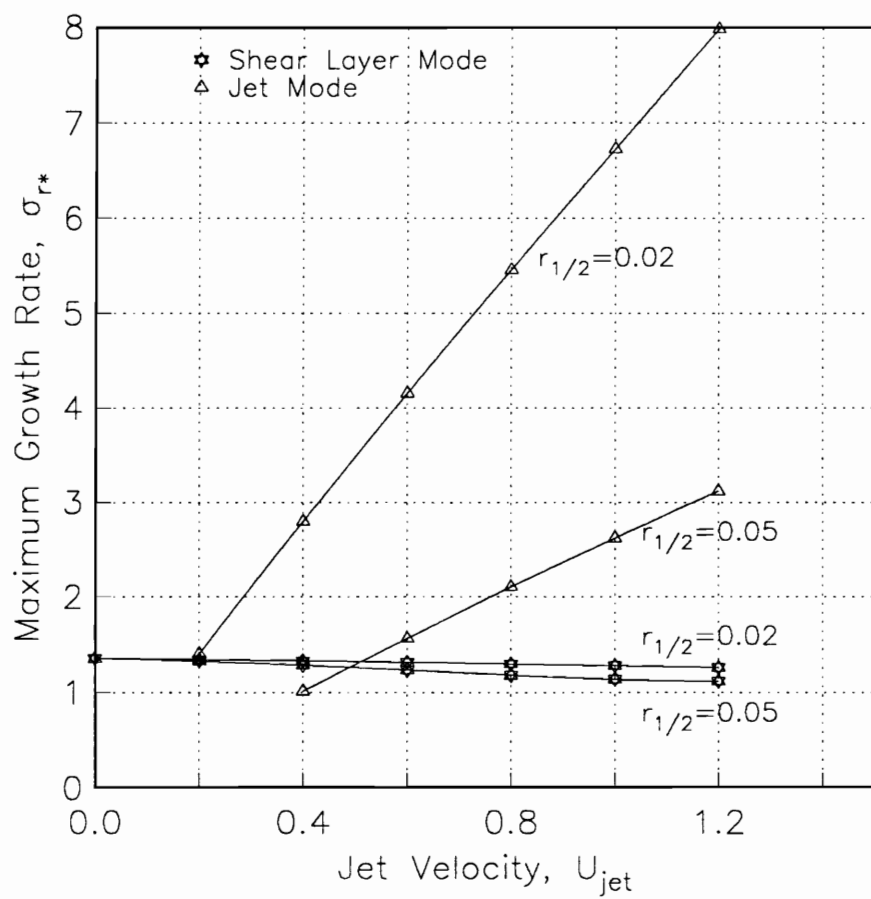


Figure 3.66 Jet/shear layer maximum growth rates vs. U_{jet} ; $M=0.5$, $\theta=0.02$, $y_{jet}=0.2$, $\phi=0$

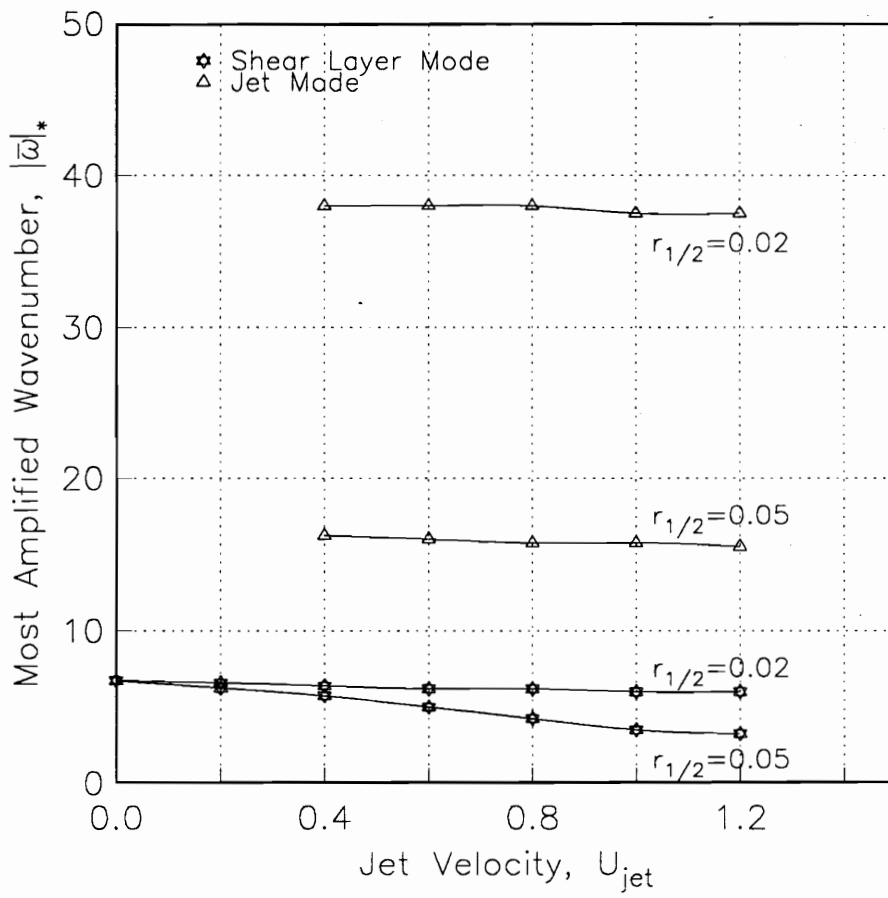


Figure 3.67 Jet/shear layer most amplified wavenumber vs. U_{jet} : $M=0.5$,
 $\theta=0.02$, $y_{jet}=0.2$, $\phi=0$

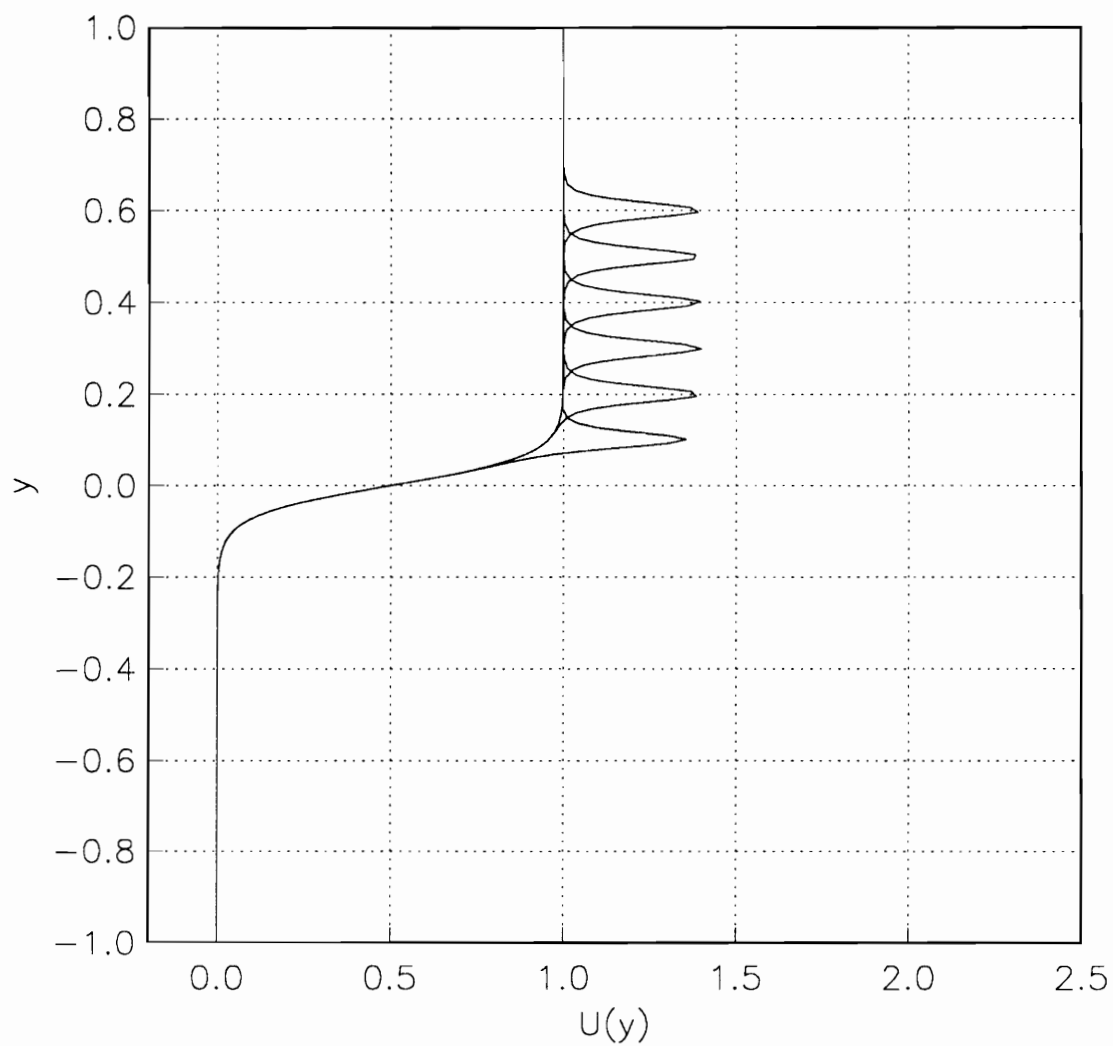


Figure 3.68 Typical jet/shear layer profiles vs. y_{jet} ; $\theta=0.02$, $U_{jet}=0.4$, $r_{1/2}=0.02$

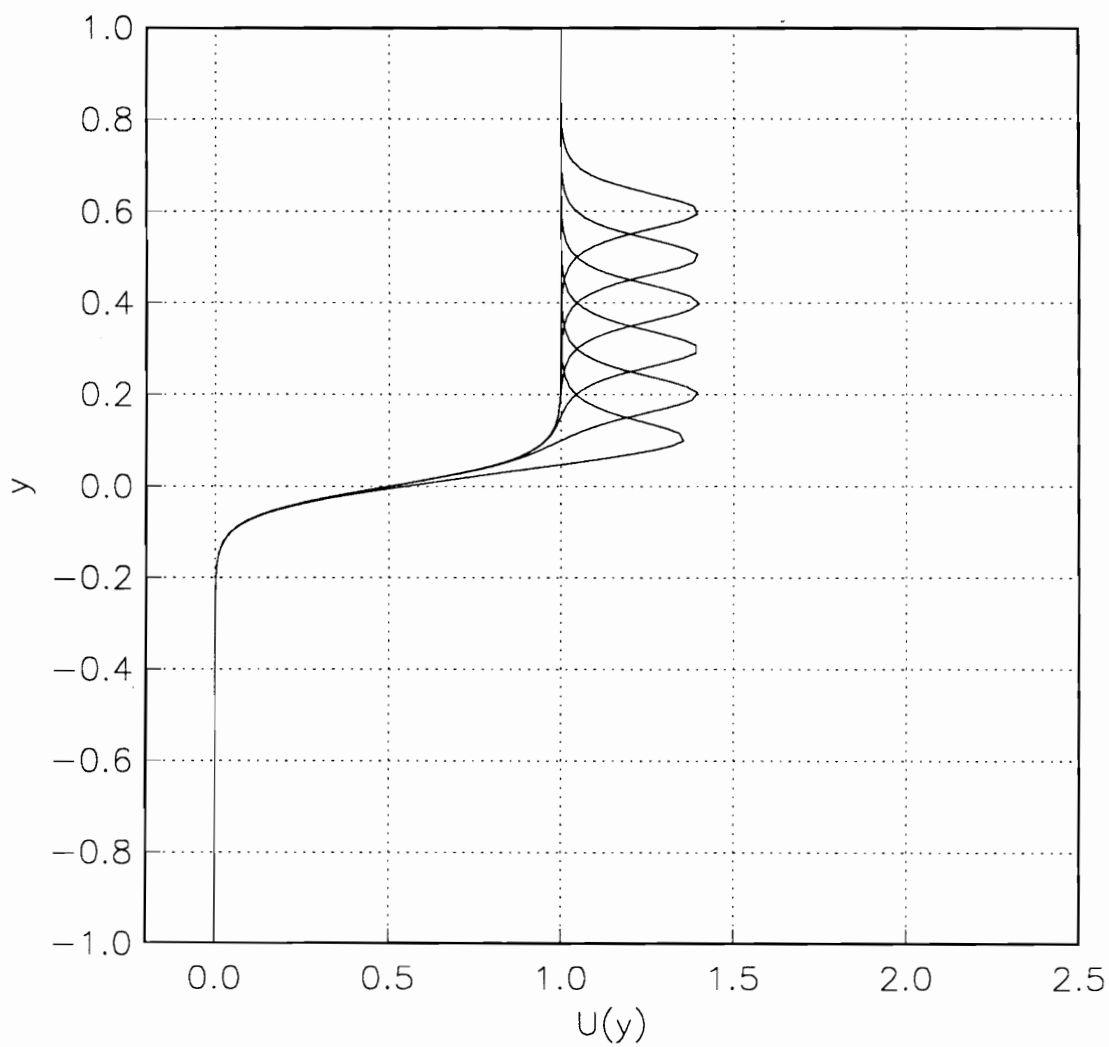


Figure 3.69 Typical jet/shear layer profiles vs. y_{jet} ; $\theta=0.02$, $U_{\text{jet}}=0.4$, $r_{1/2}=0.05$

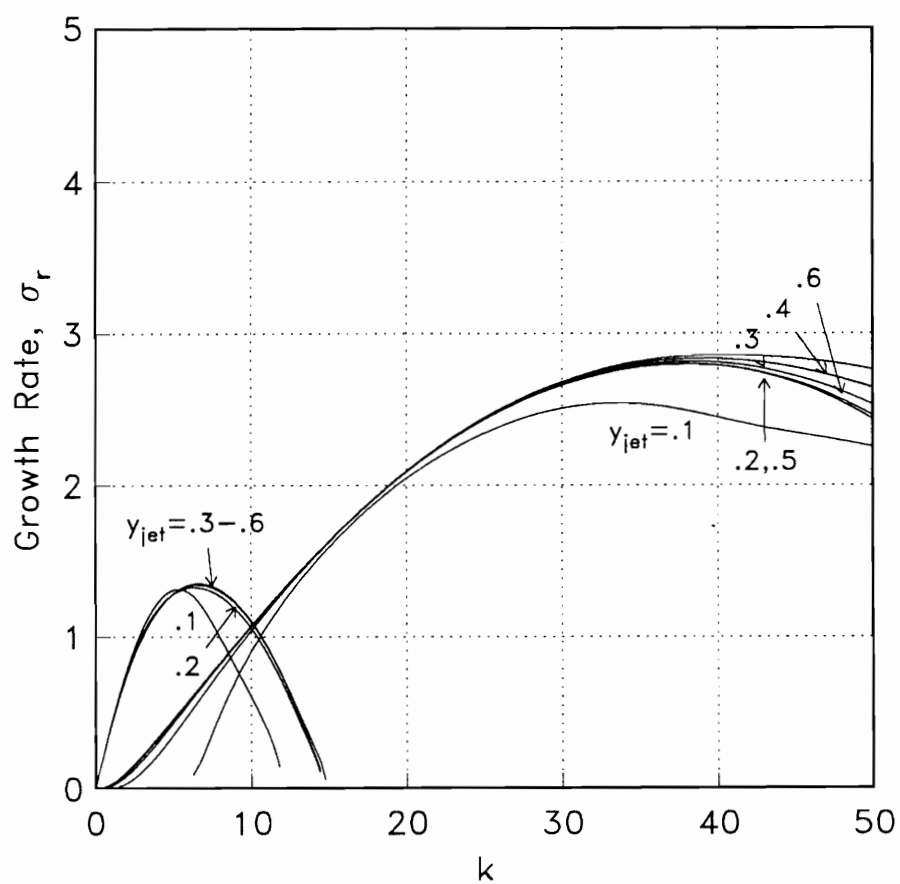


Figure 3.70 Jet/shear layer growth rates vs. k ; $M=0.5$, $\theta=0.02$, $U_{jet}=0.4$,
 $r_{1/2}=0.02$, $\phi=0$

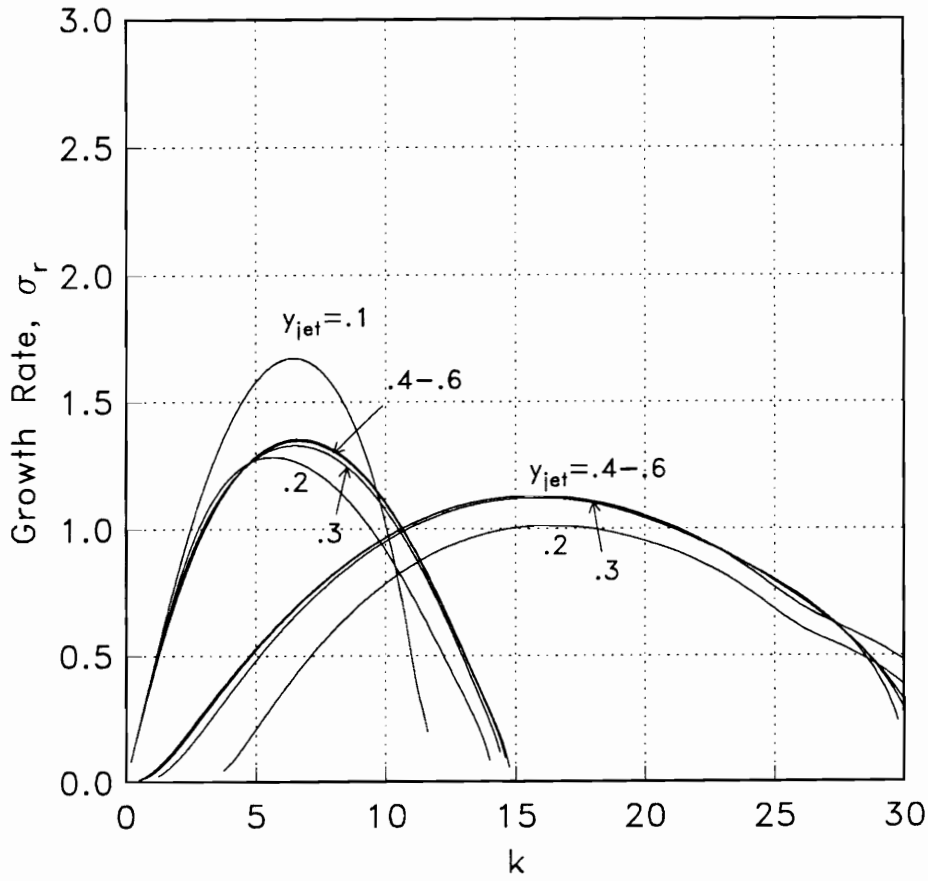


Figure 3.71 Jet/shear layer growth rates vs. k ; $M=0.5$, $\theta=0.02$, $U_{jet}=0.4$, $r_{1/2}=0.05$, $\phi=0$

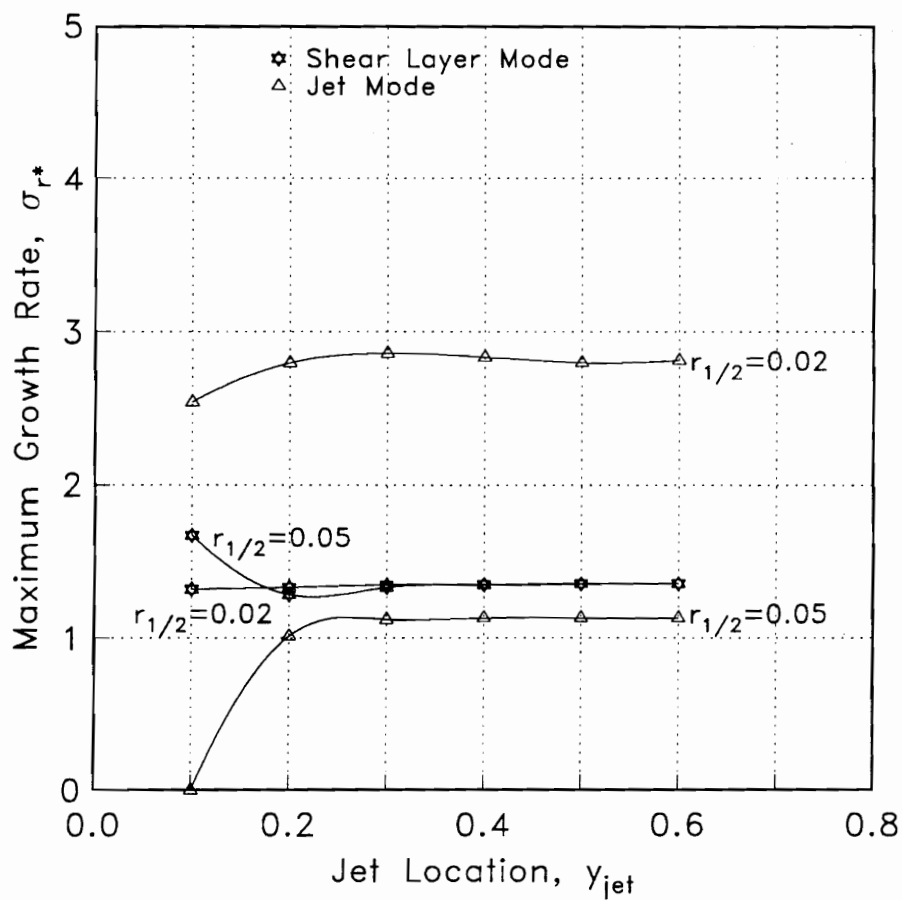


Figure 3.72 Jet/shear layer maximum growth rates vs. y_{jet} ; $M=0.5$, $\theta=0.02$,
 $U_{jet}=0.4$, $\phi=0$

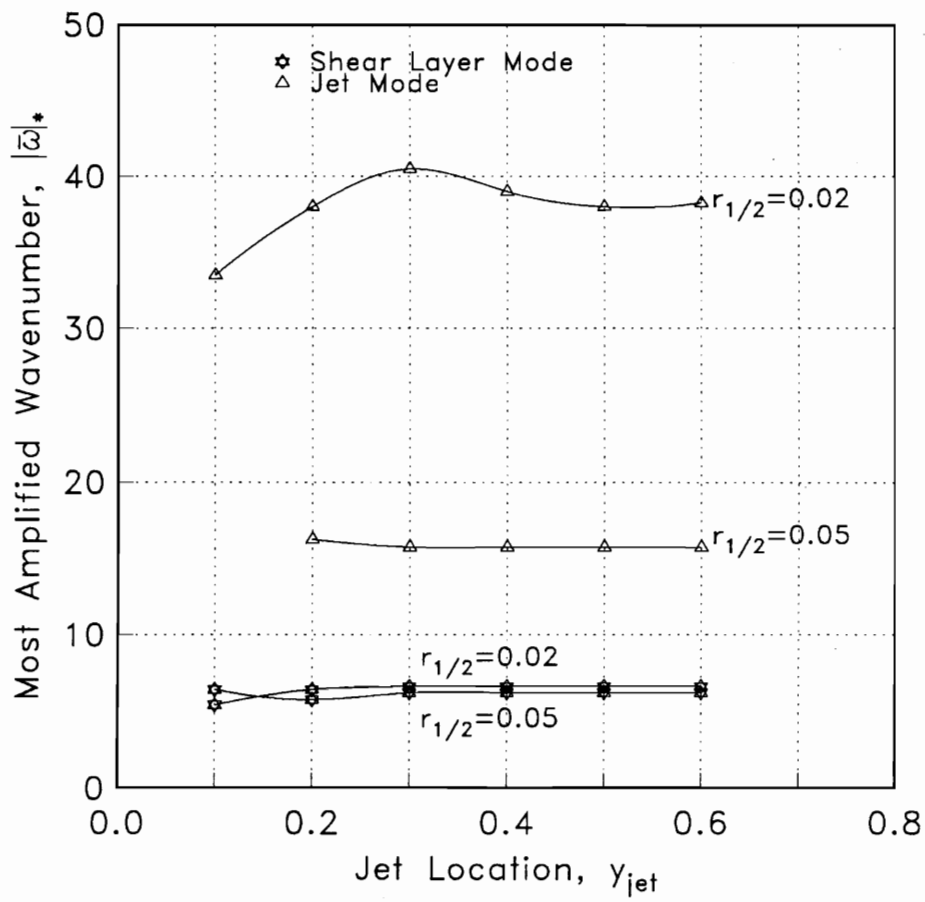


Figure 3.73 Jet/shear layer most amplified wavenumber vs. y_{jet} ; $M=0.5$, $\theta=0.02$, $U_{jet}=0.4$, $\phi=0$

Case	Primary Stream M=2.0 p_1 (psia)	Secondary Stream M=1.2 p_2 (psia)
1 (baseline)	7.0	7.0
2	7.0	8.7
3	7.0	11.0
4	7.5	7.0
5	7.1	5.0

Figure 4.1 APL experiment test conditions $\alpha=0.02$; M=1.5, $\theta=0.02$, k=6.5.

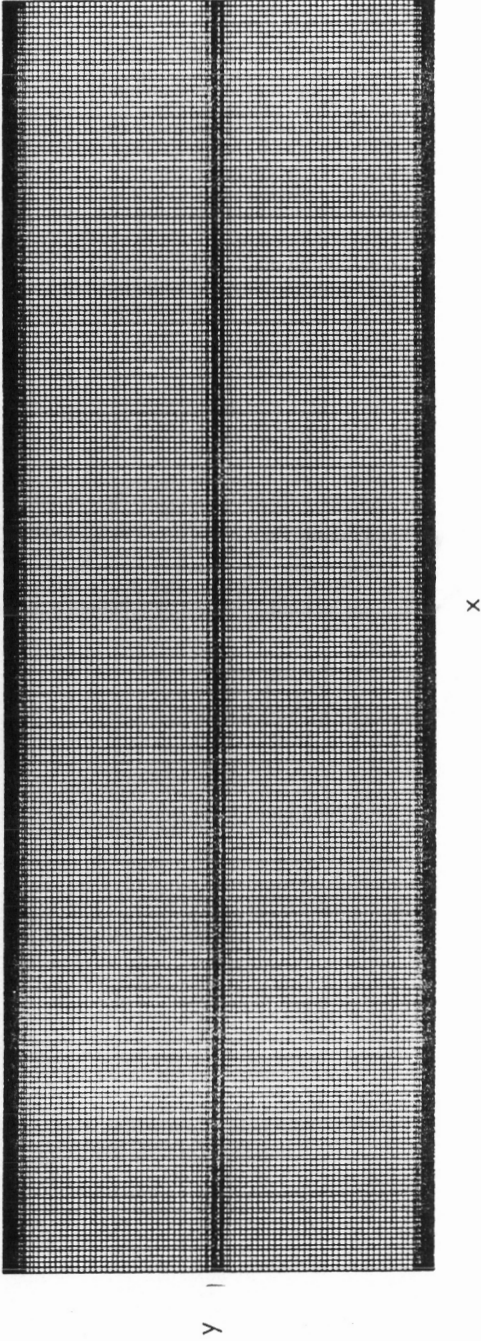


Figure 4.2 Typical numerical grid for PNS calculations

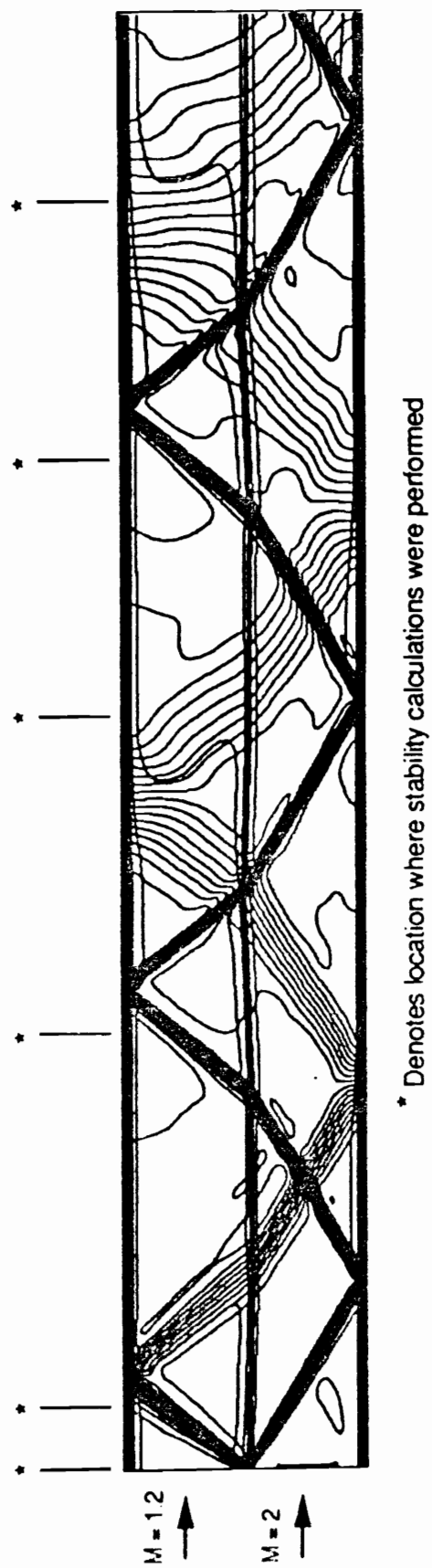


Figure 4.3 Computed velocity and pressure contours for APL Case 2

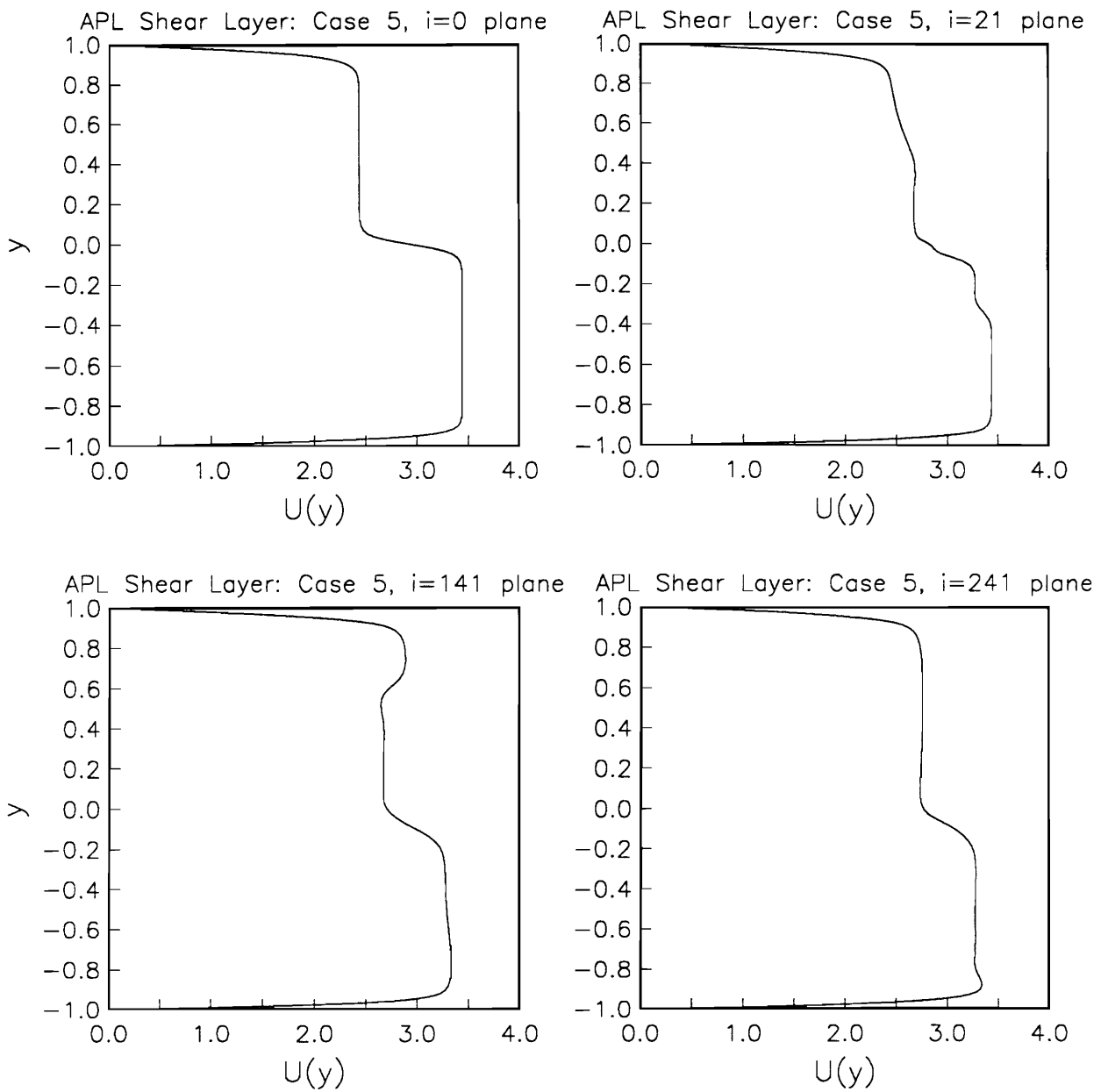


Figure 4.4 Computed u velocity profiles at each axial station for APL Case 5

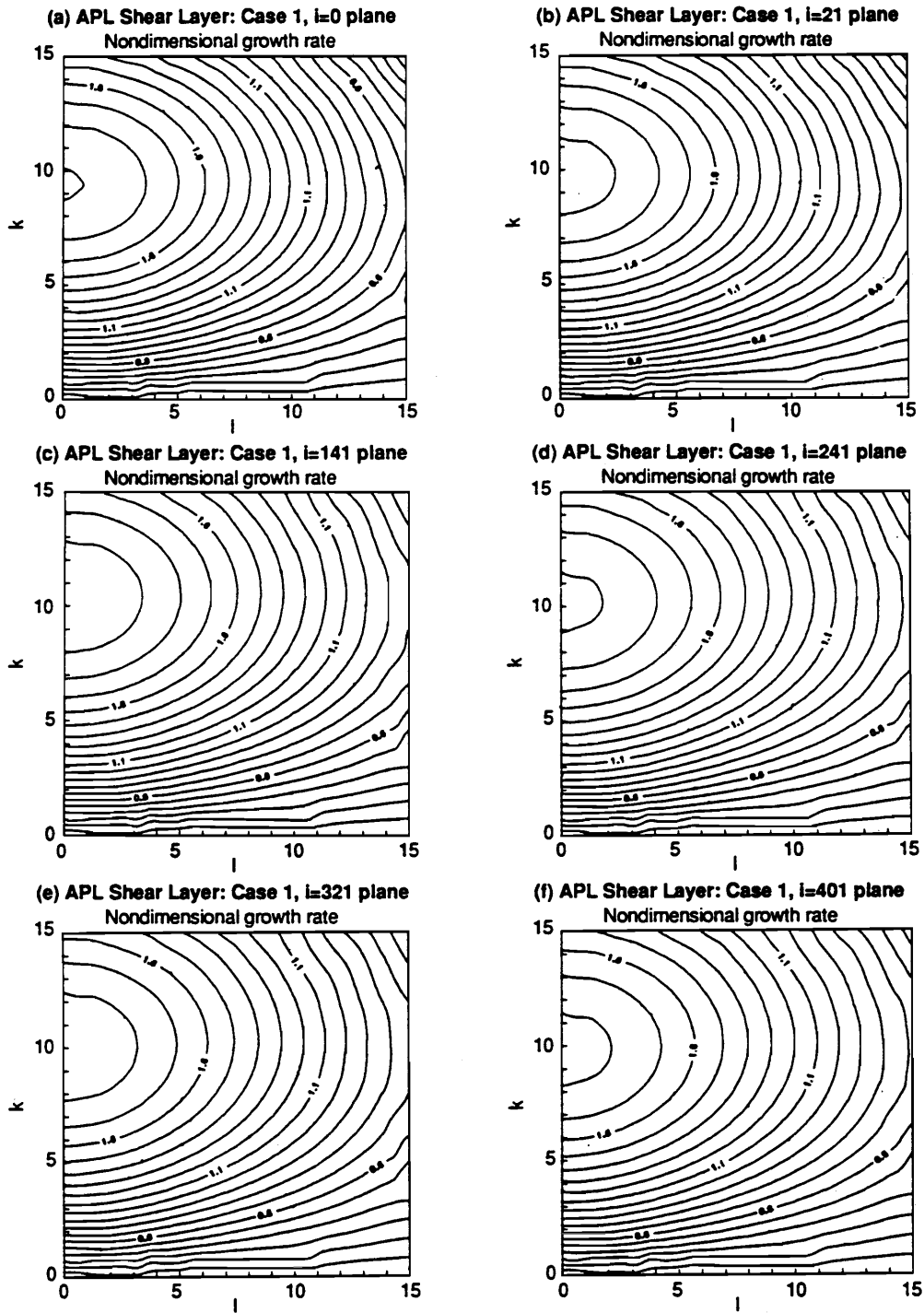


Figure 4.5 Growth rate planes at each axial station for APL Case 1

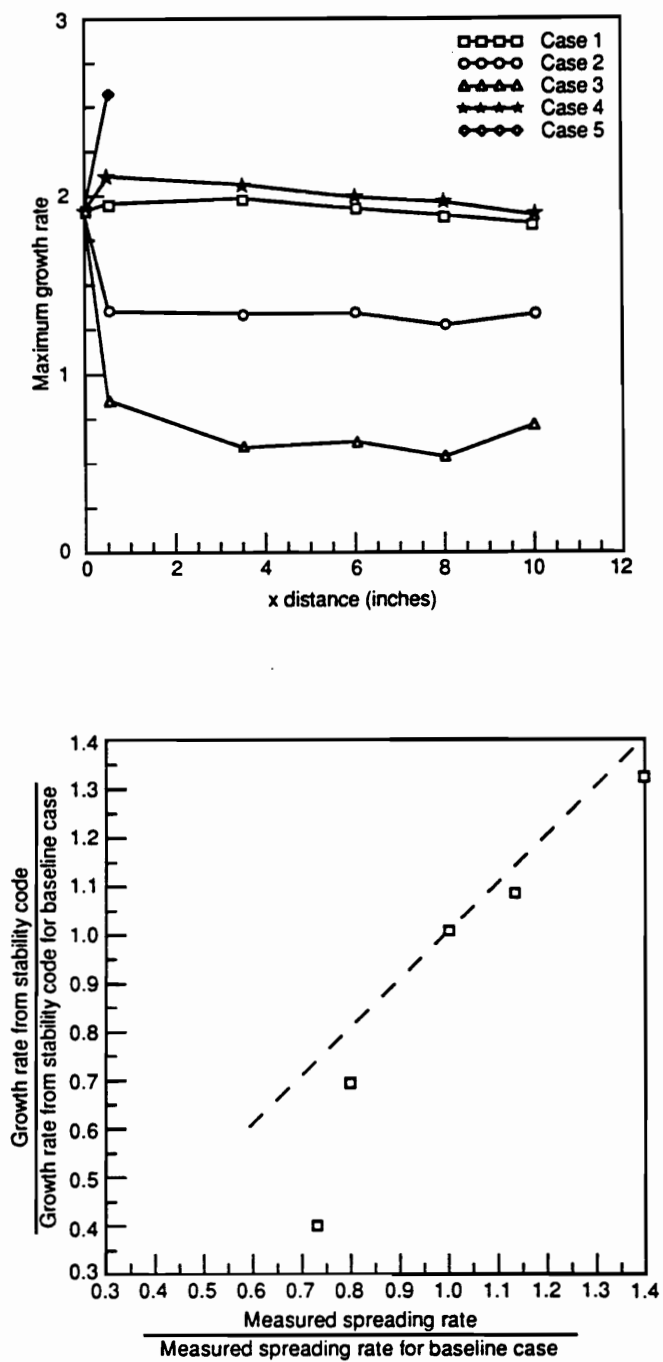


Figure 4.6 (a) Maximum growth rates; (b) comparison of growth rates vs. $\beta=4.5$.
measured spreading rates

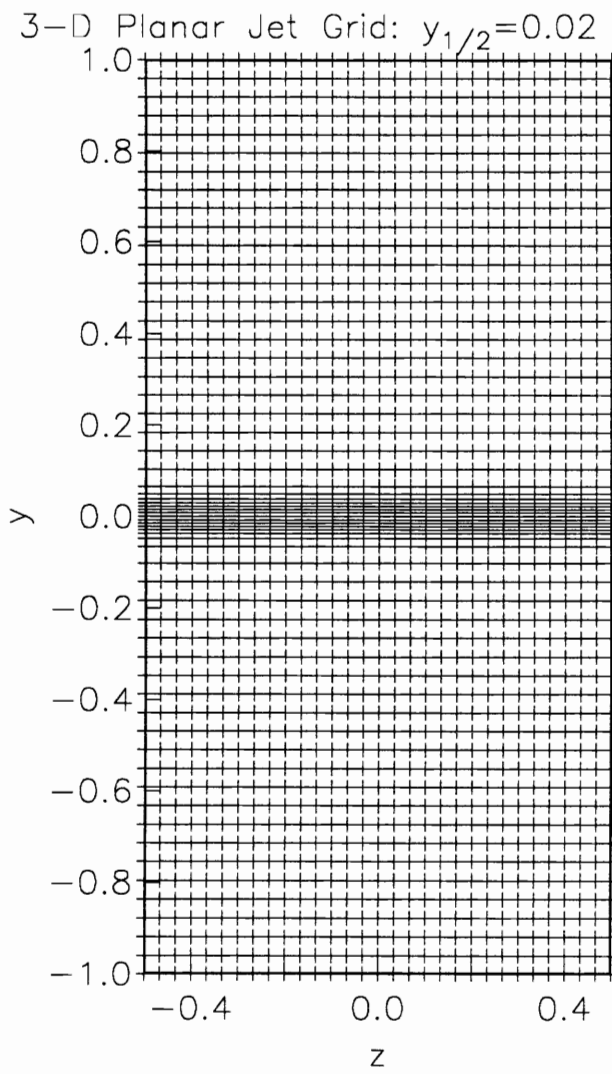


Figure 6.1 Typical computational grid for 3-D shear layer and planar jet;
61 x 31 points

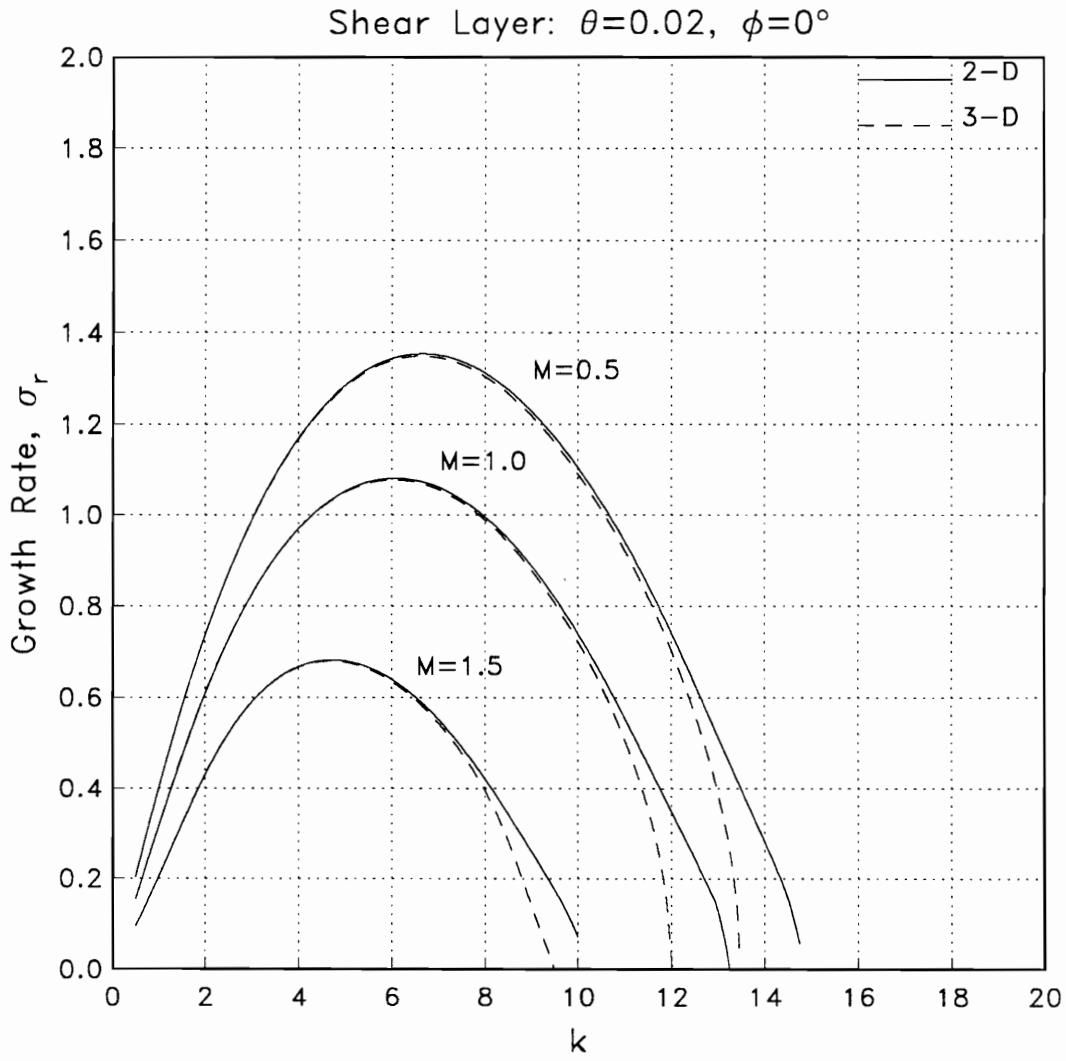


Figure 6.2 Comparison of 2-D and 3-D shear layer growth rates vs. k ; $\theta=0.02$

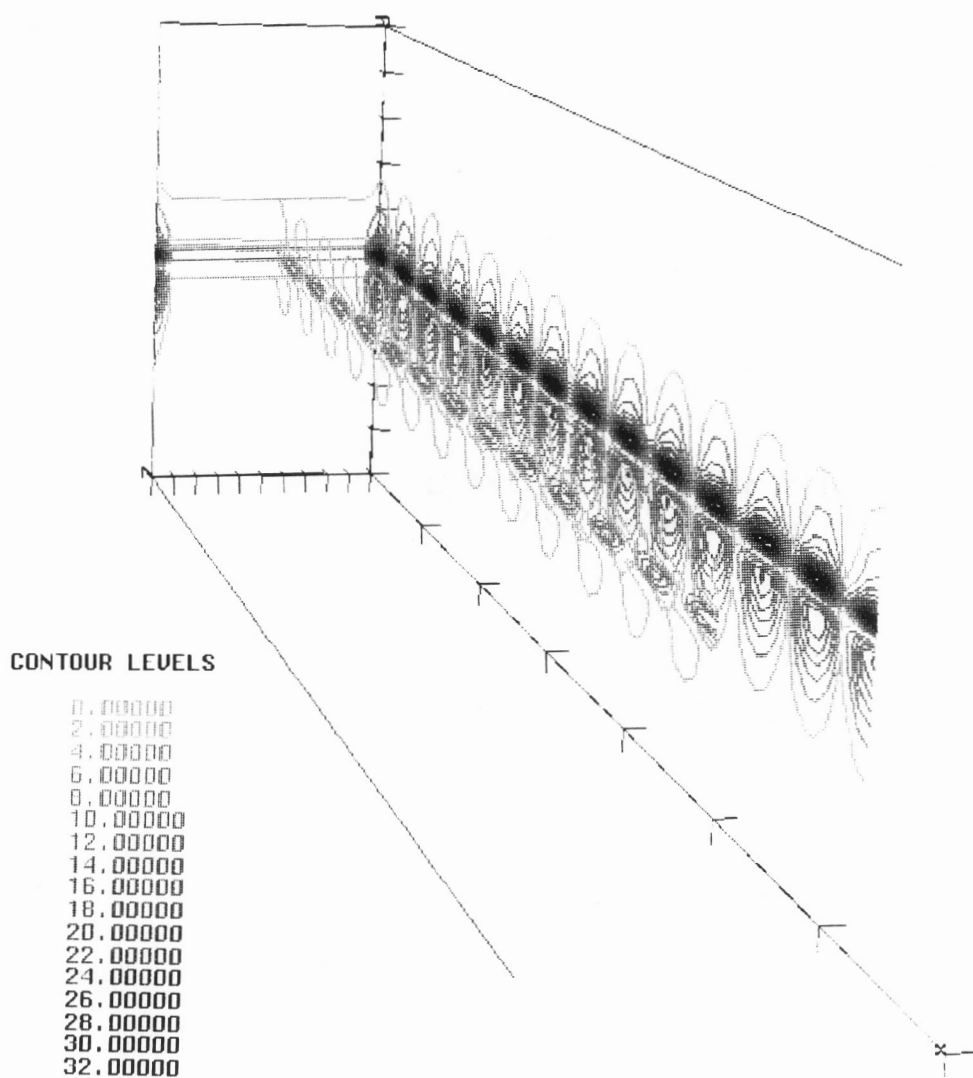


Figure 6.3 3-D shear layer vorticity disturbance magnitude; $M=0.5$, $\theta=0.02$, $k=6.5$

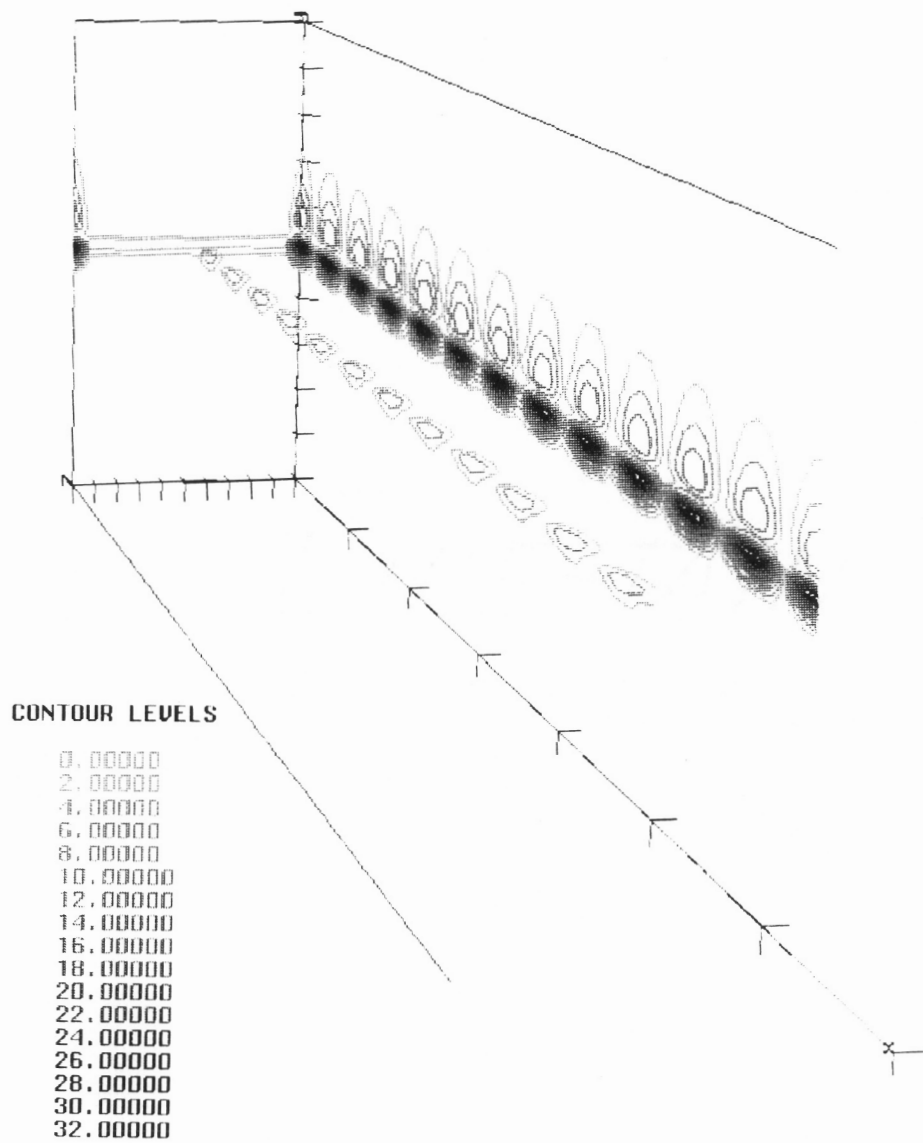


Figure 6.4 3-D shear layer vorticity disturbance magnitude; $M=1.0$, $\theta=0.02$,
 $k=6.5$

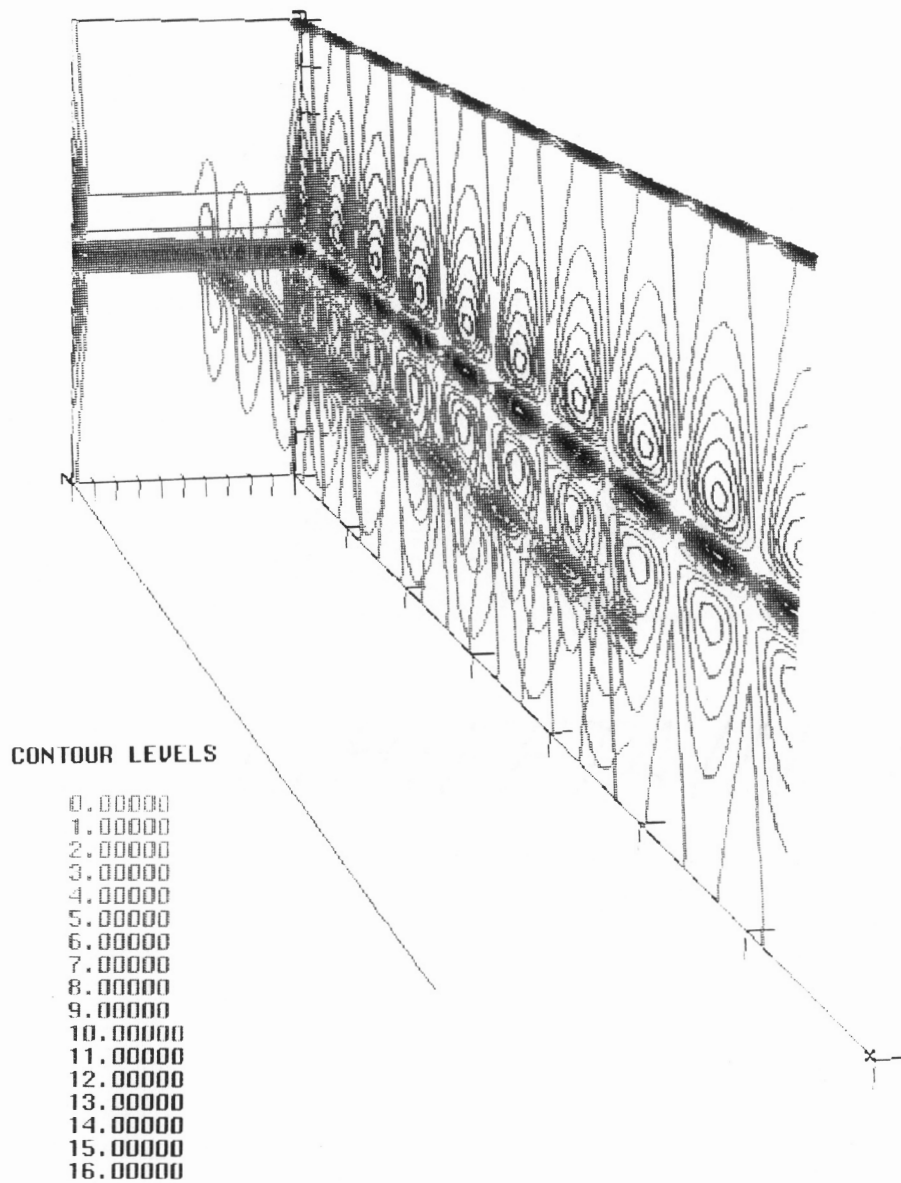


Figure 6.5 3-D shear layer vorticity disturbance magnitude; $M=1.5$, $\theta=0.02$, $k=6.5$

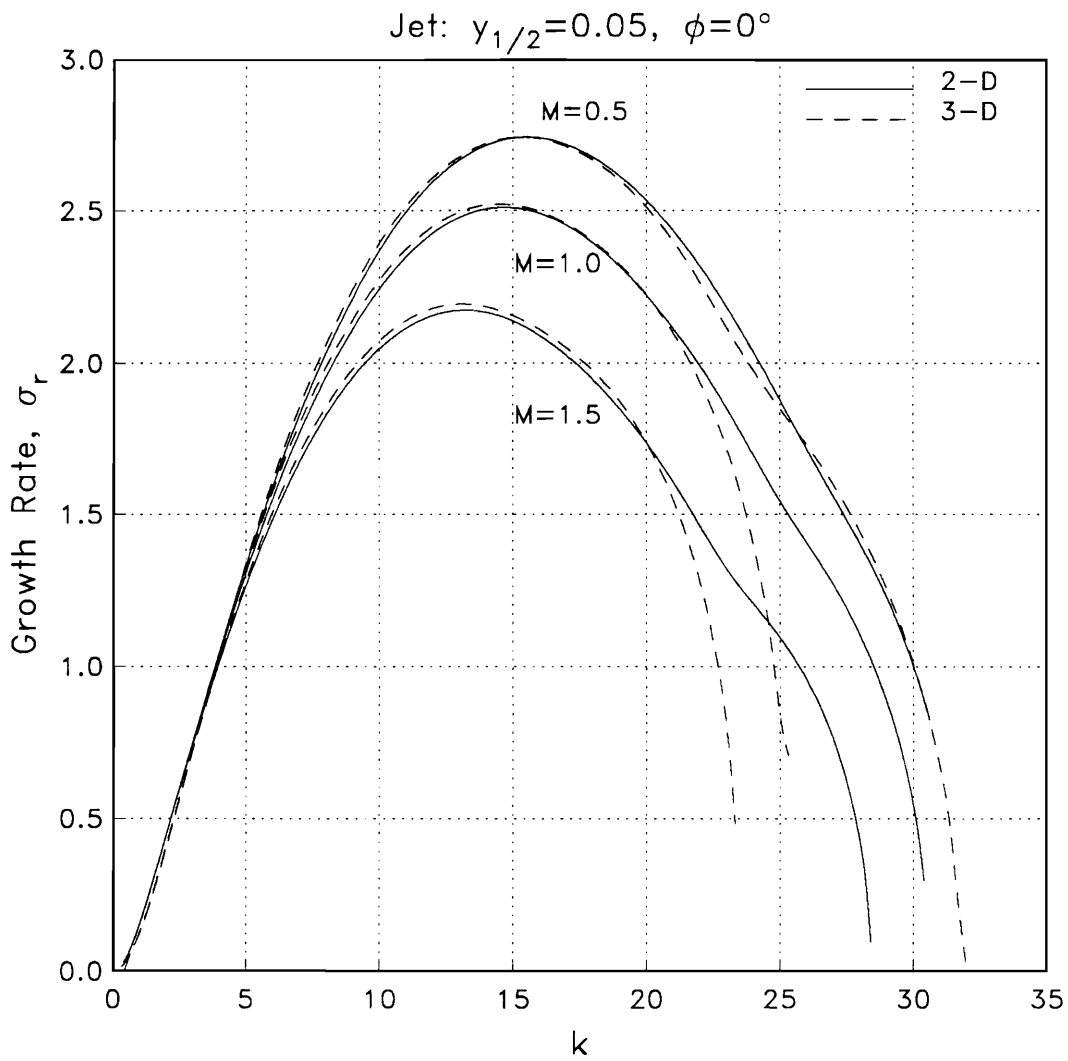


Figure 6.6 Comparison of 2-D and 3-D planar jet growth rates; $y = 0.05$, $\phi = 0$

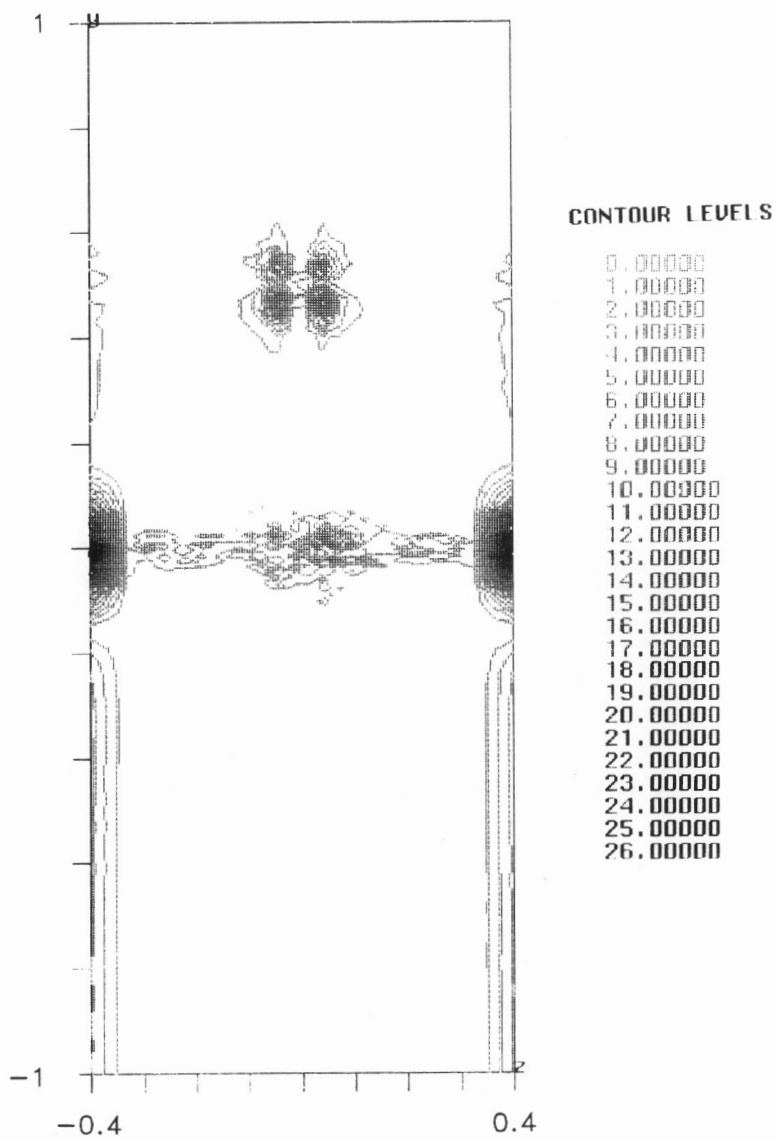


Figure 6.7 3-D jet/shear layer vorticity eigenfunction; $M=1.5$, $\theta=0.02$,
 $r_{1/2}=0.05$, $k=1.0$

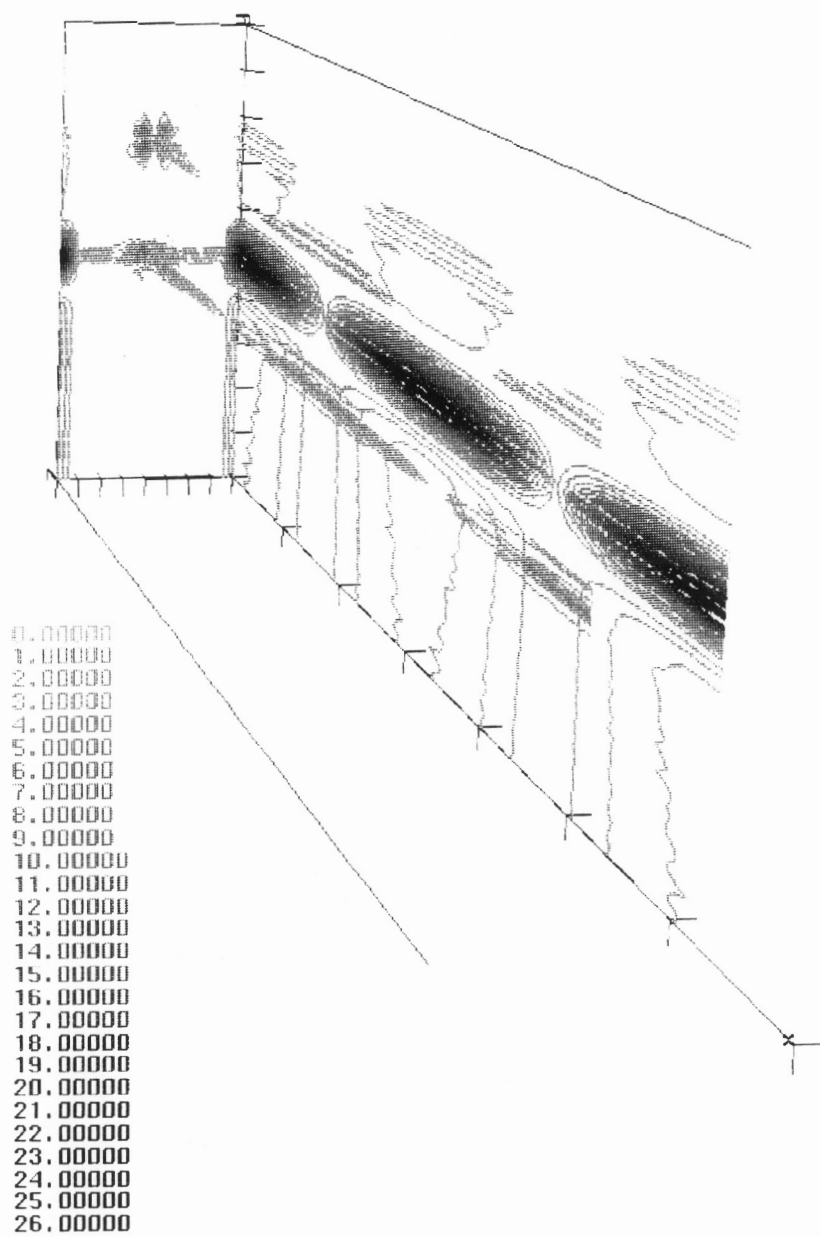


Figure 6.8 3-D jet/shear layer vorticity disturbance magnitude; $M=1.5$, $\theta=0.02$,
 $r_{1/2}=0.05$, $k=1.0$

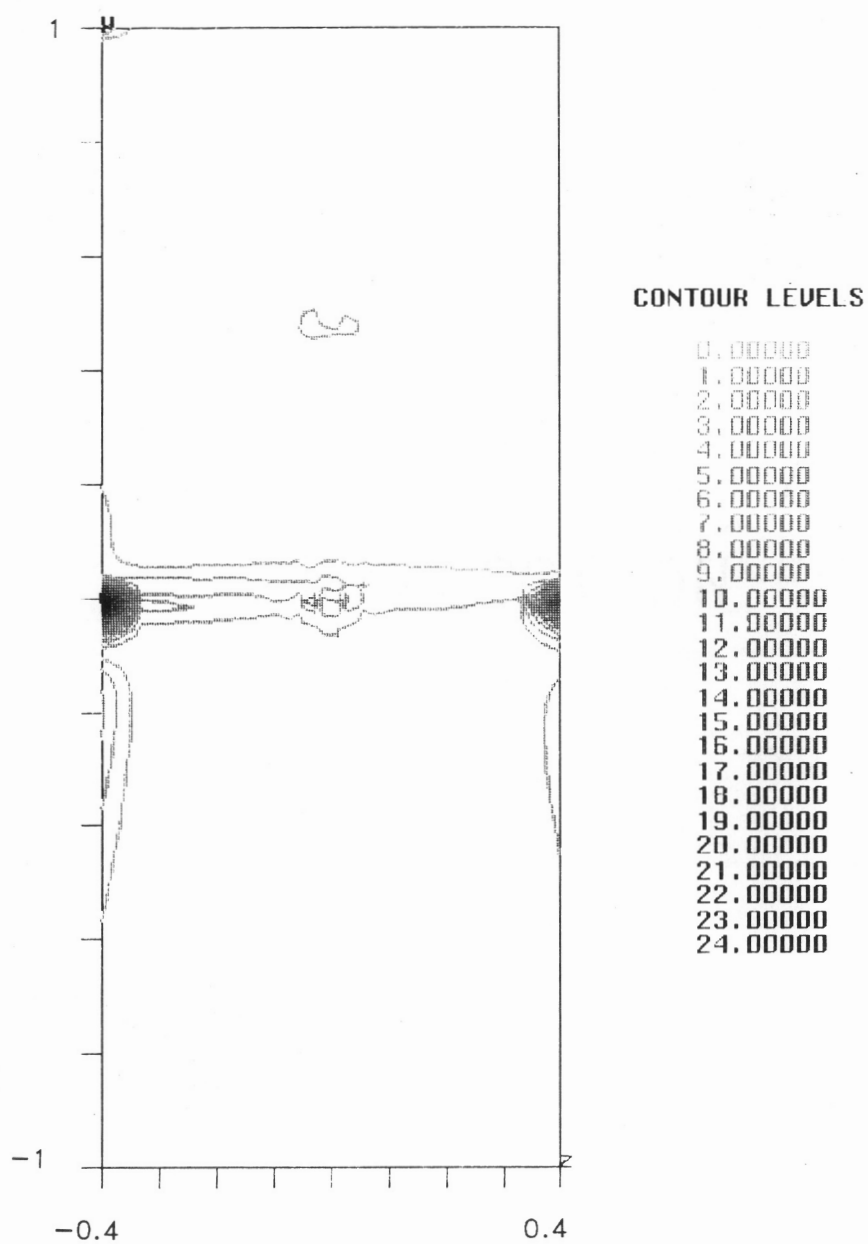


Figure 6.9 3-D jet/shear layer vorticity eigenfunction; $M=1.5$, $\theta=0.03$,
 $r_{1/2}=0.05$, $k=4.5$

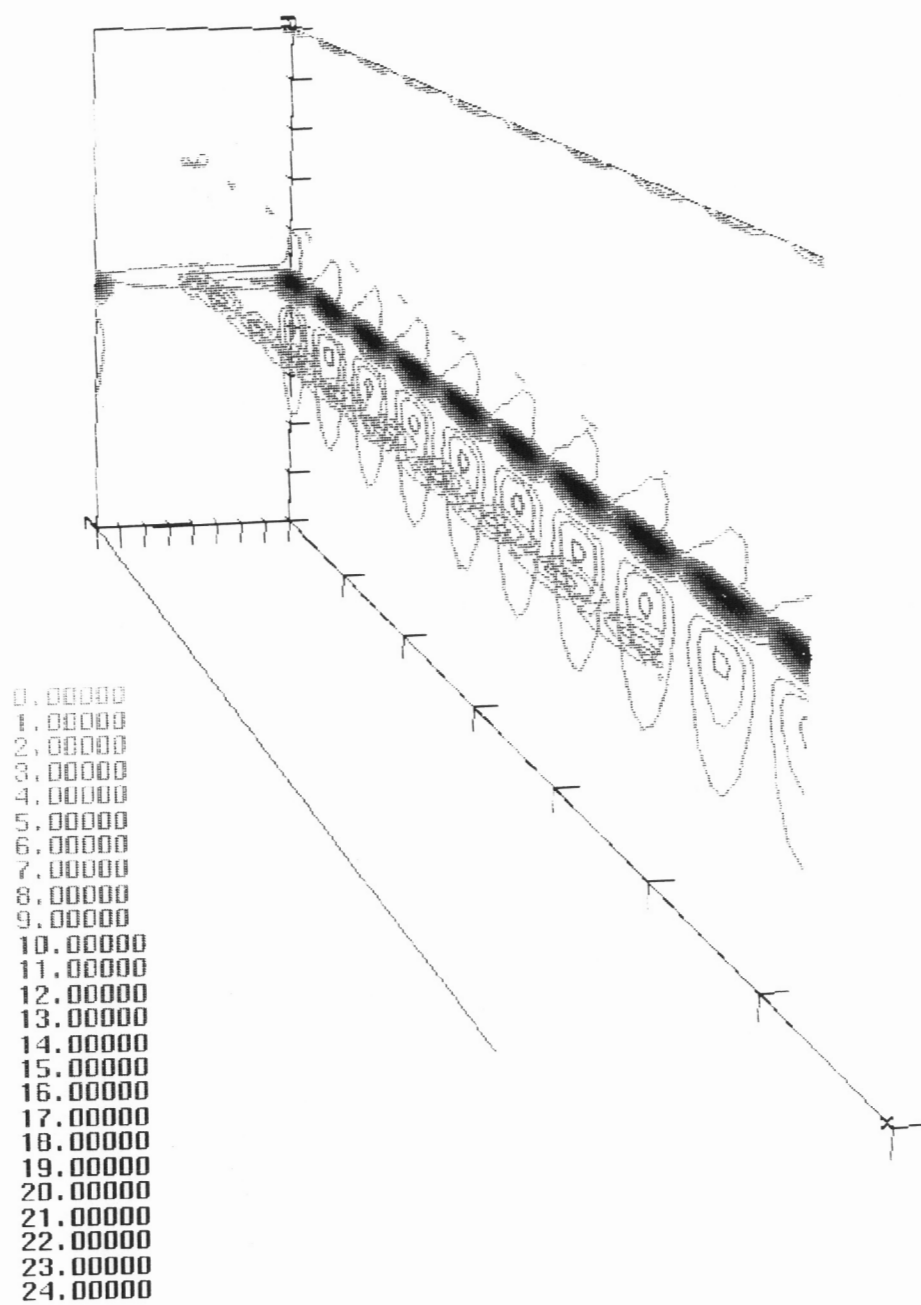


Figure 6.10 3-D jet/shear layer vorticity disturbance magnitude; $M=1.5$,
 $\theta=0.03$, $r_{1/2}=0.05$, $k=4.5$

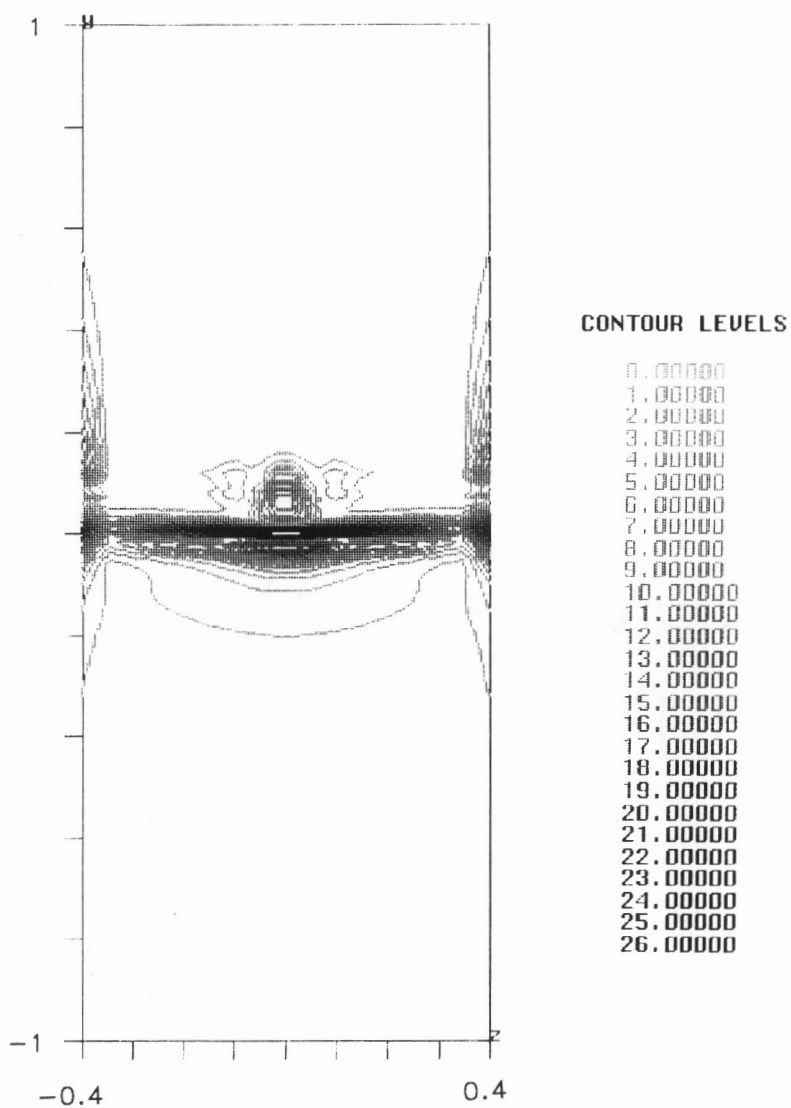


Figure 6.11 3-D jet/shear layer vorticity eigenfunction; $M=0.5$, $\theta=0.03$,
 $r_{1/2}=0.05$, $k=4.5$

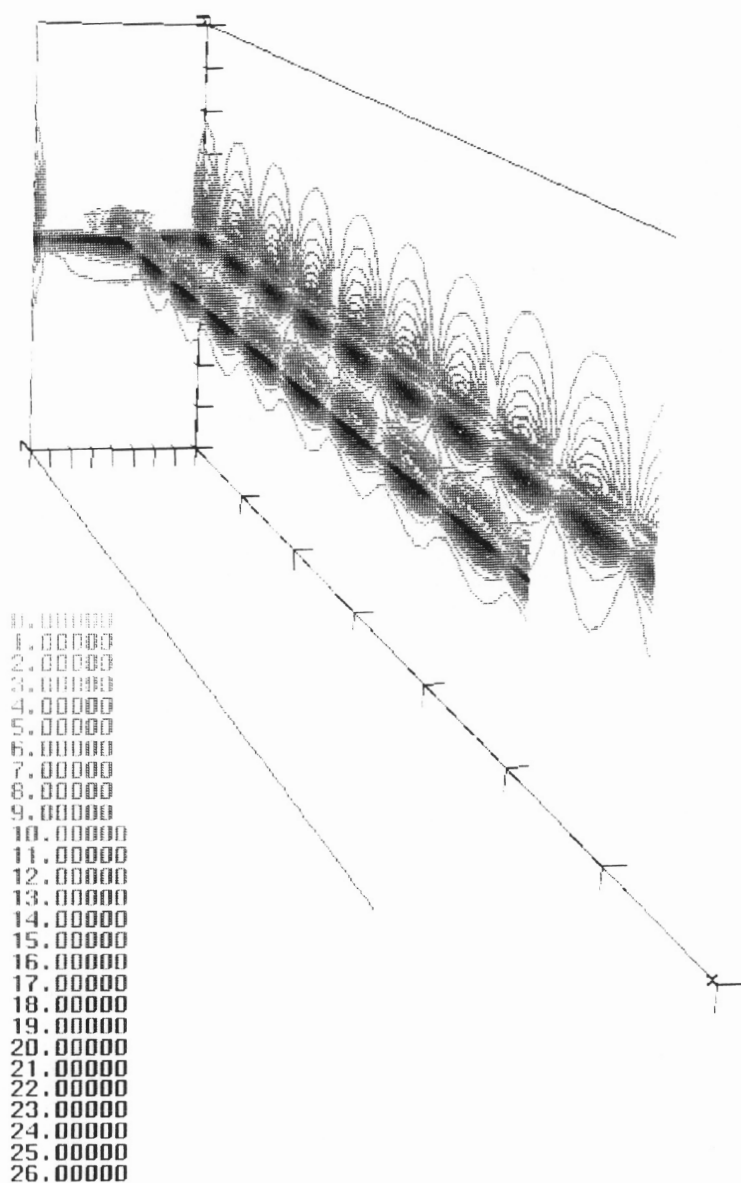


Figure 6.12 3-D jet/shear layer vorticity disturbance magnitude; $M=0.5$,
 $\theta=0.03$, $r_{1/2}=0.05$, $k=4.5$

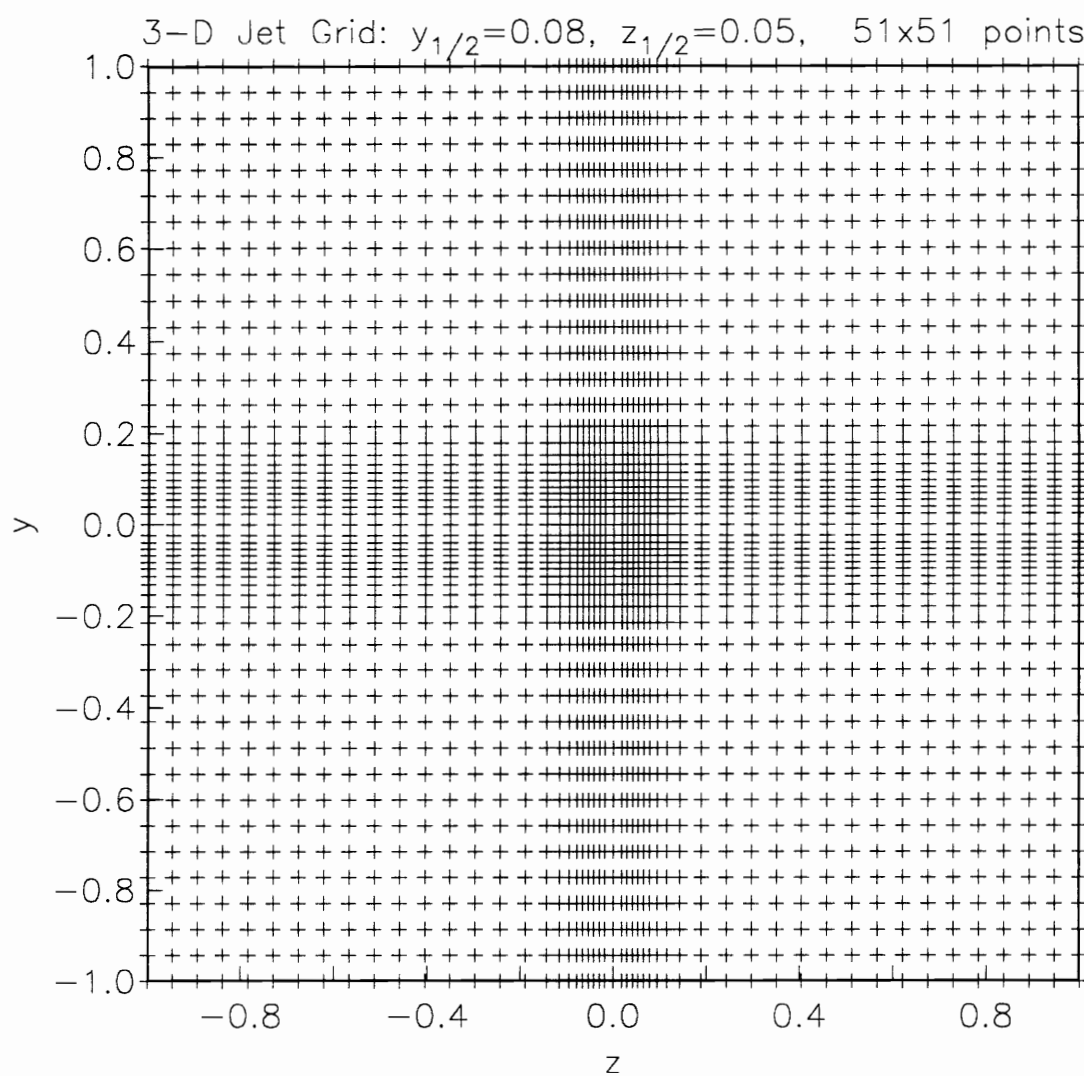


Figure 6.13 Typical computational grid for a 3-D elliptic jet; $y_{1/2}=0.08$,
 $z_{1/2}=0.05$, 51 x 51 points

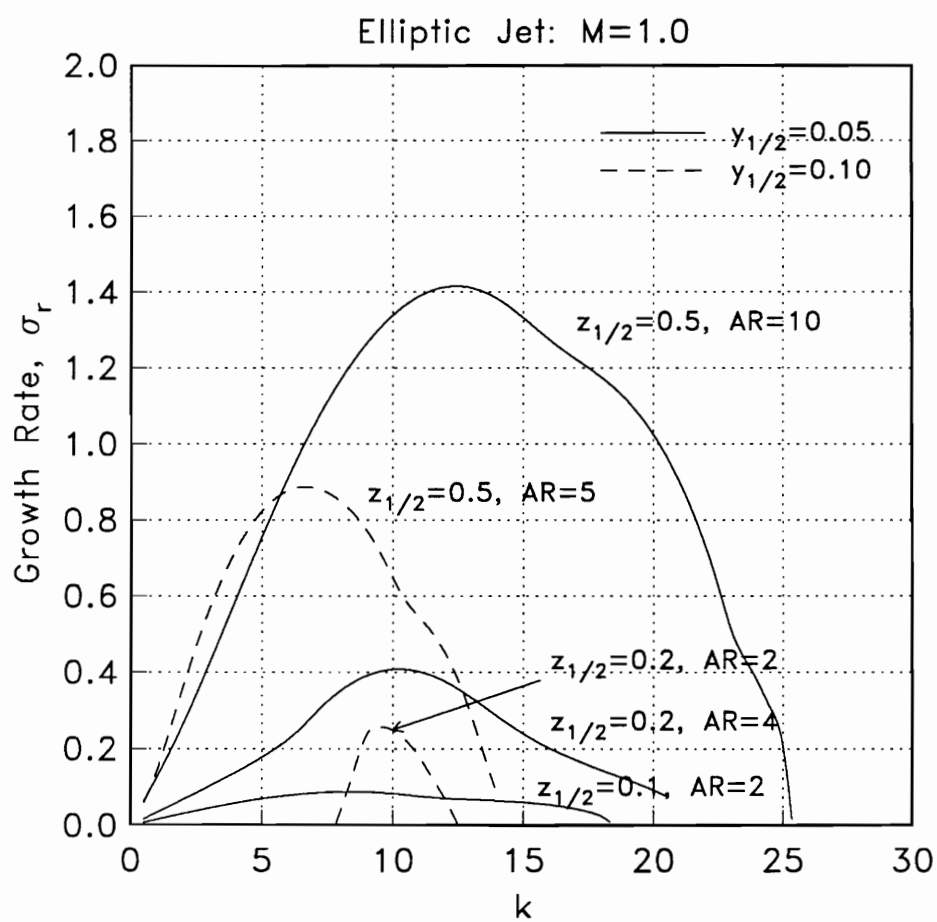


Figure 6.14 Elliptic jet growth rates for various jet aspect ratios

Vita

The author was born in Dayton, Ohio on April 6, 1964. He grew up and attended high school in Fairfax, Virginia before enrolling at Virginia Polytechnic Institute and State University (Virginia Tech) in 1982. While an undergraduate, he participated in the CO-OP program by working at the U.S. Naval Research Laboratory in Washington, D.C. He completed his B.S. in Aerospace and Ocean Engineering in 1987. He earned his M.S. at Virginia Tech in Aerospace Engineering in 1989 for his experimental work in high speed mixing studies. His research for this dissertation centered on an analytical study of the stability of high speed mixing flows. He currently resides in Floyd, Virginia with his wife, Lorette, and their cat, four dogs and two horses.